OCEANIC VERTICAL MIXING: A REVIEW AND A MODEL WITH A NONLOCAL BOUNDARY LAYER PARAMETERIZATION

W. G. Large
J. C. McWilliams
S. C. Doney
National Center for Atmospheric Research
Boulder, Colorado

Abstract. If model parameterizations of unresolved physics, such as the variety of upper ocean mixing processes, are to hold over the large range of time and space scales of importance to climate, they must be strongly physically based. Observations, theories, and models of oceanic vertical mixing are surveyed. Two distinct regimes are identified: ocean mixing in the boundary layer near the surface under a variety of surface forcing conditions (stabilizing, destabilizing, and wind driven), and mixing in the ocean interior due to internal waves, shear instability, and double diffusion (arising from the different molecular diffusion rates of heat and salt). Mixing schemes commonly applied to the upper ocean are shown not to contain some potentially important boundary layer physics. Therefore a new parameterization of oceanic boundary layer mixing is developed to accommodate some of this physics. It includes a scheme for determining the boundary layer depth h, where the turbulent contribution to the vertical shear of a bulk Richardson number is parameterized. Expressions for diffusivity and nonlocal transport throughout the boundary layer are given. The diffusivity is formulated to agree with similarity theory of turbulence in the surface layer and is subject to the conditions that both it and its vertical gradient match the interior values at h. This nonlocal "K profile parameterization" (KPP) is then verified and compared to alternatives, including its atmospheric counterparts. Its most important feature is shown to be the capability of the boundary layer to penetrate well into a stable thermocline in both convective and wind-driven situations. The diffusivities of the aforementioned three interior mixing processes are modeled as constants, functions of a gradient Richardson number (a measure of the relative importance of stratification to destabilizing shear), and functions of the double-diffusion density ratio, R_ρ. Oceanic simulations of convective penetration, wind deepening, and diurnal cycling are used to determine appropriate values for various model parameters as weak functions of vertical resolution. Annual cycle simulations at ocean weather station Papa for 1961 and 1969–1974 are used to test the complete suite of parameterizations. Model and observed temperatures at all depths are shown to agree very well into September, after which systematic advective cooling in the ocean produces expected differences. It is argued that this cooling and a steady salt advection into the model are needed to balance the net annual surface heating and freshwater input. With these advections, good multiyear simulations of temperature and salinity can be achieved. These results and KPP simulations of the diurnal cycle at the Long-Term Upper Ocean Study (LOTUS) site are compared with the results of other models. It is demonstrated that the KPP model exchanges properties between the mixed layer and thermocline in a manner consistent with observations, and at least as well or better than alternatives.

1. INTRODUCTION

A major challenge in the creation of Earth system models is the development of improved submodels of all its components, including the ocean. Recent experiences with coupled atmosphere-ocean models demonstrate that extensive and pervasive difficulties arise because of a mismatch in the equilibrium surface heat flux of each model individually. To avoid the resulting climate drift, flux corrections are often applied [*Sausen et al.*, 1988]. A demanding, but physically more attractive alternative is model improvement. A critical requirement for an ocean submodel is that it simulate the annual cycle of sea surface temperature (SST) globally, since SST is the most important ocean property governing the exchange of energy between the ocean and atmosphere. The SST represents a balance among many processes, including air-sea exchange, oceanic transport, and vertical mixing. The latter must be parameterized because the processes involve small

Reviews of Geophysics, 32, 4 / *November 1994*
pages 363–403
8755-1209/94/94RG-01872$15.00
Paper number 94RG01872

turbulent scales that presently cannot be resolved in other than very limited domains. This present work seeks practical parameterizations with skill at distributing properties in the vertical in all oceanic regimes: polar, midlatitude, and equatorial. To do so even over climate scales, it may be necessary to mix properly over the much shorter timescales of the diurnal cycle and storm events because of strong nonlinearities.

The atmosphere and ocean communicate with each other via their respective planetary boundary layers (PBL), so both may need to be well modeled. A rich literature exists for boundary layers in general [*Monin and Yaglom*, 1971] and the atmospheric boundary layer (ABL) in particular [*Haugen*, 1973; *Nieuwstadt and van Dop*, 1982; *Stull*, 1988]. Boundary layers have distinctive physics from fluid interiors [*Wyngaard*, 1982] and hence are governed by their own mixing rules. Thus ocean vertical mixing requires two distinct parameterizations: one for the ocean interior and one for the oceanic surface boundary layer (OBL). In general, employing a single scheme for both is not justified. Several known aspects of boundary layer physics are outlined in the first part of section 2. The challenge is to incorporate this knowledge into a global ocean model without imposing unreasonable computational demands.

The ABL has been much more fully observed and understood than either the oceanic surface boundary layer or bottom (benthic) boundary layer (BBL). By assuming similarity between PBLs, the wealth of atmospheric experience can be applied to models of the OBL and BBL. The extent of the knowledge gap is illustrated by the fact that heat and momentum fluxes have yet to be directly measure in the open OBL. The technical difficulty of separating the turbulent vertical velocity from surface wave motions is not so problematic under sea ice, where *McPhee and Martinson* [1994] have directly measured profiles of these fluxes. In contrast, time series and profiles of vertical turbulent fluxes (and other turbulence parameters) have been measured in the ABL from meteorological towers [*Kaimal et al.*, 1976] and aircraft [*Lenschow et al.*, 1980] over a relatively wide range of forcing conditions. Equally important, according to *Wyngaard* [1982], are the numerical investigations of the ABL pioneered by *Deardorff* [1972a]. These large eddy simulations (LES) resolve most of the energy containing turbulent eddies such that the parameterized subgrid-scale turbulence is relatively unimportant. Although these models are restricted to limited domains and short integration times, they do provide valuable data with which to formulate and evaluate parameterizations for boundary layer models used on all time and space scales.

The first objective of this paper is to choose, from a wide assortment of classes, a vertical mixing scheme that can be developed into a suitable OBL model for climate studies. The choices are surveyed in the second part of section 2, and a nonlocal K profile parameterization (KPP) of the boundary layer [*Troen and Mahrt*, 1986] is selected. Additional components of the complete KPP model are local parameterizations for each of three mixing processes in the ocean interior (section 4), rules for matching the boundary layer to the interior, and surface and bottom boundary conditions. The boundary layer scheme and matching are described in section 3. The boundary conditions are discussed in Appendix A, and some of the details of the model formulation are presented in Appendix B. The details of the vertical discretization and numerics used to implement the numerical model are given in Appendix D.

Alternatives considered in section 2 include first-order mixing length closure [*Blackadar*, 1962], the hierarchy of second-order moment closures espoused by *Mellor and Yamada* [1982] with embellishments [*Gaspar et al.*, 1990; *Kantha and Clayson*, 1994], and bulk mixed-layer models [e.g., *Kraus and Turner*, 1967; *Niiler*, 1975; *Price et al.*, 1986]. Not included a priori are closures without an established history of geophysical applications or those judged too computationally demanding or too complicated without well-demonstrated compensating benefits. Examples of such models are third-order moment closures and the transilient model of *Stull* [1984].

In section 5, model solutions for several classic oceanic situations (convective deepening, wind deepening and diurnal cycling) are used to determine, validate, and refine choices for the important model parameters. With these choices fixed, simulations of a complete oceanic annual cycle are then used to demonstrate model performance. The results of further sensitivity experiments are given in Appendix C. Model simulations, again with fixed parameter values, are compared with observations and previously published model results in section 6. The discussion, section 7, recaps the KPP model and its successes, reviews the model intercomparison, and suggests further KPP model developments. Overall, the KPP model is found to perform at least as well as others in all comparisons and significantly better in some. Unfortunately, the oceanic database is not fully up to the task of settling all modeling questions.

2. PLANETARY BOUNDARY LAYERS

This section first reviews the distinctive physics of planetary boundary layers then discusses various PBL models. These layers are fundamentally turbulent and extend from near the surface to the boundary layer depth h, which is the limit to which boundary layer eddies can penetrate in the vertical. PBL models strive to represent faithfully the mixing due to the turbulent vertical velocities w of unresolved eddies. This turbulence is driven primarily by the surface stress, τ_0 and

a negative surface buoyancy flux B_f and is suppressed by dissipation and a stabilizing $B_f > 0$. Like the wind stress, all forcing functions are defined to be positive when they act to increase the oceanic values of the property being transferred. Thus positive forcing moves properties downward into the ocean.

The time evolution of a property X due to PBL eddies is expressed as the vertical divergence of the kinematic turbulent fluxes:

$$\partial_t X = -\partial_z \overline{wx} \tag{1}$$

where t and z are the time and upward vertical coordinates, respectively, with ∂ denoting a partial derivative with respect to its subscript and the overbar denoting a time average. In (1) and hereinafter whenever generalization is possible, uppercase X represents mean quantities such as eastward velocity U, northward velocity V, potential temperature T, buoyancy B, and ocean salinity S, and lowercase x represents their turbulent fluctuations u, v, θ, b and s, respectively. Similarly, a subscript x is used to associate a particular quantity, such as diffusivity, with any of the above properties. Whenever it is necessary to distinguish the velocity or momentum components from the scalar properties, the subscripts m and s, respectively, are used. In these situations, S and s are used to represent the mean and turbulent components of all the scalar properties. Sometimes potential temperature needs to be treated uniquely, and the subscript θ is used, while S, s, and subscript s then apply only to salinity and to the concentration of other solutes that behave like salinity, such as water vapor in the atmosphere and nutrients in the ocean.

Boundary Layer Physics

The semiempirical Monin-Obukhov similarity theory is the most well tested boundary layer scaling. It argues that in the surface layer near the boundary, the only important turbulence parameters are the distance from the boundary, d, and the surface kinematic fluxes $\overline{wx}_0$. In the ABL and BBL, $d = z$, while in the OBL, $d = -z$. The fundamental turbulent parameters that can be formed from these quantities are the friction velocity u^*; the scale of the turbulent fluctuations of any scalar property, S^*; and the Monin-Obukhov length scale L:

$$\begin{aligned} u^{*2} &= (\overline{wu}_0^2 + \overline{wv}_0^2)^{1/2} = |\tau_0|/\rho_0 \\ S^* &= -\overline{ws}_0/u^* \\ L &= u^{*3}/(\kappa B_f) \end{aligned} \tag{2}$$

where $\kappa = 0.4$ is von Kármán's constant and ρ_0 is surface density.

The surface layer, $d < \varepsilon h$ ($\varepsilon \ll 1$), need not be a constant flux layer [*Tennekes*, 1973a]. In many situations a horizontal pressure gradient is balanced by substantial vertical stress divergence. However, as long as the surface fluxes remain the important parameters, dimensional analysis defines the dimensionless profiles as universal functions of the stability parameter $\zeta = d/L$:

$$\begin{aligned} \phi_m(\zeta) &= \frac{\kappa d}{u^*}\,\partial_z (U^2 + V^2)^{1/2} \\ \phi_s(\zeta) &= \frac{\kappa d}{S^*}\,\partial_z S \end{aligned} \tag{3}$$

These functions have been determined empirically from measurements in the ABL, but there is no consensus about their precise functional form [*Högström*, 1988]. The forms used throughout this paper are given in Appendix B and plotted in Figure B1.

Integration of (3) gives the mean property profiles,

$$(U(d)^2 + V(d)^2)^{1/2} = (U_0^2 + V_0^2)^{1/2} + \frac{u^*}{\kappa}\left[\ln\left(\frac{d}{z_m}\right) - \psi_m(\zeta)\right] \tag{4a}$$

$$S(d) = S_0 + \frac{S^*}{\kappa}\left[\ln\left(\frac{d}{z_s}\right) - \psi_s(\zeta)\right] \tag{4b}$$

$$\psi_x(\zeta) = \int_{z_x/L}^{\zeta} \frac{[1 - \phi_x(\zeta')]}{\zeta'}\, d\zeta'$$

where the square root terms are speeds; the X_0 are surface values; and the constants of integration, z_x, are the roughness lengths. The ψ_x functions have been integrated for some common analytic forms of the ϕ_x functions by *Paulson* [1970]. The neutral ($\psi_x = 0$) forms of (4) are the familiar logarithmic profiles. Alternative derivations of these profiles also do not require a constant stress layer [*Tennekes*, 1973a]. The surface layer does not extend all the way to the surface [*Monin and Yaglom*, 1971; *Liu et al.*, 1979] because at a finite distance, surface roughness elements and molecular processes begin to directly influence the turbulence. Therefore neither (3), nor (4) can be expected to hold as d approaches z_x.

A typical value of ε is 0.1 [*Tennekes*, 1973a]. Fluxes should be within about 20% of their surface values at $d = \varepsilon h$ and approach their surface values linearly as d becomes small [*Lumley and Panofsky*, 1964; *Tennekes*, 1973a]. In ABLs of the order of 1 km in height, logarithmic profiles have been observed to extend to a height of 100 m [*Carl et al.*, 1973], implying that the surface fluxes are still the most important turbulence parameters throughout the surface layer even though local fluxes can be measurably different from their surface values.

In addition to a surface layer, another important feature of boundary layers is that the turbulence is fundamentally nonlocal; that is, in addition to local

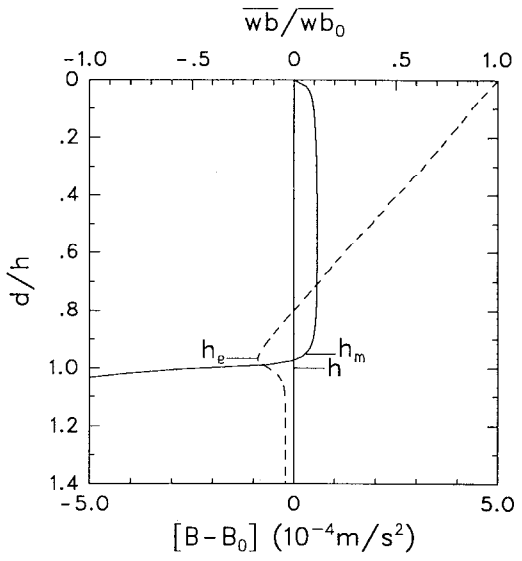

Figure 1. Relative buoyancy (solid trace, bottom scale) and buoyancy flux (dashed trace, top scale) profiles after 3.0 days of convective deepening into an initially uniformly stratified water column of $\partial_z T = 0.1°C\ m^{-1}$, $N = 0.016\ s^{-1}$, under the action of a steady cooling, $Q_t = -100\ W\ m^{-2}$. Axes have been normalized with a boundary layer depth, $h = 13.6$ m and a surface buoyancy flux, $\overline{wb}_0 = 6.3 \times 10^{-8}\ m^2\ s^{-3}$. Also shown are the entrainment depth, h_e, and the mixed layer depth, h_m.

properties and gradients, local fluxes depend on boundary layer parameters such as the surface fluxes and h. Important characteristics of nonlocal behavior are the coherent structures that can be detected in PBLs [*Mahrt and Gibson*, 1992]. Coherent structures identified in the turbulent ABL include buoyant vertical plumes, convergence lines, sweeps, microbursts, horizontal roll vortices, mesoscale cellular convective elements, Kelvin-Helmholtz waves, and internal gravity waves. Most of these structures are described by *Stull* [1988]. After surface and internal gravity waves, the most important coherent structures in the OBL are thought to be Langmuir cells [*Weller and Price*, 1988]. These are near-surface, counterrotating vortices with horizontal axes that are nearly aligned with the mean wind. Their dynamics are not well understood, but in the model of *Craik and Leibovich* [1976] they are generated by the interaction between the surface gravity wave induced current (Stokes drift) and the wind-driven current. It is uncertain what role Langmuir circulation plays in the ocean, but *Weller et al.* [1984] suggest that it could be an important factor in transporting properties that are not uniformly distributed within the mixed layer.

Figure 1 illustrates expected profiles of buoyancy and buoyancy flux in a convective oceanic boundary layer. One manifestation of nonlocal behavior found in such boundary layers is what is traditionally termed countergradient heat flux. This flux is characterized by upward buoyancy flux $\overline{wb} > 0$ in locally stable or neutral regions where the mean buoyancy increases or remains constant with height. In general, such fluxes can be present with any gradient, so nonlocal transport [*Holtslag and Boville*, 1993] is a more general term that also applies to passive scalar transports. This feature of convection is generally observed throughout the central 50% or more of both atmospheric and laboratory boundary layers [*Deardorff*, 1966] and of LES experiments [*Deardorff*, 1972b; *Holtslag and Moeng*, 1991]. In Figure 1 it dominates the region $0.35 < d/h < 0.80$. Different theoretical considerations lead to the same result, namely, that the heat flux should have a nonlocal convective transport in addition to the familiar local downgradient component. Theoretical expressions for the countergradient heat flux have been derived from the turbulent evolution equation for $\partial_t \overline{w\theta}$. *Deardorff* [1972b] finds that it arises from the buoyant production term, while *Holtslag and Moeng* [1991] find the turbulent transport term responsible. *Holtslag and Moeng* [1991] use LES data to evaluate both these possibilities and find that both give similar nonlocal behavior throughout the central region of the boundary layer despite the differing physics.

Wyngaard and Brost [1984] suggest that another fundamental property of convective boundary layers is that the vertical diffusivity profile for passive scalars is radically different depending on whether the property fluxes are driven by entrainment or surface fluxes. Because they were considering the ABL, entrainment-driven diffusion was termed "top-down" and the more familiar surface-driven diffusion was termed "bottom-up." Furthermore, they attribute this peculiar behavior to vertical asymmetry. An observed characteristic of this asymmetry is that buoyant plumes are horizontally narrower and have larger vertical velocities than the more diffuse return flows. *Wyngaard and Brost* [1984] present LES results that confirm that entrainment-driven diffusivities are significantly smaller than surface-driven diffusivities. An important implication is that a single diffusivity defined for the total process may be ill behaved but that the two processes can be parameterized separately and later superimposed. However, *Holtslag and Moeng* [1991] use the LES data of *Moeng and Wyngaard* [1989] and obtain well-behaved expressions by incorporating a nonlocal transport term in the flux parameterizations. Entrainment-driven diffusion may be very important in the ocean, where it is the principal source of salt and nutrients to the OBL.

In the case of a purely convective boundary layer, $u^* = 0$ and $B_f < 0$, eroding into a region of stable stratification (Figure 1), the entrainment depth h_e, where the negative buoyancy flux is maximum, is less than the boundary layer depth h. The mixed layer depth h_m can depend a great deal on definition [*Lukas and Lindstrom*, 1991]. Here it is arbitrarily taken as

the shallowest depth where $\partial_z B$ exceeds 5.2×10^{-5} s^{-2}, and it is less than h_e. As was argued by *Ball* [1960], the entrainment flux at h_e is driven by the surface buoyancy flux, so that in pure convection the ratio of these two fluxes should be approximately a constant, β_T. The observational data [*Deardorff et al.*, 1969; *Tennekes*, 1973b] and LES results [*Moeng and Wyngaard*, 1984, 1989] suggest $\beta_T = -0.2$. This relationship will be used in the next section to parameterize the role of unresolved turbulent shear in determining h.

Boundary layers are often characterized by very small vertical property gradients over large portions of their central region (e.g., Figure 1). This observation has led to the concept of the boundary layer as a well-mixed layer, especially in the ocean, where the isothermal layer often extends to very near the surface. A major theoretical objection to the well-mixed boundary layer is the implicit infinite diffusivity leading to all properties being instantaneously mixed throughout the layer. As is shown by Figure 1 and other cases, a more physical finite diffusion is capable of evolving well-mixed regions over much of the boundary layer.

Many observations also contradict the mixed-layer concept. Properties are often observed to have vertical structure throughout much of the boundary layer. A notable example is the specific humidity profiles shown by *Mahrt* [1976], which *Wyngaard and Brost* [1984] attribute to the entrainment flux of water vapor that diffuses according to finite "top-down" diffusivity laws. A well-mixed surface layer is not always found in the ocean either. Also, isothermal, isohaline, and turbulent layers are not universally found to coincide. In the western equatorial Pacific, for example, *Lukas and Lindstrom* [1991] find that the mean mixed-layer depths based on temperature and salinity gradient criteria are 37 m and 29 m, respectively. Individual profiles show that the isohaline layer can be as much as 90 m deeper or 70 m shallower than the isothermal layer. It has also been recognized that mixed layers might extend to the depth of previous turbulent boundary layers and that at any given time the boundary layer may be thinner. The opposite situation can also exist in the ocean. Recent observations of diurnal cycles of turbulence at the equator [*Peters et al.*, 1988; *Moum et al.*, 1989] clearly show nighttime turbulence down to 80 m, far below the 20-m depth of the isothermal layer. This state can be interpreted as the penetration of the convective boundary layer, though *Moum et al.* [1989] suggest interval waves as the cause. In midlatitudes, strongly shear-driven boundary layers do appear to penetrate tens of meters into the seasonal thermocline, giving rise to abnormal mixed-layer cooling [*Large et al.*, 1986; *Large and Crawford*, 1994].

Unfortunately, relatively little is known about the OBL from either direct observations or resolved turbulence numerical experiments. Only recently has LES modeling been applied to the OBL [*McWilliams et al.*, 1993]. It is this state of affairs that provides the motivation for incorporating the knowledge and experience of atmospheric and laboratory boundary layers to the ocean. Although there are physical reasons to expect differences between the ABL and OBL, until uniquely oceanic physics is observed and quantified, the assumption that the ABL and OBL are physically similar will remain appropriate. One obvious difference is surface waves. These ought to have little effect on the ABL above the order of a wave height above the surface, i.e., about 1% of the boundary layer. However, a wave height is a much larger fraction of the OBL depth. Wind-driven surface waves are believed to be essential to the generation of Langmuir circulation [*Craik and Leibovich*, 1976]. Also, surface wave orbital velocities and shear can extend throughout the OBL and perhaps interact with surface-driven turbulence in important ways. There could be a divergent horizontal transport of energy by surface and internal gravity waves. Another difference is that the surface velocity of the ABL is zero over land and usually negligible over the ocean. In the ocean the velocity is usually largest near the surface. A further complication is that the OBL strongly absorbs solar radiation, while the ABL is nearly transparent. How to include absorbed radiation properly in the expressions for L and S^* in (2), in the flux profiles (equation (3)), and hence in the logarithmic profiles (equation (4)) are unanswered research questions (Appendix C).

Boundary Layer Models

In trying to incorporate boundary physics in climate models, first-moment models are attractive because there are time evolution (prognostic) equations for only mean, or first moment, quantities X. The system is closed by parameterizing higher-order moments, such as the second-moment kinematic fluxes (equation (1)), in terms of the first-moment prognostic variables. The order of a turbulence closure is defined to be equal to the highest prognostic moment, so these models have first-order closure schemes. They are also easily adapted to finite differencing and matched to models of the interior. Common to these schemes is the assumption that turbulent, like molecular, diffusion is downgradient, depending linearly on the local property gradient, with an appropriate eddy diffusivity K_x, the constant of proportionality:

$$\overline{wx} = -K_x \partial_z X \tag{5}$$

Specification of K_x throughout the boundary layer, K theory, includes the constant K_x of *Ekman* [1905]. *Stull* [1988] gives a lengthy list of other proposed K_x parameterizations.

What might be termed a nonlocal K profile model was developed by *Troen and Mahrt* [1986] specifically for use in large-scale models of the atmosphere. There

are two distinctly nonlocal aspects of their model. First, there is an additional nonlocal transport term on the right-hand side of (5). Second, the diffusivity everywhere in the boundary layer depends upon both the surface forcing and the depth of the boundary layer. They report that the model is well behaved in transitions from stable to unstable forcing. It requires some resolution in the boundary layer, but detailed resolution is needed in neither the transition layer near h, nor the surface layer. Furthermore, in the convective limit of u^* approaching zero the model boundary layer turbulence is well behaved because it becomes dependent on the convective velocity scale,

$$w^* = (-B_f h)^{1/3} \tag{6}$$

and the diffusivities are well defined. *Holtslag and Boville* [1993] compare a similar nonlocal K profile parameterization to a local K approach [*Louis*, 1979] in an atmospheric general circulation model. They choose the nonlocal scheme for a global climate model primarily because of its better physics in dry convective conditions. Nighttime and wintertime convection are very prominent features of oceanic boundary layers. Therefore such a scheme appears to be very well suited for the boundary layer parameterization in an ocean general circulation model too. Other possibilities are surveyed below, but in no case do the advantages outweigh the apparent disadvantages relative to the nonlocal K profile approach.

The model of upper ocean mixing in the marginal ice zone of *McPhee* [1987] has neither of the above nonlocal aspects found in the *Troen and Mahrt* [1986] model. There is only downgradient diffusion like (5), and K_x is proportional to a locally defined, height dependent friction velocity and a length scale that describes the vertical scale of energy-containing eddies at any level. The length scale in turn depends only on local fluxes and the Coriolis parameter. As was noted by *Tennekes* [1973a], u^*, not the local friction velocity, is the true boundary layer velocity parameter that is independent of d. Consistent with this viewpoint is the observation [*Panofsky*, 1973] that the logarithmic behavior (4) describes the wind profile to greater heights when u^*, rather than local friction velocity, is used. The *McPhee* [1987] scheme behaves very differently in the convective limit. Instead of depending on w^*, the diffusivity become proportional to the square of the local friction velocity and independent of the buoyancy flux.

Nonlinear mixing length, or L theory, follows from *Prandtl*'s [1925] proposition that the significant eddy size, or mixing length L_m, is proportional to the standard deviation of the vertical displacement of fluid particles. *Heisenburg*'s [1948] hypothesis further states that K_x is proportional to the four-thirds power of L_m and the one-third power of the molecular dissipation. *Blackadar* [1962] expresses this latter dependency in terms of the vertical shear to arrive at

$$K_x = L_m^2[(\partial_z U)^2 + (\partial_z V)^2]^{1/2} \tag{7}$$

$$L_m = \kappa d/(1 + \kappa d/L_0)$$

where L_0 is an empirical, asymptotic value of L_m from observations of the free atmosphere. This formulation yields good results only near the surface, where L_m approaches κd in accord with the similarity result (3). The form (7) has no nonlocal transport term, and K_x varies only with local shear and d.

There are many other proposed parameterizations of L_m. In numerical models where the grid spacing Δ is less than the significant eddy size, L theory is used to parameterize the subgrid-scale mixing process. For this purpose it is common to make L_m proportional to Δ, with an adjustable constant of proportionality. This practice follows *Smagorinsky* [1963], who applied it to lateral mixing in a two-layer atmospheric general circulation model. It is also used for subgrid-scale vertical mixing in LES, where significant eddies are resolved in all three dimensions [*Lilly*, 1967; *Deardorff*, 1970].

The class of second-order closure models directly computes the time evolution of second-moment quantities, including the turbulent fluxes $\overline{wx}(d)$. Full closure of the second-moment equations therefore carries the substantial computing burden of integrating many prognostic equations. *Donaldson* [1973] considers a system with three velocity components, potential temperature, and one conservative scalar and formally derives time evolution equations for each of the 15 prognostic second moments. *Mellor and Yamada* [1974, 1982] present a hierarchy of second-moment closures for a u, v, w, and θ system. At each degree of approximation the "level" of their closure decreases (from 4 to 1). There are 10 prognostic equations for the second moments in their full, level 4 closure. To date it has not been demonstrated that the results from such models justify the additional complexity and computations.

At level 3 in their hierarchy, *Mellor and Yamada* [1982] solve prognostic equations for only two second moments; temperature variance $\overline{\theta^2}$ and turbulent kinetic energy $\bar{e}$ $(= 0.5\overline{(u^2 + v^2 + w^2)})$. This simplification arises from expressing the other second-order moments as diagnostic equations depending only on themselves; mean quantities, including $\bar{e}$; and empirical length scales. Similarly, expressing $\overline{\theta^2}$ as a diagnostic equation results in the intermediate level 2.5 degree of approximation, with $\bar{e}$ the only prognostic second moment. Since all the length scales are related to the scale of energy containing turbulence, they are usually made proportional to a master length scale, such as L_m of (7) with an analytic expression for L_0.

The level 2 approximation assumes that shear plus buoyant production of turbulent energy is balanced locally by turbulent dissipation. Dissipation is then parameterized by $\bar{e}^3/L_e$ to give a diagnostic equation

for $\bar{e}$ as well. The need to specify yet another length scale L_e compounds the length scale problem alluded to above. At this point in the hierarchy there are no second moment prognostic equations, so the closure is akin to L theory. *Mellor and Yamada* [1982] report that further simplification, level 1, failed to reproduce observational data.

The most popular member of the *Mellor and Yamada* [1982] hierarchy is the level 2.5. However, as was discussed extensively by *Kantha and Clayson* [1994], these schemes are known to have the general trait of too little entrainment during convection and the related problem of too little mixing across stabilizing density gradients. There are several possible causes of this problem. *Zeman and Lumley* [1976], for example, find that realistic entrainment requires buoyancy effects to be accounted for in the closure of the turbulent transport of third-order fluxes. According to *Mellor and Yamada* [1982], the use of a master length scale, which sets all processes proportional to a single scale, is another major weakness. *Moeng and Wyngaard* [1989] present an overview of second-order closures of the $\partial_t \bar{e}$ equation needed by level 3 and level 2.5 schemes. They note two more objections to these closures as usually practiced, namely, their downgradient transport assumption, which is inadequate in the convective ABL because it neglects nonlocal effects, and their neglect of buoyancy effects on the pressure-scalar covariance closure. They also find that the *Mellor and Yamada* [1982] parameterization of the eddy diffusivity for $\bar{e}$ is more than an order of magnitude less than that computed from LES data.

In response to these criticisms, there have been several recent developments. *Mellor* [1989] adds a prognostic equation for the product of $\bar{e}$ times the master length scale. *Gaspar et al.* [1990] ameliorate the master length scale problem by specifying two independent diagnostic length scales but continue to assume downgradient transport. *Kantha and Clayson* [1994] attempt to address some of *Moeng and Wyngaard*'s [1989] concerns and enhance the mixing in the shear region below the oceanic mixed layer. Results from these latter two ocean applications are presented in section 6.

Mixed-layer models attempt to capitalize on the very small vertical gradients found in the PBLs. They have often been applied to the ocean because many ocean observations support the idea of a well-mixed layer down to a mixed-layer depth h_m. Neglecting horizontal transports and integrating (1) through this layer leads to [*Stevenson and Niiler*, 1983]

$$h_m \partial_t X_m + \Delta X[\partial_t h_m + W(h_m)] = \overline{wx}(h_m) - \overline{wx}_0 \quad (8)$$

where X_m is the mean property value in the layer and $\Delta X = X_m - X(h_m)$. Given the right-hand side of (8) and $W(h_m)$ as boundary conditions, integration can proceed once the evolution of h_m is specified. A prognostic equation for h_m is commonly derived from the turbulent kinetic energy budget of the mixed layer [*Kraus and Turner*, 1967], where the energy inputs from both the mean shear and the wind are parameterized as being proportional to u^{*3}. However, G. C. Crawford and W. G. Large (A numerical investigation of ocean inertial resonant response to wind events, submitted to *Journal of Physical Oceanography*, 1994) (hereinafter referred to as Crawford and Large, submitted manuscript, 1994) find that the mean shear production can depend a great deal on the rotation rate of the wind stress vector. Implicit in many of these models are property jumps at the base of the mixed layer, but these are not generally observed even following large storm events [*Large et al.*, 1986]. However, an advantage of such integral models is that observed rapid changes in mixed-layer vertical gradients do not need to be explicitly resolved. Models based on these ideas include those of *Niiler* [1975] and its derivatives [*Davis et al.*, 1981b] and of *Garwood* [1977]. The model of *Price et al.* [1986], on the other hand, calculates h_m from bulk stability considerations and smooths out property jumps with local Richardson number dependent mixing below the mixed layer. A bulk stability criterion is also used to deepen the mixed-layer model of *Pollard et al.* [1973].

Bulk ocean mixed-layer models are common, but by vertically integrating they lose distinctive mixed-layer features, such as the logarithmic profiles (4) and nonlocal transport. In convection they typically satisfy static stability, but are not necessarily formulated to produce the additional entrainment due to convective elements penetrating into the stratified region beyond the mixed layer. Similarly, wind-driven penetrative entrainment may not be accounted for.

3. A NONLOCAL *K* PROFILE MODEL OF OCEANIC BOUNDARY LAYER MIXING

In this section the nonlocal K profile parameterization of *Troen and Mahrt* [1986] is adapted for use as an oceanic boundary layer model. The OBL scheme retains the two nonlocal characteristics discussed in section 2. Other important characteristics of both applications are that they are consistent with similarity theory (3) in the surface layer, the boundary layer is capable of penetrating the interior stratification, and turbulent transport vanishes at the surface. In this section the OBL model is shown to have some additional desirable features. For example, turbulent shear contributes to the diagnosed boundary layer depth so as to make the entrainment of buoyancy at the base of the convective OBL independent of the interior stratification. In addition, interior mixing at the base of the boundary layer ($d = h$) influences the turbulence throughout the boundary layer. Also, in the convective limit the turbulent velocity scales for both momentum and scalars become directly proportional to w^*.

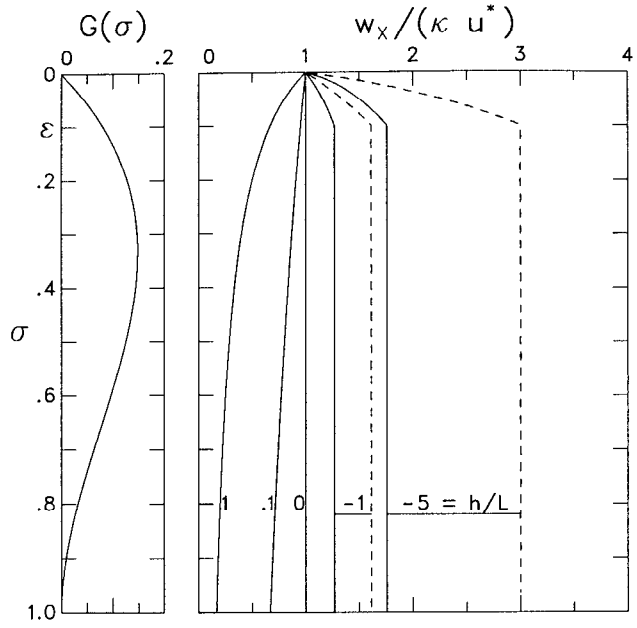

Figure 2. (left) Vertical profile of the shape function $G(\sigma)$, where $\sigma = d/h$, in the special case of $G(1) = \partial_\sigma G(1) = 0$. (right) Vertical profiles of the normalized turbulent velocity scale, $w_x(\sigma)/(\kappa u^*)$, for the cases of $h/L = 1, 0.1, 0, -1$, and -5. In unstable conditions, $w_s(\sigma)$ (dashed traces) is greater than $w_m(\sigma)$ (solid traces) at all depths, but for stable forcing $h/L \geq 0$, the two velocity scales are equal at all depths.

The problem of determining the vertical turbulent fluxes of momentum and both active and passive scalars in (1) throughout the OBL is closed by adding a nonlocal transport term γ_x to (5):

$$\overline{wx}(d) = -K_x(\partial_z X - \gamma_x) \tag{9}$$

In practice, the external forcing is first prescribed, then the boundary layer depth h is determined, and finally profiles of the diffusivity and nonlocal transport are computed. Here the depth determination is described last because its formulation depends on the form of the diffusivity. The external forcing is discussed in Appendix A.

Diffusivity and Nonlocal Transport

The profile of boundary layer diffusivity is expressed as the product of a depth dependent turbulent velocity scale w_x and a nondimensional vertical shape function $G(\sigma)$:

$$K_x(\sigma) = hw_x(\sigma)G(\sigma) \tag{10}$$

where $\sigma = d/h$ is a dimensionless vertical coordinate that varies from 0 to 1 in the boundary layer. At all depths, values of K_x are directly proportional to h, reflecting the ability of deeper boundary layers to contain larger, more efficient turbulent eddies. Particular examples of $G(\sigma)$ and $w_x(\sigma)$ profiles are shown in Figure 2. The shape function is assumed to be a cubic polynomial [*O'Brien*, 1970],

$$G(\sigma) = a_0 + a_1\sigma + a_2\sigma^2 + a_3\sigma^3 \tag{11}$$

so that there are four coefficients with which to control the diffusivities and their vertical derivatives at both the top and bottom of the boundary layer.

Turbulent eddies do not cross the surface, so there is no turbulent transport across $d = 0$. The implied condition $K_x(0) = 0$ is imposed by setting $a_0 = 0$. Molecular transport terms, in addition to (9), are required only if the very near surface, where molecular processes dominate [*Liu et al.*, 1979], is to be resolved.

In the surface layer $\sigma < \varepsilon$, where Monin-Obukhov similarity theory applies, eliminating the property gradient from (3) and (9) with $\gamma_x = 0$ and then substituting (10) for K_x with $G(\sigma) \simeq \sigma(a_1 + a_2\sigma)$ leads to

$$w_x(\sigma)(a_1 + a_2\sigma) = \left[\frac{\kappa u^*}{\phi_x(\zeta)}\right]\left(\frac{\overline{wx}(d)}{\overline{wx}_0}\right) \tag{12}$$

A sensible way of satisfying (12) is to equate the term in square brackets to the turbulent velocity scales. As was argued by *Troen and Mahrt* [1986], this formulation is assumed to be valid everywhere in the stably forced boundary layer. In unstable conditions the turbulent velocity scales beyond the surface layer are assumed to remain constant at their $\sigma = \varepsilon$ values. Without this constraint, unstable w_x values would become very large (Figure 2), in the absence of any supporting observational evidence. Therefore the general expression for the velocity scales is

$$\begin{aligned} w_x(\sigma) &= \frac{\kappa u^*}{\phi_x(\varepsilon h/L)} \qquad \varepsilon < \sigma < 1 \qquad \zeta < 0 \\ w_x(\sigma) &= \frac{\kappa u^*}{\phi_x(\sigma h/L)} \qquad \text{otherwise} \end{aligned} \tag{13}$$

These scales are functions of $\zeta = d/L = \sigma h/L$, so profiles of $w_x(\sigma)$ are fixed functions of h/L, as is shown in Figure 2.

The ϕ_x functions (Appendix B, Figure B1) are such that the velocity scales equal κu^* with neutral forcing ($h/L = 0$ in Figure 2) and are enhanced and reduced in unstable ($h/L < 0$) and stable ($h/L > 0$) conditions, respectively. The turbulent velocities for momentum and scalars are equal in stable forcing. The unstable ϕ_m is greater than ϕ_s (Figure B1), so w_m becomes less than the corresponding w_s (dashed lines) in Figure 2. In order for w_x to scale with w^* in the convective limit, the ϕ_x functions in very unstable (convective) conditions of $\zeta < \zeta_x < 0.0$ have the form

$$\phi_x = (a_x - c_x\zeta)^{-1/3} \tag{14}$$

where the constants a_x and c_x make (14) match less unstable forms of ϕ_x at $\zeta = \zeta_x$ (equation B1). Combining (2), (6), (13), and (14) leads to

$$w_x = \kappa(a_x u^{*3} + c_x \kappa \sigma w^{*3})^{1/3} \rightarrow \kappa(c_x \kappa \sigma)^{1/3} w^* \qquad \sigma < \varepsilon$$
$$w_x = \kappa(a_x u^{*3} + c_x \kappa \varepsilon w^{*3})^{1/3} \rightarrow \kappa(c_x \kappa \varepsilon)^{1/3} w^* \qquad \varepsilon \le \sigma < 1 \tag{15}$$

where the arrows indicate the convective limit.

Eliminating the velocity scales from (12) and assuming a linear reduction of flux with distance in the surface layer [*Lumley and Panofsky*, 1964; *Tennekes*, 1973a] gives

$$\overline{wx}(\sigma)/\overline{wx}_0 = 1 - \beta_r \sigma/\varepsilon = a_1 + a_2 \sigma \tag{16}$$

where β_r is the fractional loss of flux at the furthest extent of the surface layer, $\sigma = \varepsilon$. To satisfy (16) at $\sigma = 0$ requires $a_1 = 1$, so that this loss is governed by $a_2 \simeq -\beta_r/\varepsilon$.

Equation (11) and its derivative with respect to σ at $\sigma = 1$ give the following expressions for a_2 and a_3:

$$a_2 = -2 + 3G(1) - \partial_\sigma G(1) \simeq -\beta_r/\varepsilon$$
$$a_3 = 1 - 2G(1) + \partial_\sigma G(1) \tag{17}$$

Atmospheric conditions are often well approximated by $G(1) = \partial_\sigma G(1) = 0$, and $\varepsilon = 0.1$, which lead to the *Troen and Mahrt* [1986] result, $G(\sigma) = (\sigma)(1 - \sigma)^2$, shown in Figure 2. In this case, $a_2 = -2$, $a_3 = 1$, and $\beta_r \simeq 2\varepsilon = 0.2$, which is in accord with *Lumley and Panofsky*'s [1964] definition of the atmospheric surface layer. We assume $\varepsilon = 0.1$ to be appropriate in the ocean, too. However, there is evidence of more complicated interior-driven boundary layers. For example, type I nocturnal boundary layers, as classified by *Kurzeja et al.* [1991], are characterized by light and variable winds, strong radiative cooling and a weak low-level jet. In such a case, *Kim and Mahrt* [1992] find that boundary layer similarity theory fails to represent the impact of the local shear on the underside of the nocturnal jet. They conclude that the local generation of turbulence at the top of the inversion layer resulting from this shear may be the principal cause of boundary layer diffusion.

Therefore in our ocean scheme the ocean interior is allowed to force the OBL through a dependence of $G(\sigma)$ and its vertical derivative at $\sigma = 1$ on the interior diffusivity, $\nu_x(d)$, and its vertical derivative at $d = h$. By matching these two interior quantities to the boundary layer diffusivity K_x and its vertical derivative, respectively (assuming γ_x is negligible compared with $\partial_z X$ at $\sigma = 1$), the fluxes, the time rate of change ($\partial_t X$), and the vertical derivatives of X through the second order are all continuous across the bottom of the boundary layer at $d = h$, $\sigma = 1$. This matching is achieved with

$$G_x(1) = \frac{\nu_x(h)}{h w_x(1)}$$
$$\partial_\sigma G_x(1) = -\frac{\partial_z \nu_x(h)}{w_x(1)} - \frac{\nu_x(h)\partial_\sigma w_x(1)}{h w_x^2(1)} \tag{18}$$

In unstable and neutral forcing, the $\partial_\sigma w_x(1)$ term vanishes (Figure 2). In stable forcing, the form of (B1) and (2) reduce this term to $5\kappa\nu_x(h)B_f u^{*-4}$, a function of the surface and interior forcing. In cases where the right-hand sides of (18) are nonzero, the shape functions become different for velocity and scalars because in general $\nu_m \neq \nu_s$ and $w_m \neq w_s$. When the interior diffusivities are different for temperature and salinity, the shape functions for these properties differ too.

The nonlocal transport term in (9) is nonzero only for scalars in unstable (convective) forcing conditions where, as was suggested by *Deardorff* [1972b], it has been successfully parameterized by *Mailhôt and Benoit* [1982] as

$$\gamma_s = C^* \frac{\overline{wx}_0}{w^* h} \tag{19}$$

with $C^* = 10$ in a highly convective case. In order that it apply to all forcing conditions, we use

$$\gamma_x = 0 \qquad \zeta \ge 0$$
$$\gamma_m = 0 \qquad \gamma_s = C_s \frac{\overline{ws}_0}{w_s(\sigma) h} \tag{20}$$
$$\gamma_\theta = C_s \frac{(\overline{w\theta}_0 + \overline{w\theta}_R)}{w_s(\sigma) h} \qquad \zeta < 0$$

with $C_s = C^* \kappa (c_s \kappa \varepsilon)^{1/3}$ from (15) in order to be consistent with (19) in the convective limit outside the surface layer. The $\overline{w\theta}_R$ term is discussed and defined in Appendix A. It represents the amount of radiative heat absorbed in the boundary layer that effectively contributes to the nonlocal transport of heat (equation (20)).

There is considerable evidence from observations [*Kaimal et al.*, 1976; *Lenschow et al.*, 1980] and LES [*Deardorff*, 1972a] of very small velocity gradients in the central portion of the convective ABL. This implies that momentum fluxes in this region are also maintained by nonlocal transport. However, such a term cannot be derived as *Deardorff* [1972b] did for the heat flux, so it is unlikely to have the form of (20). Until a suitable form is determined, nonlocal momentum flux is not parameterized ($\gamma_m = 0$).

Boundary Layer Depth

The extent of the oceanic PBL, h, depends on the surface forcing and on the oceanic buoyancy $B(d)$ and velocity $\mathbf{V}(d)$ profiles. A bulk Richardson number relative to the surface is defined as

$$Ri_b(d) = \frac{(B_r - B(d))d}{|\mathbf{V}_r - \mathbf{V}(d)|^2 + V_t^2(d)} \quad (21)$$

and h is equated to the smallest value of d at which this Richardson number equals a critical value Ri_c. The physics behind this definition is that boundary layer eddies with mean velocity $\mathbf{V}_r$ and buoyancy B_r should be able to penetrate to a depth h where they first become stable relative to the local buoyancy and velocity. The stabilizing mean buoyancy difference is taken relative to a near-surface B_r, but this is neither the parameterized surface buoyancy of convective elements in unstable forcing nor the first grid level buoyancy in the stable case, as are used by *Troen and Mahrt* [1986]. Instead, both B_r and the near-surface reference velocity $\mathbf{V}_r$ are estimates of the average buoyancy and velocity, respectively, over the surface layer, $0 < \sigma < \varepsilon$. In this way the direct use of resolution dependent grid level values is avoided. As is illustrated in Figure 1, property values at the first grid level depend a great deal on how well the surface layer is resolved.

The destabilizing shear term that leads to the denominator of (21) includes the magnitude squared of the vector mean velocity difference from $\mathbf{V}_r$. Unlike the *Troen and Mahrt* [1986] model, it also includes turbulent velocity shear, equal to V_t/d, which is often not negligible and is most important in pure convection and other situations of little or no mean shear. The turbulent shear is resolved and needs to be parameterized. It should increase with the turbulent velocity scale and decrease with boundary layer depth. It is also suspected that it would increase with greater local stratification, $\partial_z B = N^2$, where N is the local buoyancy frequency. These dependencies and dimensional considerations suggest

$$(V_t(d)/d)^2 \propto N w_x d^{-1} \quad (22)$$

The empirical rule of convection, $\overline{wb}_e/\overline{wb}_0 = \beta_T$ (Figure 1), can now be invoked to provide a more rigorous derivation and further dependencies on model parameters. Consider the special case of pure convection and no mean shear with a well-mixed layer of buoyancy B_r eroding into a layer of constant stratification, N^2. The numerator of (21) at $d = h$ then becomes $h(h - h_e)N^2$. The above convection rule, relations (9), (10), and (15), and the assumptions $\gamma_b \ll N^2$, $G(h_e/h) = (h - h_e)^2/h^2$, and $N(h_e) = N/C_v$, can then be used to eliminate $(h - h_e)$, leaving

$$V_t^2(h) = \frac{C_v(-\beta_T)^{1/2}}{Ri_c\kappa^{2/3}} (c_s\varepsilon)^{-1/6} h N w^*$$

The constant C_v should be greater than 1 and less than about 2 because it accounts for some smoothing of the buoyancy profile at h_e caused by mixing (Figure 1).

Using the scalar (15) to go from the pure convective to the general case gives

$$V_t^2(d) = \frac{C_v(-\beta_T)^{1/2}}{Ri_c\kappa^2} (c_s\varepsilon)^{-1/2} d N w_s \quad (23)$$

Without the V_t^2 term in (21), cases of larger N at the bottom of the boundary layer would tend to have smaller entrainment fluxes because the larger buoyancy gradient is insufficient to compensate for the very much smaller diffusivity resulting from the smaller h. However, with this term the larger N gives a larger h from (21), and hence for a fixed h_e the smaller h_e/h and the larger h increase the diffusivity (equation (10)) just enough to keep the entrainment flux independent of N. Although the ratio of this flux to the surface buoyancy flux will be a constant $-\beta_T$ in the convective limit, it will depend on u^* in forced convection.

With stable forcing ($B_0 > 0$, $L > 0$), the boundary layer depth is required to be less than both the Monin-Obukhov length and the Ekman depth [*Koracin and Berkowicz*, 1988],

$$h_E = 0.7u^*/f \quad (24)$$

where f is the Coriolis parameter. The Ekman depth is the extent of the boundary layer in neutral stratification, so with stable forcing tending to give stable stratification, h should be less than h_E. At depth beyond L, buoyant suppression of turbulence exceeds the mechanical production, and other sources of turbulent energy are small. Thus these depths should be placed outside the boundary layer because there is no surface-driven turbulent mixing. The restriction $h < L$ means that ζ cannot be greater than 1 in the boundary layer.

4. OCEAN MIXING BELOW THE BOUNDARY LAYER

In this section the vertical mixing in the ocean interior beyond the boundary layer is regarded as the superposition of three processes: local Richardson number instability due to resolved vertical shear, internal wave breaking, and double diffusion. Each process is reviewed and parameterized in terms of a local vertical diffusivity, ν_x^s, ν_x^w, and ν_x^d, respectively. The profile of effective overall interior diffusivity,

$$\nu_x(d) = \nu_x^s(d) + \nu_x^w(d) + \nu_x^d(d) \quad (25)$$

then gives the interior diffusivity and its gradient at $d = h$, which are used to force the boundary layer through (18). It also gives the turbulent vertical fluxes of momentum and scalars at depths $d > h$ as

$$\overline{wx}(d) = -\nu_x(d)\partial_z X \quad (26)$$

Other processes could be easily included by adding their diffusivities to (25). An alternative would be to assume that only the dominant process acts and equate ν_x to the largest of the process diffusivities.

Shear instability mixing occurs locally in stratified flow when the vertical velocity shear overcomes the stabilizing effect of the buoyancy gradient. The tendency for shear instabilities to develop is generally characterized by the local gradient Richardson number,

$$Ri_g = \frac{N^2}{(\partial_z U)^2 + (\partial_z V)^2} \tag{27}$$

and turbulent mixing can ensue when Ri_g is below some critical value Ri_0. The diffusivity for interior shear instability mixing is parameterized as a function of Ri_g and is the same for momentum and all scalars. This parameterization is shown in Figure 3, where

$$\nu_x^s/\nu^0 = 1 \quad Ri_g < 0 \tag{28a}$$

$$\nu_x^s/\nu^0 = [1 - (Ri_g/Ri_0)^2]^{p_1} \quad 0 < Ri_g < Ri_0 \tag{28b}$$

$$\nu_x^s/\nu^0 = 0 \quad Ri_0 < Ri_g \tag{28c}$$

$\nu^0 = 50 \times 10^{-4}$ m^2 s^{-1}, $Ri_0 = 0.7$, and $p_1 = 3$. The value of ν^0 is chosen to fall within the range of maximum observed diffusivities reported for the seasonal thermocline [*Peters et al.*, 1988]. Oceanic field measurements of Ri_g rarely fall as low as the theoretical value of 0.25 [e.g., *Koop and Browand*, 1979] but are often in the range 0.4–1.0 [e.g., *Eriksen*, 1978; *Davis et al.*, 1981a; *Kundu and Beardsley*, 1991]. The ν_x^s function of Ri_g (equation (28)) is not as steplike as is observed in laboratory results because it is to be applied to coarse-resolution models of the more complex ocean environment. Nonetheless, it is in general agreement with the limited observations [*Peters et al.*, 1988]. It results in rapid growth of the diffusivity as Ri_g decreases below the threshold value of Ri_0 (Figure 3). At low Ri_g there is a smooth transition into the regime of static instability, characterized by $Ri_g < 0$. These instabilities are removed by the high, but finite, ν^0, rather than by convective adjustment and its implicit infinite diffusivity. For $0 < Ri_g < Ri_0$, the shear instability parameterization (28) is more steplike than the Richardson number scheme presented by *Pacanowski and Philander* [1981] and results in comparatively higher (lower) diffusivities for values of Ri_g less than (greater than) about 0.4.

Mixing in the stratified water column away from the boundary layer is thought to be driven primarily by unresolved internal-wave shear. *Kunze et al.*'s [1990] Richardson number (RiNo) float data generally supports the general picture of the superposition of internal waves increasing shear and lowering the instantaneous Richardson number below a critical value resulting in turbulence and mixing. The magnitude of mixing due to internal waves can be calculated from the Garrett-Munk internal wave model [*Gregg*, 1989] and *Osborn*'s [1980] equation relating dissipation and diffusivity. Diffusivity ν_x^w due to internal wave breaking appears to be small, varying only with the internal wave energy, and constant relative to N [*Gregg*, 1989]. *Ledwell et al.* [1993] estimate a small diapycnal scalar diffusivity equal to 0.11×10^{-4} m^2 s^{-1} from purposeful tracer releases in the main thermocline of the open ocean. The magnitude of internal wave momentum viscosity is still not well known, but for $Ri_0 < Ri_g$, *Peters et al.* [1988] show it to be from 7 to 10 times larger than the scalar diffusivity. These quantities are therefore assigned the respective constant values of

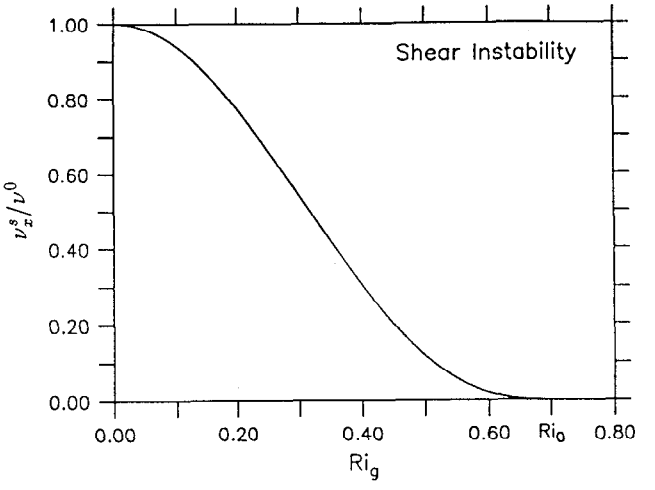

Figure 3. Interior diffusivity due to shear instability mixing, ν_x^s (equation (28)), normalized by its maximum, $\nu^0 (= 50 \times 10^{-4}$ m^2 s^{-1}), as a function of the local gradient Richardson number (equation (27)).

$$\nu_m^w = 1.0 \times 10^{-4} \text{ m}^2 \text{ s}^{-1}$$
$$\nu_s^w = 0.1 \times 10^{-4} \text{ m}^2 \text{ s}^{-1} \tag{29}$$

These values are less than the *Pacanowski and Philander* [1981] functions for $Ri_g < 10$. They enter (25) and become the effective background diffusivities throughout the ocean interior. Alternatively, *Gargett and Holloway* [1984] argue that ν_x^w should vary as N^{-1}; a form that could easily be implemented.

Double-diffusive mixing can occur when the vertical gradient of density is stable but the vertical gradient of either salinity (salt fingering) or temperature (diffusive convection) is unstable in its contribution to density [*Turner*, 1973]. Although the cause of double diffusion in the ocean is the more rapid molecular diffusion of temperature relative to salinity, the net effect on turbulent length scales is to reduce the potential energy of the vertical profile by preferentially mixing the destabilizing component. Regions of active salt fingering and diffusive convection can be identified using the double-diffusion density ratio R_ρ:

$$R_\rho = \alpha \partial_z T / (\beta \partial_z S) \tag{30}$$

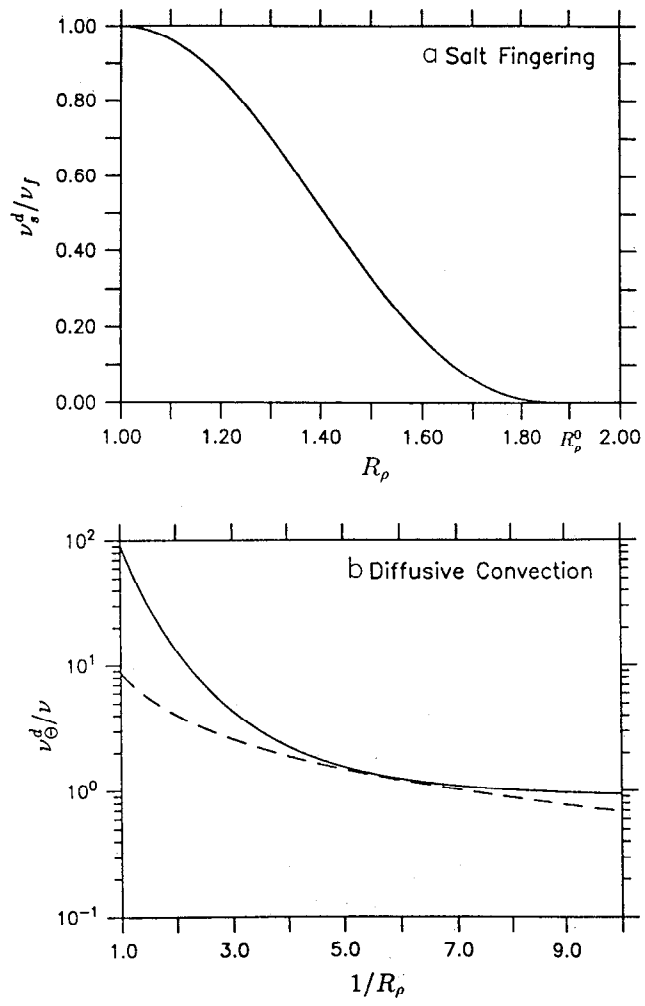

Figure 4. (a) Interior diffusivity for double-diffusive mixing due to salt fingering, $\nu_s^d = \nu_m^d$ (equation (31)), normalized by its maximum, $\nu_f = 10 \times 10^{-4}$ m^2 s^{-1}, as a function of the density ratio R_ρ (equation (30)). (b) Interior diffusivity of potential temperature for double-diffusive mixing due to diffusive convection, ν_θ^d, normalized by the molecular diffusivity ν ($= 1.5 \times 10^{-6}$ m^2 s^{-1}), as a function of R_ρ^{-1}. The solid trace represents (32); the dashed trace, (33).

where α and β are the thermodynamic expansion coefficients for temperature and salinity, respectively. The mixing of momentum from double diffusion is treated in the same fashion as salinity, such that $\nu_m^d = \nu_s^d$. All solutes are also mixed like salinity, but temperature is distinctly different.

Salt fingering is found in the subtropical and tropical thermoclines where warm, salty water overlies cold, fresh water ($\alpha\partial_z T > 0$ and $\beta\partial_z S > 0$) and $1 < R_\rho < 2$ [*Schmitt*, 1981, 1990]. Little is known about the relationship between R_ρ and the diffusivities for salt and temperature, ν_s^d and ν_t^d, in this regime. On the basis of the limited observational data, $\nu_s^d(R_\rho)$ appears to be large ($\sim 10^{-3}$ m^2 s^{-1}) for R_ρ less than 1.5, falling dramatically near $R_\rho = 1.7$ and reaching low background levels (10^{-5} m^2 s^{-1}) by $R_\rho = 1.9$ [*Schmitt*, 1981]. The mixing of temperature is generally found to behave in a similar fashion but to be somewhat less. We should note, however, that the ν_s^d estimates are computed indirectly by applying a laboratory flux law to observed salinity steps in staircase regions and then dividing by the mean salinity gradient [*Schmitt*, 1988]. With this caveat in mind, mixing due to salt fingering is parameterized by (Figure 4a)

$$\nu_s^d(R_\rho)/\nu_f = \left[1 - \left(\frac{R_\rho - 1}{R_\rho^0 - 1}\right)^2\right]^{p_2} \quad 1.0 < R_\rho < R_\rho^0 \tag{31a}$$

$$\nu_s^d(R_\rho)/\nu_f = 0.0 \quad R_\rho \geq R_\rho^0 \tag{31b}$$

$$\nu_\theta^d(R_\rho) = 0.7\nu_s^d \tag{31c}$$

where $\nu_f = 10 \times 10^{-4}$ m^2 s^{-1}, $R_\rho^0 = 1.9$, and $p_2 = 3$. A value of R_ρ less than or equal to 1 in the salt-fingering case results in $Ri_g \leq 0$ and convective instability where ν_x^s dominates (25).

Diffusive-convective staircases occur primarily in the Arctic and adjacent regions where temperature is destabilizing (cold, fresh water over warm, salty water: $\alpha\partial_z T < 0$, $\beta\partial_z S < 0$, and $0 < R_\rho < 1$) [*Padman and Dillon*, 1987]. As in the salt-fingering case, no direct measurements of ν_s^d or ν_θ^d exist for diffusive-convective staircases, but an effective diffusivity can be computed from a combination of laboratory measurements, theory, and field data. The temperature flux F_T across a diffusive interface can be related to R_ρ and the temperature jump ΔT using the flux law, $F_T \propto f(R_\rho)(\Delta T)^{4/3}$ [*Turner*, 1965]. The function $f(R_\rho)$ is an empirical fit to laboratory data that accounts for the dependence of the flux on R_ρ [*Marmorino and Caldwell*, 1976]. *Fedorov* [1988] uses a simple model for diffusive layer thickness and *Marmorino and Caldwell*'s [1976] $f(R_\rho)$ function to compute ν_θ^d as

$$\nu_\theta^d/\nu = 0.909 \exp(4.6 \exp[-0.54(R_\rho^{-1} - 1)]) \tag{32}$$

where ν is molecular viscosity (about 1.5×10^{-6} m^2 s^{-1}. *Kelley* [1988, 1990] offers an alternative formulation based on observed, oceanic step size data and a different empirical fit for $f(R_\rho)$,

$$\nu_\theta^d/\nu = 8.7R_\rho^{1.1} \tag{33}$$

The two formulations are shown in Figure 4b. They differ by an order of magnitude near $R_\rho = 1$ but converge for $R_\rho < 0.25$. Since an early objective is to assess whether or not it is necessary to include double-diffusive processes, *Fedorov*'s [1988] formulation (equation (32)) is implemented because it gives larger effects. Other diffusivities are then found from

$$\nu_s^d = \nu_\theta^d(1.85 - 0.85R_\rho^{-1})R_\rho \quad 0.5 \leq R_\rho < 1.0$$

$$\nu_s^d = \nu_\theta^d\, 0.15R_\rho \quad R_\rho < 0.5 \tag{34}$$

5. MODEL VERIFICATION AND SENSITIVITIES

The core of the vertical mixing scheme developed in sections 3 and 4 is the nonlocal K profile parameterization (KPP) of the boundary layer, so we shall refer to our complete one-dimensional ocean model as the KPP model. The other model components are the interior mixing and the rules for matching it to the boundary layer. The purpose of this section is threefold. The first purpose is to determine reasonable values for model parameters, especially C_v and Ri_c. Simulations of convection are used for the former, and simulations of high wind forcing are used for the latter. A simulation of diurnal cycling under strong stable solar forcing is used to investigate these and other parameters. The second purpose is to investigate the resolution dependencies of these parameters. The third motivation is to demonstrate that with these choices fixed, a KPP simulation of an upper ocean annual cycle is comparable to observations in its vertical temperature distribution. Further sensitivity studies, especially to resolution, can be found in Appendix C.

The following equations are discretized and integrated implicitly:

$$\partial_t U = \partial_z[-\overline{wu}] + fV \tag{35a}$$

$$\partial_t V = \partial_z[-\overline{wv}] - fU \tag{35b}$$

$$\partial_t T = \partial_z[-\overline{w\theta}] - \partial_z Q_n - A_T \tag{35c}$$

$$\partial_t S = \partial_z[-\overline{ws}] - \partial_z F_n - A_S \tag{35d}$$

where the kinematic fluxes $\overline{wx}$ are parameterized by (9) in the boundary layer ($d \le h$) and by (26) beyond ($d > h$). The Coriolis terms are fV and fU. The nonturbulent heat and freshwater flux profiles, $Q_n(d)$ and $F_n(d)$, are discussed in Appendix A. The vertical plus horizontal advection tendencies are combined in the A_T and A_S terms. Except for some multiyear simulations in section 6, these terms are set to $A_T = A_S = 0$. Vertical discretization and numerical implementation are outlined in Appendix D. In this section the discrete numerical model is used in an upper ocean configuration with constant grid spacing ($\lambda = 0$ (equation (D1)).

Convection

Oceanic convection is common, so it should be well modeled. Stabilizing downwelling longwave radiation is usually overcome by several tens of watts per square meter by the longwave emissions from the sea surface. Even when the sensible heat flux is positive, it is almost always compensated for by a greater negative latent heat flux. The evaporation responsible for such a latent heat flux is also accompanied by a destabilizing loss of fresh water. Thus, the OBL is convective every night and often during the day.

TABLE 1. Sensitivity of $\beta_T = (\overline{wb}_e/\overline{wb}_0)$ to the Critical Richardson Number Ri_c and to C_v in Pure Convective Entrainment

Ri_c	$C_v = 1.4$	$C_v = 1.6$	$C_v = 1.8$
0.25	−0.171	−0.206	−0.243
0.50	−0.170	−0.206	−0.241
0.75	−0.171	−0.207	−0.241

The value of C_v in (23) is chosen to make $\beta_T = -0.2$ in the pure convective limit of $u^* = 0$, $B_0 < 0$. Consider a motionless, constant salinity (35 practical salinity units, PSU) ocean that is continuously stratified with $\partial_z T = 0.1°\text{C m}^{-1}$ and $N = 0.016\ \text{s}^{-1}$ from a surface temperature of 22°C. Under the action of a steady cooling, $Q_t = -100\ \text{W m}^{-2}$, the surface cools, and the resulting convection leads to a deepening turbulent boundary layer. This situation is somewhat akin to a windless, cloudless night where the dominant forcing is a net longwave radiative heat loss. The mean buoyancy and buoyancy flux profiles shown as an example in Figure 1 are actually from day 3.0 of a high-resolution ($\Delta z = 0.2$ m, $Ri_c = 0.25$, $C_v = 1.6$) KPP simulation of such a convective case. These profiles are classic examples of the convective boundary layer and are very reminiscent of atmospheric observations and simulations. Table 1 shows the sensitivity of β_T at $t = 3$ days to both C_v and Ri_c. There is nearly a linear dependency on the former and no dependence on the latter because, as expected, the influence of Ri_c is captured by (23). Table 1 establishes that a value of C_v between 1.5 and 1.6 results in the desired $\beta_T = -0.2$.

In the pure convection case described above, KPP was made to behave properly by the choice of C_v. For confidence that entrainment is realistic in other conditions, such as when surface cooling is accompanied by a wind, the model is now compared with two observations of forced oceanic convection. *McPhee and Martinson*'s [1994] momentum and heat flux measurements under drifting pack ice in the Weddell Sea were taken in a predominantly shear-driven boundary layer ($0 > \zeta > -0.01$) with a destabilizing heat flux of the order of $-10\ \text{W m}^{-2}$. The derived momentum diffusivities at depths of 4, 8, 16, 20, and 24 m were 160, 200, 250, 200, and $150 \times 10^{-4}\ \text{m}^2\ \text{s}^{-1}$, respectively. The neutral KPP boundary layer scheme with $u^* = 0.012\ \text{m s}^{-1}$ and $h = 40$ m gives diffusivities of comparable magnitude and a similar vertical structure, namely, 160, 210, 280, 250, and $100 \times 10^{-4}\ \text{m}^2\ \text{s}^{-1}$, respectively.

Observations of a more convective nighttime oceanic boundary layer are presented by *Anis and Moum* [1992], who used 78 profiles of potential temperature and salinity taken throughout a March 1987 night (their night 3) between 7 and 10°N along 140°W to produce the average data shown by triangles in Figure 5. Be-

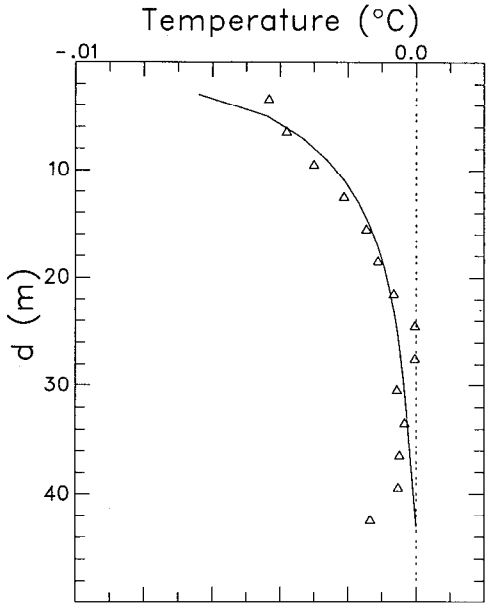

Figure 5. Potential temperature profiles during nighttime convection as observed by *Anis and Moum* [1992] (triangles) and as simulated K profile parameterization (KPP, solid trace).

fore averaging, each profile was referenced to the mean potential temperature and salinity of the mixed layer in an attempt to minimize the effects of the ship moving through oceanic features. Furthermore, the data were averaged over 3-m-thick bins. To simulate these results, a KPP model with 2.0-m resolution was initialized at sundown and forced for 12 hours with the surface wind stress and buoyancy fluxes computed by *Anis and Moum* [1992] from shipboard meteorological observations. The averages of these two forcing functions were 0.08 N m^{-2} and -1.4×10^{-7} W kg^{-1}, respectively. Model profiles at each 0.5-hour time step were also referenced to mixed layer averages and then averaged over the run to give the solid trace of Figure 5. Absolute potential temperatures are not comparable because of the ship's travels. Therefore in Figure 6, both model and observed profiles are plotted relative to their maximum potential temperature, making the horizontal offset arbitrary. Both observations and KPP give an unstable temperature difference of the order of 5×10^{-3} °C between depths of 3 m and 25 m. Deeper than 25 m a more isothermal water column is evident in both observations and model. The thermocline in the observed average is just appearing at 43 m. It is shallower than that modeled because after nightfall, when the model was initialized, the ship entered a region of decreasing mixed-layer depth [*Anis and Moum*, 1992]. As the surface is approached the modeled gradient becomes more unstable. An open question is whether observations nearer the surface would show a similar behavior. The data tend to suggest not, perhaps because of unmodeled near-surface processes such as surface wave stirring.

Wind Deepening

In atmospheric applications, Ri_c has varied from 0.25 in the fine vertical resolution model of *Holtslag et al.* [1990] to 0.50 in the coarser *Troen and Mahrt* [1986] configuration. It now will be shown that values in this range yield acceptable oceanic results at both fine and coarse resolution. Fortunately, the results from many upper ocean observational [e.g., *Davis et al.*, 1981a; *Large et al.*, 1986; *Paduan and deSzoeke*, 1986; *Large and Crawford*, 1994] and modeling studies [e.g., *Niiler*, 1975; *Davis et al.*, 1981b; *Price*, 1981; Crawford and Large, submitted manuscript, 1994] are available for this purpose.

First, following *Pollard et al.* [1973], a steady of 0.3 N m^{-2} wind stress blows over an initially motionless ocean with a constant $N = 0.016$ s^{-1} given by a 0.10°C m^{-1} temperature gradient. The boundary layer depth from KPP, like the mixed layer depth of *Pollard et al.* [1973], has the characteristics

$$h \propto u^*(t/N)^{1/2} \qquad h_{\max} \propto u^*/(Nf)^{1/2}$$

where time t represents only the initial deepening and $h_{\max}$ is the depth after 0.5 inertial periods, when the deepening is arrested by rotation of the currents into the wind. Table 2 shows that as Ri_c increases from 0.25 to 0.75, $h_{\max}$ increases by more than a third, or 8 m. Other sensitivities are much smaller. Lower resolution always tends to decrease $h_{\max}$, and a larger C_v

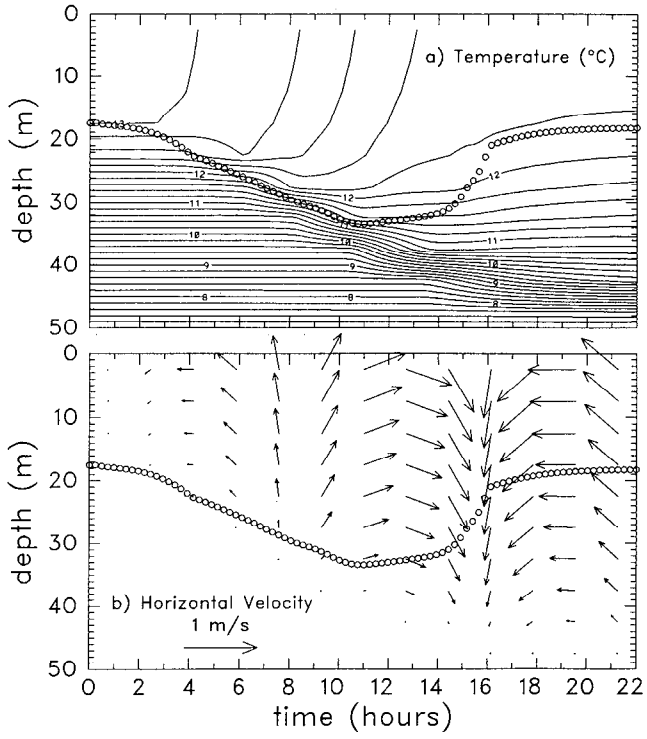

Figure 6. Time-depth sections of (a) temperature and (b) horizontal velocity, where an upward vector indicates northward flow from an idealized simulation of resonant ocean response to an inertially rotating wind given by (36). The open circles trace the evolution of the boundary layer depth h.

TABLE 2. Boundary Layer Depth, h_{max}, in Meters at 0.5 Inertial Periods After the Onset of a Steady 0.3 N m^{-2} Wind, as a Function of C_v, Ri_c, and Resolution, With and Without the Interior Mixing Activated

	No Interior Mixing			*Interior Mixing*		
	C_v = 1.6			C_v = 1.6		
Ri_c	Δz = 1 m	Δz = 4 m	C_v = 2.0, Δz = 4 m	Δz = 1 m	Δz = 4 m	C_v = 2.0, Δz = 4 m
0.25	23.4	22.7	23.1	24.7	22.6	23.3
0.50	28.3	28.1	28.1	30.2	27.7	28.3
0.75	31.8	31.4	31.4	32.9	31.1	31.7

can only partially compensate. Including interior mixing increases h_{max} by 1–2 m with 1-m resolution but can decrease it slightly with 4-m resolution and C_v = 1.6. The experiments with no interior mixing are most like those of *Pollard et al.* [1973], who find h_{max} to be about 25 m. The K profile model agrees with this result when Ri_c is greater than 0.25 but less than 0.50.

A more quantified determination of Ri_c is provided by comparisons with observed ocean responses during the Ocean Storms experiment [*D'Asaro*, 1985a]. The data analysis of *Large and Crawford* [1994] provides the initial conditions, forcing, and response to seven wind events whose peak wind stresses all exceed 0.4 N m^{-2}. The observed mixed layer temperature changes have a wide range from −0.03 to −1.11°C. The increase in potential energy of the water column above 150 m, ΔPE, is a good measure of this response for comparison with model simulations. It includes both mixed-layer cooling and thermocline heating and can be readily computed from thermistor chains, and the effects of horizontal advection often can be estimated and removed. Lagrangian drifters also provide an estimate of the change in mixed-layer kinetic energy at the inertial period, ΔIKE_m; however, that is perhaps not such a good measure of response because it excludes energy at other periods and below the mixed layer.

The changes in potential and mixed-layer inertial kinetic energy have been computed from KPP simulations of the seven Ocean Storms events for a range of Ri_c values and resolutions. For each parameter choice, Table 3 gives the ratio, modeled to observed, of the average responses, ΔPE and $\Delta(PE + IKE_m)$, over the seven events. The changes in potential energy show that the average observed and modeled responses could be made equal at all resolutions using a value of Ri_c between 0.25 and 0.50. Interpolating these results suggests Ri_c = 0.3 at Δz = 1 m, increasing slightly to about 0.4 as the resolution is degraded to Δz = 5 m. The sum of the energy changes shows the same tendency but suggests somewhat larger values of Ri_c. Hereinafter, the standard choice at all resolutions will be Ri_c = 0.3.

The Ocean Storms events with the largest SST decreases are similar to the episodic cooling events reported by *Large et al.* [1986]. There is little change in mixed-layer depth and considerable heating in the thermocline, which *Large and Crawford* [1994] find are characteristics of resonant ocean response to inertial period rotation of the wind. In analogy with penetrative convection, the dominant process might be termed penetrative wind mixing because it is the penetration of the boundary layer deep into the stratified thermocline that is responsible for the vigorous exchange of properties between the mixed layer and thermocline.

The following idealized simulation illustrates how the KPP, with moderate resolution of Δz = 5 m, responds to an idealized inertially rotating wind stress given by

$$\tau(t) = [\tau_x, \tau_y] = A_m \sin(\pi t/T_i) \cdot [\sin(2\pi t/T_i), \cos(2\pi t/T_i)] \quad 0 < t < T_i \quad (36a)$$

$$\tau(t) = [\tau_x, \tau_y] = [0.0, 0.0] \quad t > T_i \quad (36b)$$

where T_i = 16 hours is the inertial period and A_m = −0.6 N m^{-2} corresponds to a peak wind at t = 8 hours of about 20 m s^{-1} blowing to the north. At t = 0 hours and again at $t = T_i$ the wind blows toward the south but with no speed. There is no other forcing, no initial velocities, and a constant salinity. The initial temper-

TABLE 3. Ratios of Average Model Response to the Average of Observed Changes in Potential Energy and Changes in the Sum of Potential Plus Mixed-Layer Inertial Kinetic Energy as a Function of Ri_c and Model Vertical Resolution

	ΔPE			*(ΔPE + ΔIKE$_m$)*		
Ri_c	Δz = 1 m	Δz = 2 m	Δz = 5 m	Δz = 1 m	Δz = 2 m	Δz = 5 m
0.25	0.92	0.89	0.81	0.96	0.90	0.85
0.50	1.27	1.21	1.08	1.06	1.02	0.99
1.0	2.03	1.96	1.80	1.30	1.29	1.25

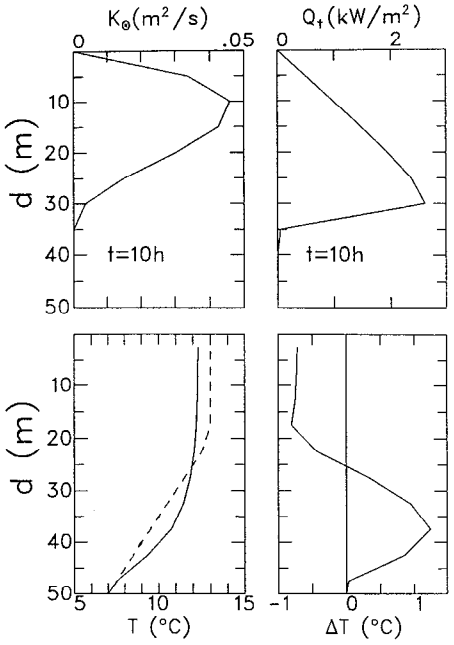

Figure 7. Profiles taken during the simulated resonant ocean response to an inertially rotating wind shown in Figure 6. (top) Instantaneous profiles at $t = 10$ hours of (left) thermal vertical diffusivity K_θ and (right) vertical heat flux Q_t. (bottom) (left) Initial (dashed trace) and final (solid trace) model temperature profiles and (right) their difference, ΔT.

ature profile is given by $T = 13.0$°C from the surface to 20-m depth, then a linear decrease to $T = 7.0$°C at 50-m depth.

Figure 6 shows time-depth sections of temperature and horizontal velocity from this simulation. Unlike the previous steady wind case, the boundary layer deepening and current acceleration are not arrested at $0.5T_i$ because the wind rotates with the near-surface currents and never opposes them. Instead, the boundary layer retreats, and the currents stop accelerating later as the wind stress diminishes in strength. As the currents and velocity shear increase, the boundary layer deepens according to (21), so that for many hours it is well below the initial mixed-layer depth of 20 m. The juxtaposition of large boundary layer diffusivities and upper thermocline temperature and velocity gradients leads to very large downward fluxes of heat and momentum with the following consequences. First, considerable momentum is transferred out of the mixed layer, so that when the wind stops at $t = 16$ hours there are significant free inertial currents in the upper thermocline. Thus velocity shear is found, not at the base of the mixed layer as in many models, but in the upper thermocline as was observed by *D'Asaro* [1985b]. Second, there is rapid mixed-layer cooling of more than 0.6°C in 10 hours and an associated thermocline heating that is as much as 1.2°C at 37.5-m depth. The temperature change profile (Figure 7, bottom right) is very similar to the composite heating profile from 20 observed episodic cooling events from *Large et al.* [1986]. Finally, Figure 7 (bottom left) shows that the initial sharp break in temperature gradient (dashed trace) imposed at 20-m depth is smoothed so that the temperature profile at $t = 18$ hours (solid trace) is more like observations [e.g., *Large et al.*, 1986].

The model response also agrees quantitatively with observations. It is most energetic at about $t = 10$ hours, when the instantaneous downward heat flux $Q_t(d)$ between 20- and 30-m depth exceeds 2000 W m^{-2}, and when K_θ at 20 m is about 300×10^{-4} m^2 s^{-1}. Such a large boundary layer diffusivity at the base of the initial mixed layer does not need to persist for very long to give the large, 1- to 2-day, average values of K_θ reported at the base of the mixed layer ($20–70 \times 10^{-4}$ m^2 s^{-1} [*Large et al.*, 1986], $15–20 \times 10^{-4}$ m^2 s^{-1} [*Gregg*, 1987]) and in the seasonal thermocline ($\sim 4 \times 10^{-4}$ m^2 s^{-1} [*Large et al.*, 1986]; 16×10^{-4} m^2 s^{-1} [*Large and Crawford*, 1994]). *Large et al.* [1986] estimate average heat fluxes of more than 1000 W m^{-2} from observed mean temperature changes. The heat flux profile at $t = 10$ hours (Figure 7) is reminiscent of the buoyancy flux profile of Figure 1 in that it is nearly linear from the surface to the entrainment depth, which lies between h_m and h. Of course, at all depths in this wind-driven case, $Q_t(d)$ is positive and $\overline{wb}$ is negative because there is no surface heat or buoyancy flux.

Diurnal Cycling

The occurrence of stabilizing forcing depends a great deal on the radiative contribution B_R to the surface buoyancy flux B_f (equation A3)). If no solar heat is allowed to contribute ($h_B = 0$), then only periods of substantial precipitation would be expected to be stable. It is clearly incorrect to include all the solar heating in B_R, especially when the boundary layer is thin and a large fraction of the radiation passes through the boundary layer. However, it is physically possible for heat absorbed within the boundary layer to directly influence the turbulence throughout the layer. Assuming that this influence does not depend on where the heat is absorbed leads to $h_B = h$, which is now to be tested against observations of diurnal cycling.

Stable forcing conditions are commonly produced by strong solar heating in low-wind conditions and are often followed by convection when the Sun goes down. The net result is a large diurnal cycle in SST. The capability of KPP to simulate these diurnal oscillations is desirable so that their role in climatological air-sea exchange can be addressed. It is demonstrated by comparison to observations from the Long-Term Upper Ocean Study (LOTUS) site in the Sargasso Sea (34°N, 70°W) [*Briscoe and Weller*, 1984]. LOTUS data have been used to validate other one-dimensional models of the upper ocean (section 6). The data set

consists of an approximately 2-year-long time series of meteorological variables and of temperature and velocity measured at various depths through the water column from a mooring.

A short, 7-day portion of the LOTUS temperature records from shallow thermistors (0.6-, 5-, 10-, and 15-m depths) for July 1982 is shown in Figure 8. The SST (0.6-m temperature) undergoes large diurnal oscillations of 0.5°–2.5°C during the initial part of the record when wind speed was low and daytime insolation was high [*Stramma et al.*, 1986]. These diurnal temperature fluctuations are trapped above 1- to 2-m depth and are not apparent in the 5-m thermistor record. Increasing wind speed on year day 200 deepens the mixed layer and damps the diurnal SST response.

Surface forcing for the LOTUS simulations is computed as outlined in Appendix A and is similar to that used by *Stramma et al.* [1986] and *Gaspar et al.* [1990]. The heat content of the upper 50 m at the LOTUS site just prior to day 194.5 shows a large decrease, which is inconsistent with the calculated surface heat flux and most likely reflects horizontal advective effects. Following day 194.5, however, the estimated net heat flux nearly balances the observed increase in the 0- to 50-m heat content. The KPP simulations therefore have been initialized at day 194.5, and no advective heat flux corrections have been applied. They have been integrated forward in time until the end of the low-wind period at 201.5. These LOTUS simulations are initialized using observed temperature and velocity components linearly interpolated onto the model grid (surface to 50 m) and a climatological surface salinity of 36.3 PSU everywhere in lieu of salinity measurements.

The simulated temperature records at the shallow LOTUS thermistor depths from our standard LOTUS configuration ($C_v = 1.5$; $Ri_c = 0.3$) are also shown in Figure 8. In this case there are 20 vertical levels, each with $\Delta z = 2.5$ m. Solar radiation is included in B_f, with $h_B = h$. We chose not to include radiation in the countergradient term by setting $h_\gamma = 0$ (equation A4)), because there is negligible impact on modeled diurnal cycles and because further refinement of the nonlocal transport (equation (20)) is being considered. Therefore $\overline{w\theta}_R$ in (20) is zero. The performance of KPP relative to the observations is acceptable, given the uncertainty in the forcing. The K profile boundary layer captures both the magnitude of the diurnal SST variability and the shallow trapping depth found in the thermistor data. The model solution also entrains the 5-m and 10-m thermistors into the surface layer at about the correct times. The model SST differs from the observed after year day 200, when clouds lower the solar heating and perhaps lead to large errors in the estimated surface heat flux.

The standard LOTUS simulation is almost identical to a high-resolution run ($\Delta z = 0.50$ m), so the KPP

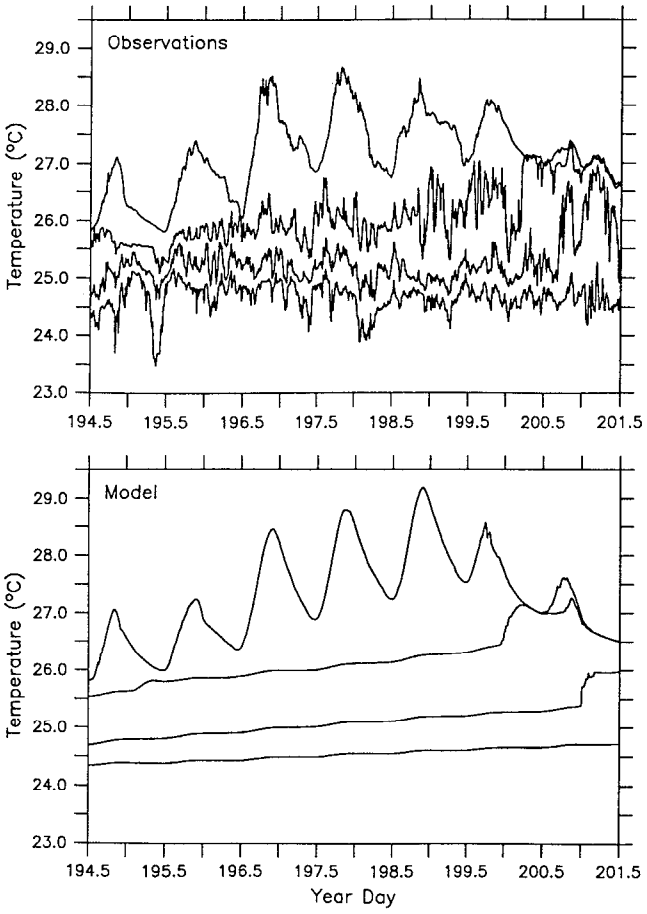

Figure 8. Seven-day time series from 1200 UTC on July 13, 1982, of LOTUS (34°N, 70°W) ocean temperatures at depths of 0.6, 5.0, 10.0, and 15.0 m. Shown are (top) the observations and (bottom) a KPP simulation, with $h_B = h$, $h_\gamma = 0$.

results (Figure 8) are not very resolution dependent. Sensitivity to the treatment of solar radiation through the choices of h_B (equation A3)) and h_γ (equation (A4)) and to the choices of C_v and Ri_c, and the role of interior mixing are presented in Appendix C. These experiments support allowing all radiation absorbed in the boundary layer to influence stability ($h_B = h$). The model solutions are then insensitive to solar radiation included in the nonlocal transport parameterization (20), so $h_\gamma = 0$ is our preferred choice.

Annual Cycling

The performance of the KPP over the highly variable conditions of an annual cycle will now be assessed. Of particular interest here is the comparison with observed temperatures and the dependency on resolution. An attractive site for this simulation is ocean weather station (OWS) Papa (50°N, 145°W) because the forcing functions are relatively well known; there is a large annual range of SST, h_m, and forcing conditions; there is an abundance of local oceanographic data available over many years; and horizontal effects are relatively small in the area [*Gill and Niiler*,

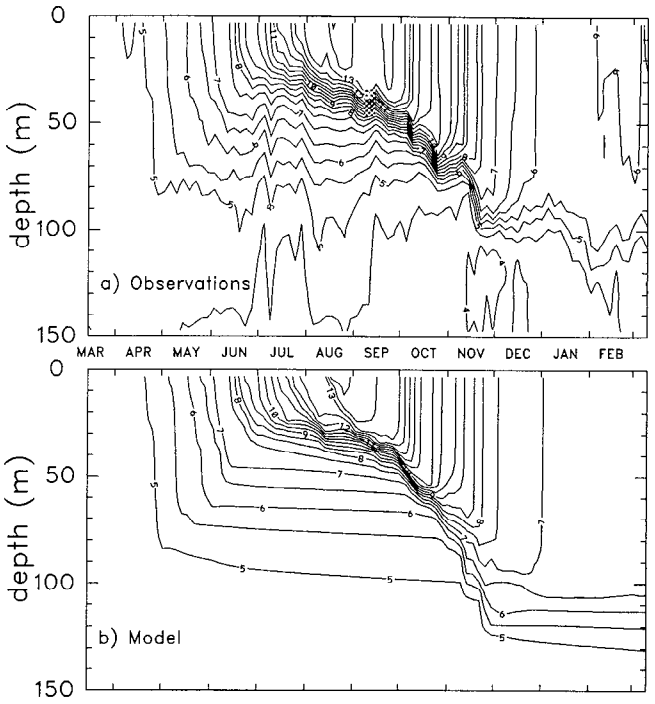

Figure 9. Time-depth sections of 4-day averages of observed temperatures in degrees Celsius (a) from ocean weather station (OWS) Papa during the ocean year March 15, 1961, to March 15, 1962 and (b) from the standard KPP simulation of OWS Papa.

1973]. For these reasons this site is popular for upper ocean model testing. *Martin* [1985], for example, compares simulations of the period from January 1 to December 31, 1961, from four models (section 6).

Our standard OWS Papa simulation uses model parameters as determined above ($Ri_c = 0.3$, $C_v = 1.5$, $h_B = h$, $h_\gamma = 0$), and these values are retained throughout the remainder of this paper. There is a moderate 5-m resolution over a 200-m depth and a 1-hour time step. The annual run begins on March 15, 1961, at the beginning of the ocean year when the heat content above 200 m is a minimum, the SST is 4.6°C and the mixed-layer depth is about 130 m (Figure 9). This start date is preferable to the beginning of the calendar year, when the ocean is still cooling and advective events still appear to be important. Model initial conditions are 20-day average observed temperatures, the salinity profiles from *Tabata* [1965], and zero flow. The observed temperature data shown in Figure 9a were produced by averaging the frequently observed temperature profiles over 4-day periods, which effectively filters out the internal tide and inertial oscillations by averaging over about eight and six periods, respectively.

The surface forcing at OWS Papa is described in Appendix A. Over the simulated 1961 ocean year there is greater than average net heat flux of 34 W m^{-2} and freshwater flux of about 11 mg m^{-2} s^{-1}. Since there is no advection in the standard OWS Papa simulation ($A_T = A_S = 0.0$), it is expected that the results should begin to diverge from observations in the fall as is discussed in Appendix A.

Simulations in spring and summer are sensitive to water clarity, so an annual cycle of *Jerlov* [1976] water type is specified as moderately clear type IA from December through February, turbid type II from June through September, and intermediate type IB in the other months. Such an annual cycle in the North Pacific is indicated by the Secchi depth (depth to which a white disk is visible) analysis of *Lewis et al.* [1988]. The winter values are supported by measurements at 35°N, 155°W in February [*Simpson and Paulson*, 1979] and Secchi depth readings at OWS Papa in excess of 20 m. In summer the Secchi depth is only 10–12 m, indicating more turbid Type II water. However, any such annual cycle is somewhat uncertain because of the difficulty in converting Secchi depths to light extinction coefficients [*Preisendorfer*, 1986] and then to Jerlov water types.

Figure 9 shows both the observed and modeled time-depth sections of temperature. The latter (Figure 9b) shows comparatively less variability at depth. The formation of the seasonal thermocline during spring and summer is very well reproduced, as is the thermal structure above 20 m. The erosion of the thermocline and its internal structure is well modeled until the end of October, after which the annual (34 W m^{-2}) imbalance in model heating leads to the expected warm temperatures from the surface to the halocline below 100-m depth. These features support the suggestion of *Large et al.* [1986] that the fall and winter advection of deep, cold water may be at the depth of the seasonal thermocline where it first acts to stabilize the water column and later to cool the surface when mixed.

Figure 10a shows that 1961 was not an average year for heat advection because of the observed net gain in heat content above 200 m. The heat flux inferred from changes in observed heat content (Figure 10b, dashed trace) is averaged over 6 days. This flux often differs from 6-day averages of the estimated surface flux by many hundred watts per square meter when advective effects must have been dominant. The associated temperature changes are seen in Figure 9a as vertically coherent signals, which are indicative of advection. Until November 1, 1961, advective heating and cooling appear to nearly balance, though heat content excesses and deficits, relative to the one-dimensional model, can persist for as long as a month (Figure 10a). After November 1 the anticipated bias due to net advective cooling is evident, but a heating tendency from late January through February leads to the annual heat content gain of about 500 MJ m^{-2}, which corresponds to a heating rate of 16 W m^{-2}. Thus the warm model bias in 1961 is only 18 W m^{-2}. If this amount of advective cooling were judiciously applied to the model, the simulations could be made to match observations throughout the year. Without such cool-

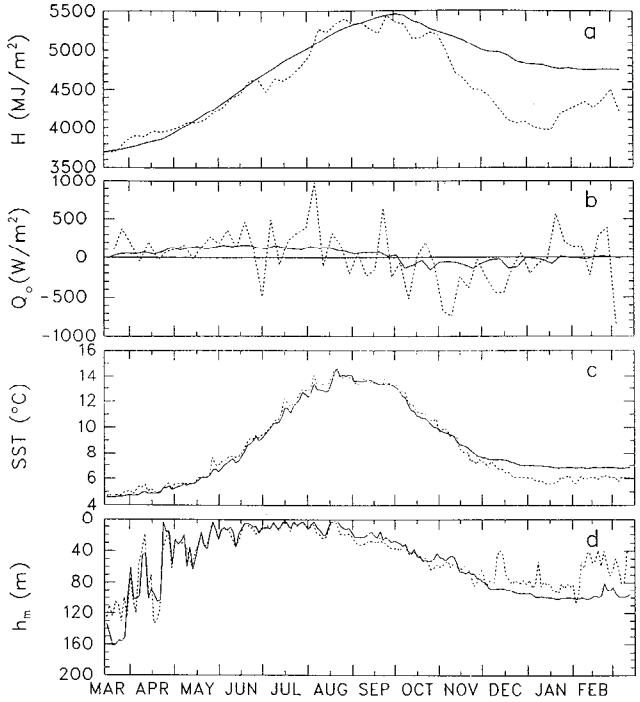

Figure 10. Time series, March 15, 1961, to March 15, 1962, of observed (dotted traces) and modeled (solid traces) (a) heat content above 200-m depth, (b) the time derivatives of Figure 10a, which are the total heat fluxes, (c) sea surface temperature (SST), and (d) mixed-layer depth.

ing the modeled and observed heat contents agree only through October, and the overall gain in modeled heat content over the year reflects the net 34 W m^{-2} of surface heating minus 2 W m^{-2} of vertical diffusion across 200-m depth.

The SST and h_m comparisons are shown in Figures 10c and 10d, where the data are averaged over 2 days, or about three inertial and four semidiurnal tidal periods, to reduce signal contamination. Here, to be consistent with *Martin* [1985], h_m is the shallowest depth at which the temperature is 0.1°C less than SST. The excellent agreement extends past the November 1 limit of similar heat contents and into December 1961 because the colder observed temperatures are confined to below the mixed layer. Throughout the spring and summer there is considerable high-frequency correlation between model and observed SSTs and mixed-layer depths, indicating that the KPP is performing well. At the start of the simulation, the model h_m from the 20-day average initial conditions is about 15 m deeper than the instantaneous temperature observations, but within about 20 days, the two h_m traces begin to track each other again. Advective heating (cooling) can be seen to result in warmer (colder) observed SSTs that persist until advective cooling (heating) can compensate.

Figure 11 compares the standard simulation with two cases with constant water types throughout the year. A constant Jerlov water type IA (dotted trace) produces much lower SSTs from July through October and deeper mixed-layer depths from September through December. By late summer the SSTs are more than 1°C cooler than in the standard simulation. *Martin* [1985] used constant type II water, and the dashed trace of Figure 1 comes from the corresponding KPP simulation. The specification of type IB water in May and June reduces the SST in the standard run, and this difference persists throughout the summer even though the standard run also uses type II water during this period.

6. COMPARISON OF MODEL PERFORMANCE

In this section, simulations from several one-dimensional upper ocean models of Ocean Storms wind deepening, LOTUS diurnal cycling and annual cycles

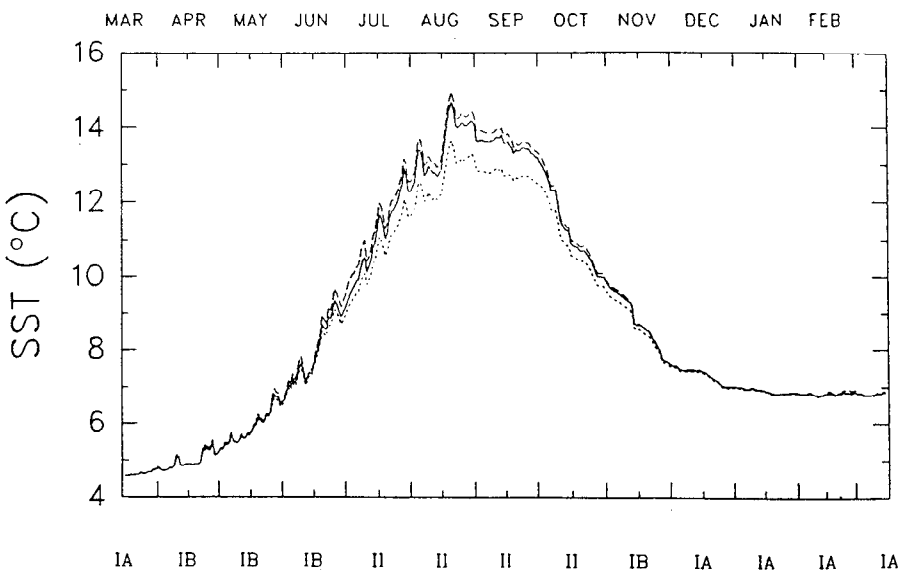

Figure 11. (a) Annual cycle, starting March 15, 1961, of SST from the standard OWS Papa simulation (solid trace), whose specified monthly Jerlov water types are given at the bottom of the figure, and from runs with constant type IA (dotted trace) and type II (dashed trace) water.

at OWS Papa ocean models are intercompared and compared with observations. In each case the KPP is shown to perform as well as or better than the others without any of its parameter values adjusted. Fortunately, simulations from all major classes of models are available in the literature for comparison. However, some of these results were obtained only after their model parameters had been optimally adjusted. There is considerable discussion of the model forcing in Appendix A because any comparison of model results is really a comparison of the model and of the forcing used to drive it. Using identical forcing would not separate the two effects because inaccurate or erroneous forcing could easily cause a poor model to simulate observations better than even a perfect model. Therefore the KPP is forced with our preferred forcing, while other model results are taken as published even though the forcing may have been very different.

A further, related complication, also discussed in Appendix A, is that the upper ocean is rarely found to be one dimensional, so that there is usually an imbalance between the estimated surface fluxes of heat and salt and the corresponding observed changes in upper ocean heat content and salinity. There are different strategies employed to cope with this problem. Perhaps the most common is flux correction, in which the fluxes are adjusted to match the observed changes. Often the imbalance is simply ignored. The most physical treatment is to determine the cause of the imbalance and to add, or subtract, heat, or salt, at the appropriate model depths. However, the cause is not always known.

Ocean Storms

Large and Crawford [1994] have conducted a detailed study of the oceanic response of three models to storm events in the northeast Pacific. The models are a *Mellor and Yamada* [1982] approximation level 2.5 (MY2.5), the bulk mixed-layer model of *Price et al.* [1986] (often referred to as PWP), and the KPP model. The wind forcing is dominant over these very short timescales, so heat and salt imbalances can be ignored. Forcing, initial conditions, and comparative observations both of the dynamic responses (changes in mixed-layer inertial kinetic energy and Lagrangian particle displacements in the mixed layer), and of the thermodynamic responses (mixed-layer temperature and potential energy changes due to vertical mixing) were all derived from observations taken during fall and winter 1987 during the Ocean Storms experiment [*D'Asaro*, 1985a]. The results can be summarized as follows. The thermodynamic responses of KPP are significantly stronger than those of either PWP or MY2.5 because mixing penetrates deeper into the thermocline in response to an inertially rotating wind stress. The deep mixing in KPP and observations, as inferred from thermocline heating, are very similar. Again the failure of local second-order closure schemes to mix sufficiently deep results in MY2.5 producing smaller than observed thermodynamic responses. Mixing in PWP penetrates deeper than in MY2.5, but still considerably less than in the observations. Mixing into the thermocline has much less of an effect on the dynamical responses, which are therefore similar from all three models. These responses compare favorably with the observations.

The model of *Kantha and Clayson* [1994] (KC) is a modification of the *Galperin et al.* [1988] version of a *Mellor and Yamada* [1982] second-moment closure model. Additional mixing in the stratified region below the mixed layer is based on the parameterizations of section 4 and is intended to remedy the inadequate mixing of the *Mellor and Yamada* [1982] models. This mixing has a significant impact. Using the same forcing and initial conditions as Large and Crawford for one particular Ocean Storms event, the mixing extends about 5 m deeper and is more vigorous in the upper thermocline in KC than in a companion MY2.5 simulation. The resulting mixed-layer cooling is about 0.4°C greater [*Kantha and Clayson*, 1994]. The observed thermocline mixing and KPP mixing extend even deeper by about 10 m. The observed SST cooling of 1.12°C is about 0.12°C more than that of KC and 0.18°C less than that of KPP. However, the one-dimensional heat budget for this event did not close. There was insufficient mixed-layer cooling to balance the observed thermocline heating, making comparisons of SST changes inconclusive.

LOTUS

Diurnal cycling at LOTUS over the 7 days of Figure 8 has also been simulated with other models. *Stramma et al.* [1986] use the PWP model and ignore heat imbalances (Appendix A). *Gaspar et al.* [1990] develop a second-moment model (GGL), which is akin to a MY2.5 model except that there are two independent length scales and these are diagnostic rather than prognostic. These length scales are defined by *Bourgeault and Andre* [1986] as the distances upward or downward that a fluid particle would travel in converting all of its initial turbulent kinetic energy into potential energy. Gaspar et al. flux correct for about 85% of the heat imbalance not accounted for by their estimates of advection (Appendix A). However, there is an inconsistency because the advective heat flux is not added to the water column. Following *Stramma et al.* [1986], heat imbalances are ignored by *Kantha and Clayson* [1994] and in the KPP simulations (Figure 8). Over this 2-week LOTUS timescale, salt imbalances are not important and are ignored in all four simulations.

Some critical quantities that simulations of diurnal cycling at LOTUS seek to reproduce are the daily maximum surface temperature, T_{max} (0.6 m), the daily minimum surface temperature, T_{min} (0.6 m), and the difference between these surface temperatures and a

TABLE 4. Maximum Daily Near-Surface Temperature Minus the Temperature at 15-m Depth T_{max} (0.6 m) − T (15 m) for 6 Days of Large Diurnal Cycles at LOTUS in July 1982

		Model			
Day	*Data*	*KPP*	*PWP*	*GGL*	*KC*
194	2.52	2.67	1.80	1.81	2.07
195	2.83	2.79	2.18	2.08	2.64
196	3.91	3.95	4.06	3.19	3.65
197	4.06	4.25	4.92	3.42	4.03
198	3.90	4.58	4.78	3.63	4.38
199	3.51	3.93	4.97	3.28	4.20
Average	3.45	3.69	3.79	2.90	3.50
rms		0.34	0.88	0.59	0.41

Shown are observed data and the values from four model simulations, and their rms differences from observations.

deeper reference temperature at, say, 15 m, T (15 m). Two useful quantities for comparison then are T_{max} (0.6 m) − T (15 m), and the amplitude of the diurnal cycle, T_{max} (0.6 m) − T_{min} (0.6 m). Values of these quantities are given in Table 4 and Table 5, respectively, for the 6 days of Figure 8 with large diurnal signals. *Stramma et al.* [1986] do not give the absolute temperatures from the PWP model, so it is assumed that their T (15 m) is constant at the observed average value of 24.6°C. Also shown for each measure are the averages over the 6 days and the root-mean-square (rms) difference between the observed and each of the four models.

Table 4 shows the T_{max} (0.6 m) − T (15 m) from KPP compared with observations is always within 0.7°C, agrees on average to within 0.25°C, and has a small rms difference of only 0.34°C. The agreement is particularly good over the first four diurnal cycles. In contrast, this quantity from GGL is more than 0.6°C smaller than observed on each of the first 4 days and on average is 0.55°C smaller. The T_{max} (0.6 m) − T (15 m) values from KC tend to be smaller than observed early in the simulation and larger later, such that there is good agreement on average, but a 0.41°C rms difference. The PWP model does not reproduce this quantity as well as the others, with a rms difference of 0.88°C and a maximum difference of 1.46°C on day 199. The large PWP differences appear to be due to lack of vertical mixing. The consequences of this deficiency are that heat remains in the upper few meters of the model, causing the surface temperature to become too warm and the thermal stratification between the surface and 5 m to be much greater than observed.

Table 5 shows that all models simulate the average observed diurnal amplitudes to within 0.2°C. However, PWP differs the most on average and gives the largest rms difference. By both the above measures the PWP simulation is the least successful. This result is somewhat surprising because this model was first developed to study diurnal cycling in the Pacific [*Price et al.*, 1986].

Over the comparison period of Tables 4 and 5, the heat flux into the GGL model appears to be too small by at least 30 to 46 W m^{-2} (Appendix A). Such a larger heat flux would heat the upper 5 m by nearly 0.5°C over these days. It would also stabilize the water column, inhibiting vertical mixing and producing even more warming, depending on where the advection was put into the water column. Thus without the flux corrections the GGL surface temperatures would have

TABLE 5. Amplitude of Diurnal Cycle, [T_{max} (0.6 m) − T_{min} (0.6 m)], for 6 Days at LOTUS in July 1982

		Model			
Day	*Data*	*KPP*	*PWP*	*GGL*	*KC*
194	1.26	1.24	1.01	1.16	1.26
195	1.60	1.24	1.01	1.25	1.41
196	2.43	2.08	2.31	2.07	1.86
197	1.78	1.91	1.92	1.80	1.70
198	1.74	1.95	1.59	1.73	1.66
199	1.14	1.03	1.06	1.23	1.22
Average	1.66	1.57	1.48	1.54	1.52
rms		0.23	0.28	0.21	0.25

Shown are observed data and the values from four model simulations, and their rms differences from observations.

TABLE 6. Compilation of Results From OWS Papa Simulations of 1961, 1969, and 1973

Model	Q_A, W m^{-2}	Mean Model-Data SST Difference, °C									
		April	May	June	July	Aug.	Sept.	Oct.	Nov.	Dec.	April–Aug.
						1961					
MY2	8	0.0	0.2	0.6	0.8	1.5	1.9	0.0	0.2	0.8	0.62
MY2.5	8	0.0	0.2	0.7	0.9	1.6	2.2	0.3	0.5	0.9	0.68
N75	8	−0.2	−0.5	−1.2	−2.0	−2.4	−2.7	−3.0	−2.0	−0.8	−1.26
G77	8	0.0	−0.1	−0.3	−0.2	−0.3	−1.1	−1.8	−1.0	−0.1	−0.18
KC	8	−0.1	−0.14	−0.37	−0.76	−0.73	−0.76	−0.92	0.67	1.11	−0.42
KPP	29	−0.23	−0.16	−0.27	−0.26	−0.33	0.03	−0.32	0.07	0.65	−0.25
						1969					
NK77	12	−0.04	0.12	0.77	0.52	0.48	0.25	−0.33	−0.49	−0.34	0.37
G77	12	−0.06	0.02	0.56	0.37	0.39	0.48	0.05	−0.02	−0.02	0.26
CMO	12	−0.06	0.03	0.50	0.28	0.25	0.33	−0.05	−0.07	−0.09	0.20
GGL	12	−0.04	−0.07	0.02	−0.06	0.22	−0.14	−0.23	0.15	0.24	0.01
KPP	29	0.15	0.28	0.38	0.06	0.17	0.44*	0.43*	0.46*	0.22*	0.21
						1973					
PWP	0	−0.48	−0.33	−0.61	−1.10	−1.08	−0.73	−1.05	−0.47	−0.59	−0.72
KPP	11	−0.34	−0.15	0.04	0.22	0.01	0.02*	−0.66*	−0.55*	−0.86*	−0.04

Shown are monthly mean SST differences, model minus observed, and the April through August average. Heat fluxes averaged over the calendar year are also shown.

*Months when climatological horizontal advection was applied to the KPP simulations.

become much too high and would be indicative of too little entrainment mixing. In the LOTUS case the additional KC local mixing appears to have overcome this problem without flux correction.

OWS Papa

Simulations of an annual cycle at OWS Papa provide a more stringent test of model and forcing because of the longer integration time and the great variety of surface forcing conditions. As was discussed in section 5, KPP simulations always start at the beginning of an ocean year in mid-March. By September we suspect that horizontal advection may become systematic and large. Thus the most meaningful comparisons are for the months April through August of the first year.

One useful measure of model success is the annual cycle of monthly mean SST difference, ΔSST_m, model minus observed. The turbulent heat flux at the ocean's surface, Q_t, varies with SST approximately according to

$$\frac{\partial Q_t}{\partial SST} = (5 + 4U_{10}) \frac{W}{m^2 K} \tag{37}$$

where the first term in the right-hand side comes from the longwave radiation and the second is due to the combined effects of the latent and sensible heat fluxes, with U_{10} the 10 m wind speed in meters per second. The mean wind speed at OWS Papa is about 10 m s^{-1}, so an SST error of even 0.5°C can lead to serious flux errors of more than 20 W m^{-2}. A necessary, but insufficient, condition for model success therefore might be ΔSST_m values less than 0.5°C every month. Even differences this small are a significant fraction (14%) of the amplitude of the mean annual cycle of SST (about 3.7°C) and 50% or more of the standard deviation of a monthly mean temperature over 20 years.

Kraus and Turner [1967] bulk mixed-layer models have often been applied at OWS PAPA. *Martin* [1985], for example, runs both the *Niiler* [1975] (N75) and the *Garwood* [1977] (G77) models at OWS Papa for the calendar year 1961, in addition to *Mellor and Yamada* [1982] approximation levels 2 (MY2) and 2.5 (MY2.5). This year has also been simulated by the KC model [*Kantha and Clayson*, 1994]. *Gaspar* [1988] employs several Kraus-Turner type models at OWS Papa over the 4 years 1969–1973. The models include G77, *Niiler and Kraus* [1977] (NK77), and his own attempt to improve on these, which he refers to as the CMO model. *Gaspar et al.* [1990] also report on their OWS Papa simulations of 1969 and 1970 with GGL. The PWP model too has recently been run at OWS Papa, but over the years 1973–1979 [*Archer et al.*, 1993]. The forcing used in these simulations is discussed in Appendix A.

The first four ΔSST_m entries of Table 6 are from *Martin*'s [1985] simulations of 1961. Both second-order closure models (MY2 and MY2.5) display a warm bias, with $\Delta SST_m > 0.5$°C from June through September. The two models' August and September mean SSTs range from 15.3° to 15.7°C. For comparison, the maximum monthly mean SST observed between 1959 and 1981 was only 14.5°C (August 1979). In September, ΔSST_m is about twice the climatological standard deviation of monthly SST (1°C). Forcing these two

models with our larger heat fluxes would likely degrade their performance by the ΔSST_m measure because of both the increased heat and the greater vertical stability. This result is consistent with the pattern of insufficient vertical exchange in models of this class. The additional KC mixing may be overcompensating, since the ΔSST_m values are consistently too low until December.

The bulk mixed-layer models behave very differently. As was noted by *Martin* [1985], the N75 mixed layer tends to be far too deep, resulting in much too cold surface temperatures. It deepens to the model bottom at 200 m in March and again in December. According to *Martin* [1985], G77 gives good results at OWS Papa (Table 6) with appropriate tuning but tends to deepen too rapidly in the fall. Forcing with greater heat fluxes would certainly improve the N75 simulation by warming the surface and stabilizing the water column, but it is likely that there would still be excessive deepening, especially in March. Use of such fluxes could seriously degrade the G77 results. *Martin* [1985] shows a spike in the August SST of 16°C from G77 compared with an observed value of less than 15°C. More heating would make this peak much higher and probably increase the summer values of ΔSST_m to more than 0.5°C. However, the fall deepening would likely be reduced.

Gaspar [1988] performs 4-year simulations at OWS Papa starting January 1, 1969. The imbalance in his heat budget is only 4 W m^{-2} over the 4 years (Appendix A) and is ignored. He first runs the NK77, *Resnyanskiy* [1975], and *Wells* [1979] models. He concludes that all these bulk models systematically overestimate SST in summer by about the same amount, despite empirical calibration or tuning. Table 6 shows only the NK77 results because of the similarity between the results. In an attempt to improve this situation, *Gaspar* [1988] then develops a new model, CMO. He runs this model and G77 over the same 4 years. He finds that the G77 results (Table 6) are similar to those of *Resnyanskiy* [1975] and of *Wells* [1979] and that although CMO succeeds in reducing ΔSST_m below 0.5°C, there is still a tendency for SST estimates to be too high in summer and too low in fall (Table 6). Dissatisfaction with these results presumably led to the development of GGL, which *Gaspar et al.* [1990] run only over 1969 and 1970. Now the magnitudes of the ΔSST_m values are very small, especially in 1969 (Table 6). The summer bias in all the bulk models (NK77, G77, and CMO) would increase significantly if they were forced with our larger surface heating. It is unclear what the effect on the second-order closure of GGL would be, but it is likely that all the 1969 ΔSST_m values would become positive.

A companion 4-year KPP simulation starts in March 1969. Here, for the first time, climatological advection of heat and salt is used to balance the heat and salt budgets. As is described in Appendix A, most of the heat advection occurs between September and February, and with this cooling, ΔSST_m remains less than 0.5°C through December (Table 6). Before September the maximum ΔSST_m is only 0.38°C in June.

The *Archer et al.* [1993] PWP simulations at OWS Papa cover the 6 years 1973–1978. Climatological advection was again applied each winter of a companion, 6-year KPP run. The 1973 results (Table 6) show that PWP seriously underestimates the monthly mean SST; a systematic bias that persists throughout the 6 years. Our estimates over the 20 years 1961–1980 indicate that Q_A was smallest in 1973 and 1974, at 11 and 12 W m^{-2}, respectively. The observed temperatures suggest anomalous thermocline heating in the summer and usual advective cooling in the fall, so that the KPP modeled SSTs are too cold from October to December 1973. It appears to take two winter advective seasons to overcome the anomaly, so that the KPP model reproduces observed SSTs from March 1976 through 1978 with little bias.

We now address the question of how GGL produces such a good SST simulation when forced with what we believe is too little surface heating. The answer is that, as is usual with such second-moment models, there is insufficient mixing into the thermocline, which allows the SST to become high enough by keeping the entire thermocline too cold. Monthly mean observed temperature profiles (dotted traces) from near OWS Papa are shown in Figure 12 for June through November 1969. The time-depth section from *Gaspar et al.* [1990] is used to give the average depth of GGL isotherms from 5° to 11°C (solid circles). In the seasonal thermocline, GGL temperatures are always colder than observed ones, usually by more than 1°C. The August comparison is particularly poor, with a temperature difference of 3°C at 35 m. Vertical mixing of this cold thermocline water up into the mixed layer would lower the model SST, and hence ΔSST_m, by at least 2°C. The July and September values would decrease by at least 1°C. The decrease would be less in the other months because of the deeper mixed layer, but still significant. Thus proper vertical mixing would seriously degrade the GGL simulation throughout most of the year. Forcing with our larger surface heating would increase the surface temperatures and inhibit the vertical mixing even more.

Monthly mean KPP temperature profiles from 1969 are also shown in Figure 12. For all 6 months, KPP thermocline temperatures are closer to observations than are GGL modeled temperatures. The poorest agreement is again in August, which may be due to warm water advected into the thermocline, but the KPP temperature deficit is only about half of that found for GGL. Another positive feature of the KPP simulation is that differences with observations are not systematic. July and October mean profiles are not significantly different, and modeled thermocline tem-

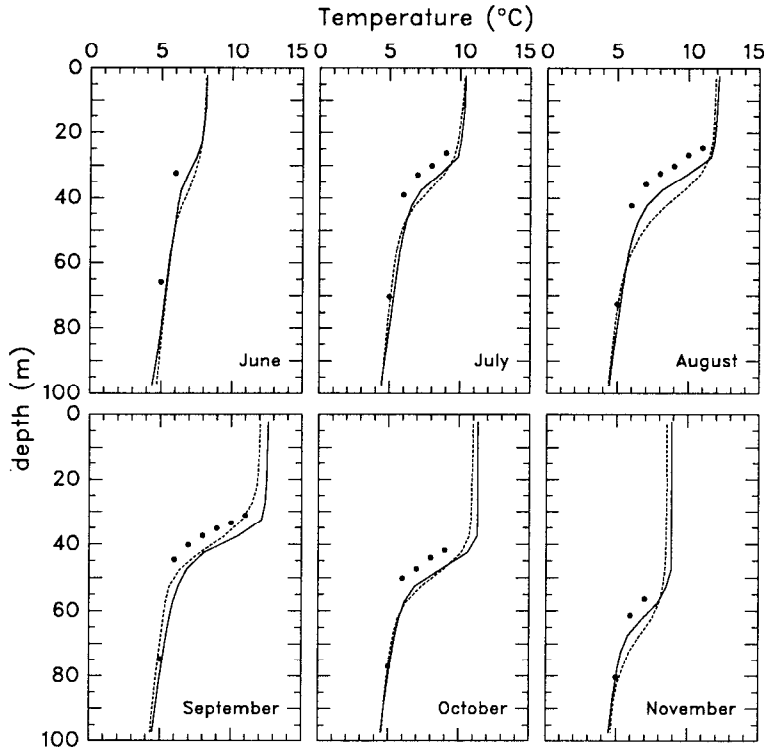

Figure 12. Monthly mean profiles for six months of 1969 at OWS Papa. Shown are observed (dotted trace) and simulated temperatures from GGL (solid circles) as reported by *Gaspar et al.* [1990] and from KPP (solid trace).

peratures are warmer in September but colder in August and November.

Figure 13 (bottom) compares observed (dashed trace) and modeled (solid trace) changes in heat content over the 4 years 1969–1972. Again, strong advective activity on timescales of 1 week to 1 month is evident in the observations. Corresponding observed temperature changes (top plots, dashed traces) are coherent throughout the water column. With climatological advection (Appendix A) the average heat con-

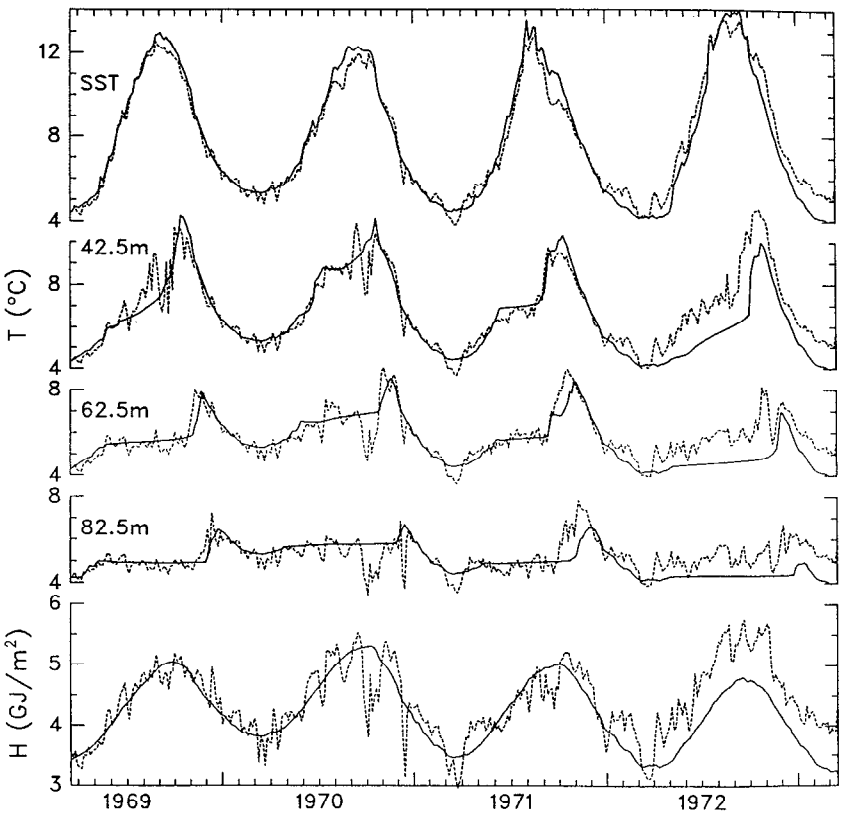

Figure 13. Four-year time series (top) of temperatures at the surface and at three depths in the seasonal thermocline and (bottom) of heat content above 200 m. Shown are observations (dotted trace) and KPP simulations (solid trace).

tents are in good agreement through the first two winters, suggesting that advection was not unusual. From January through March of 1972, however, the observed heat content fails to decrease in response to the surface cooling, suggesting an absence of the usual advective cooling with perhaps some advective heating, such as was already seen in 1961. April 1972 to March 1973 appears to have been an average year, so throughout this time the observed heat content retains its positive anomaly picked up in the previous winter and remains greater than in the model. It is interesting to note that the 1972 SST simulation is reasonable, but like GGL in 1969, this test is insufficient because the shallow summer mixed layer contains only a small fraction of the warm anomaly. However, the absence of winter cooling is obvious in the thermocline temperature comparisons at 42.5, 62.5, and 82.5 m (Figure 13).

From March 1969 to January 1972 the modeled and observed temperatures are in very good agreement throughout the water column, with the exception of some anomalous, relative to the imposed climatological advection, events (Figure 13). There do not appear to be any systematic biases. Modeled temperatures at a given depth are sometimes warmer and sometimes cooler than those observed. The annual cycle is faithfully represented. There are increasing temperatures in spring, a leveling off of the temperature increases as a particular depth is capped by the seasonal mixed layer, then a heating in the fall as heat stored in the mixed layer is exchanged with colder thermocline water. As one looks deeper, the spring temperature rise stops earlier, the leveling persists longer, and the fall heating and temperature maximum occur later. Such an annual cycle was described by *Tabata* [1965] for earlier years at OWS Papa.

7. DISCUSSION

The KPP vertical mixing parameterizations of both the OBL and the oceanic interior were developed for use in global ocean models, with integrations lasting a decade and longer. A particularly encouraging result of the present study is that the KPP model has been successful over timescales spanning about 4 orders of magnitude, from hours to years. Observations at OWS Papa are well simulated at all depths from year to year provided that the fall advection is accounted for. It very well may be that this success depends on the capability of the model to handle events of order only a day in duration. The KPP model has been shown to simulate many such events very well, including convective boundary layer deepening, diurnal cycling, and storm forcing.

One key to the success of KPP is that it predicts an ocean boundary layer depth, with the mixed-layer depth a diagnostic quantity that can depend on definition and the property of interest. This feature allows for finite diffusivities throughout the water column and hence vertical structure within what might be termed the mixed layer. Most importantly, both the convective and the wind-driven boundary layers can penetrate well into the stratified region below a mixed layer. Even though such events may be short-lived, the resulting vertical fluxes can be large enough to have a significant impact on much longer timescales. Only with such penetration can the large diffusivities that represent the efficient mixing of boundary layer eddies act upon the large property gradients typically found below a mixed layer.

The KPP scheme has several other attributes that make it attractive for a variety of applications, including large-scale climate modeling. It is relatively insensitive to vertical resolution and may perform well in low-resolution configurations (see also Appendix C). It is readily adaptable to various finite-differencing schemes and vertical coordinates. Most importantly, the results of the present work indicate that if it is given the correct surface forcing and advective transports, it will distribute properties properly in the vertical. A one-dimensional model can do no more. In addition, the parameterization has been formulated to be run off surface fluxes, so it is readily coupled to an atmosphere or sea ice model.

There are several major differences between this ocean boundary layer model and the atmospheric counterparts that it follows [*Troen and Mahrt*, 1986; *Holtslag et al.*, 1990]. First, in the atmospheric models the turbulent shear does not contribute to the boundary layer depth. Instead, enhanced convective entrainment is achieved by giving convective elements (thermals in the atmosphere) a buoyancy excess. Thus the atmospheric version of (21) sets $V_t = 0$ and $B_r = B_0 + C_b\overline{wb}_0$, where the last term parameterizes this excess and C_b is an empirical constant. This form is unattractive in the ocean because neither has C_b been measured, nor has the form of the parameterization been confirmed. Also, the use of the surface buoyancy B_0, rather than a surface layer average, promotes resolution dependency (Figure 1). Global applicability would be questionable because for a fixed excess, β_T would depend on the stratification near h. Also, with $V_t = 0$, Richardson numbers (equation (21)) get very large when the mean shear is small. Besides, turbulence should contribute to the shear. To illustrate the effect, suppose that interior stratification weakens and all other conditions remain steady. In the atmospheric form, the Ri_b decreases and h can get very large. In our oceanic case these tendencies are offset to a degree by smaller values of V_t, so the growth in h is controlled.

The second major difference is that all depths in the OBL can be forced from the interior through the dependence of a_2 and a_3 in (17) on the interior diffusivity and its vertical derivative at h (equation (18)). This

forcing could be very significant in regions such as the equatorial ocean where the Equatorial Undercurrent could lead to shear instability near h. The scheme may be applicable to atmospheric situations, such as when the top of the boundary layer is near a nocturnal jet [*Kim and Mahrt*, 1992] or the subtropical jet. The dimensionless flux profiles (equation (B1)) are also quite different, but situations where these differences would change model results appreciably are probably rare.

It is worthwhile reiterating that any comparison between model results and observations is a test both of model integrity and of the fidelity of the forcing functions, and that comparisons of SST and mixed-layer depth are necessary but insufficient tests of a model's performance. Over most of the period chosen for the LOTUS simulation, for example, the ocean observations show little sign of important advective heating, so following *Stramma et al.* [1986], no flux or advective corrections are applied in the present study. Although this is most likely not the case over the longer period simulated by *Gaspar et al.* [1990], it is not proper to apply a constant correction to the surface fluxes. Instead, an intermittent advective cooling should be injected at depth in the water column when and where the observations indicate. The former procedure tends to reduce the stability of the upper water column, while the latter may enhance stability. Thus it may be preferable not to apply any correction rather than to apply an inappropriate one. At OWS Papa our flux estimates and interpretation of historical data indicate that there is important systematic advective heat in the region during the fall and winter. Other studies assume one-dimensionality and use heat flux estimates that are near zero when averaged over an annual cycle. Thus at both sites our preferred surface heat flux is larger than that used in some other investigations.

The most significant difference compared to other models is that the KPP boundary layer can extend well into the thermocline and produce realistic exchanges of properties between the mixed layer and thermocline. Second-moment models such as MY2.5 and GGL tend to underestimate such mixing. Forcing with a greater surface heat flux would stabilize the water column and worsen this trait. Another difference, especially with bulk mixed-layer models such as PWP, is that the OBL in KPP need not always be well mixed. Mixing at the base of bulk mixed-layer models typically depends on adjustable parameters, so they can be made to represent some situations quite well [*Gaspar*, 1988]. However, it may be difficult or even impossible to find one set of parameter values for such a model that applies in the variety of conditions found over an annual cycle [e.g., *Archer et al.*, 1993] or over the global ocean.

Integrations here and in the other studies discussed in section 6 have been over a relatively short period of time, with temperature the important diagnostic variable. However, in cases when other properties are also important, the model's ability to exchange properties between the mixed layer and deeper stratified waters may become even more important. For example, such ability would seem to be an essential ingredient of any model used to study mixed-layer biogeochemistry. There is often a rich supply of nutrients in the upper thermocline with productivity above in the euphotic zone limited by the supply of these nutrients. There can also be large differences in the concentrations of chemical species between the mixed layer and water below. Also, salt can play an important role in the ocean, especially, but not exclusively, over longer timescales. In such instances the exchange of salt between the mixed layer and deeper pycnocline becomes critical to maintaining the correct stability of the water column and to balancing the surface freshwater flux.

Although the present KPP model has proven successful, there are several areas where the model development should continue. Most urgently required is a scheme that differentiates between the entrainment-driven and surface-driven vertical transports of passive scalars. Because the thermocline is such a large property reservoir, entrainment-driven transport may be much more important in the ocean than in the atmosphere. To achieve this behavior, it will likely be necessary to have a more satisfactory parameterization of the nonlocal transport term. In the traditional parameterization (20), γ_s depends on the surface fluxes, which in the ABL bulk formulae are expressed in terms of near-surface property gradients. However, this term should perhaps depend on property differences over a larger vertical extent, since it accounts for turbulent fluxes resulting from eddies that traverse much or all of the boundary layer.

There are also several aspects of the present model that have not been adequately tested owing to a lack of observations. Within the boundary layer scheme we were unable to show that the restrictions that h be less than both L and h_E (equation (24)) made any appreciable difference to the solutions. These conditions are likely to arise often in a global simulation of many years, so it is important to establish whether or not they are proper and necessary. Proper physics would seem to require much reduced diffusivities at depths $d > L$, where buoyant suppression exceeds mechanical production of turbulent kinetic energy. The restriction $h \leq L$ accomplishes this reduction by making this region part of the interior. However, a similar effect is achieved for $L < d < h$ by the large values of ϕ_x given by (B1) for $\zeta > 1$. Such values very effectively reduce boundary layer diffusivities (Figure 2) to levels more comparable to those of the interior. It was shown (Figure C4) that including solar radiation in the surface buoyancy flux (equation (A3)) did change the diurnal cycling at LOTUS but that the change was too small

for the observations to determine which is preferable. Some form of interior diffusivity ν_x was noted to be necessary. However, it was not determined if the parameterizations of section 4 were appropriate. Of concern for global deep water applications is whether internal wave mixing is best described as a constant (equation (34)) following *Gregg* [1989] or as proportional to N^{-1}, as was suggested by *Gargett and Holloway* [1984]. The latter could be easily implemented because N is already computed for the gradient Richardson number calculation (32). Most of the observations of double diffusion have gone into the parameterizations, and independent observations of both salt fingering and diffusive convection are required to confirm the treatment of section 4.

APPENDIX A: EXTERNAL FORCING

This appendix describes the external forcing used to drive the KPP model. There are the surface fluxes and the bottom boundary conditions at $d = -D$. Expressions are given for the solar irradiance profile and for the radiative contributions both to the stability and to the nonlocal transport. In addition, details of the heat fluxes used to drive various LOTUS and OWS Papa simulations are given, and strategies for dealing with imbalances in the heat and salt budgets are discussed in the context of individual simulations of ocean observations.

Surface forcing that is transferred by turbulent processes is distinguished from nonturbulent forcing, such as radiation. The former includes the zonal and meridional stress components τ_u and τ_v, the net turbulent heat flux Q_t, and the net turbulent freshwater flux F_t. The net solar surface irradiance I_0 is distributed in the water column as one component of the nonturbulent heat flux profile, $Q_n(d)$. Sea ice that forms at depth and rises to the surface (frazil ice) gives rise to the other component of $Q_n(d)$ and to a nonturbulent freshwater flux $F_n(d)$. The heat flux associated with freezing at the surface and accretion of ice crystals onto existing sea ice is incorporated into the net turbulent heat flux. The companion water flux is really a turbulent saltwater flux F_s, with the salinity of sea ice, S_I.

In the ice-free conditions considered in this paper, the surface stress is due solely to the wind, the components of Q_t are the net longwave radiation and the latent and sensible heat fluxes, F_t is the excess of precipitation over evaporation, $Q_n(d)$ is just the solar irradiance profile $I(d)$, and $F_s = F_n(d) = 0$. Sometimes the fluxes are estimated from observed meteorological variables such as wind velocity, SST, air temperature, relative humidity, and cloudiness. In these cases the wind stress, the sensible heat, the latent heat, and hence the evaporation are computed following *Large and Pond* [1982], where the respective neutral, 10-m bulk transfer coefficients are

$$10^3 C_D = \frac{2.70}{U_{10}} + 0.142 + 0.0764 U_{10} \quad \text{(A1a)}$$

$$10^3 C_\theta = 32.7 C_D^{1/2} \quad \text{unstable}$$

$$10^3 C_\theta = 18.0 C_D^{1/2} \quad \text{stable} \quad \text{(A1b)}$$

$$10^3 C_E = 34.6 C_D^{1/2} \quad \text{(A1c)}$$

where U_{10} is the wind speed at 10-m height in meters per second. The C_D formulation is a fit to data averaged over wind speed bins from 1 to more than 25 m s^{-1} (E. E. Vera, unpublished manuscript, 1983), and it makes all the coefficients go to their theoretical infinite values at zero wind speed. The solar radiation is computed assuming an oceanic albedo of 0.06 and the Okta model of *Dobson and Smith* [1988]. This model corrects the clear sky solar radiation (a function of latitude, year day, and local time) for a specified cloud fraction. Net longwave forcing is computed from a conventional parameterization [*Berliand and Berliand*, 1952; *Fung et al.*, 1984], with *Bunker*'s [1976] cloud factor equation and a slightly enhanced emissivity of 1.0 to account for reflected longwave radiation.

The active surface kinematic fluxes are given by

$$\overline{wu}_0 = -\tau_u/\rho_0 \quad \text{(A2a)}$$

$$\overline{wv}_0 = -\tau_v/\rho_0 \quad \text{(A2b)}$$

$$\overline{wt}_0 = -Q_t/(\rho_0 C_{p0}) \quad \text{(A2c)}$$

$$\overline{ws}_0 = F_t S_0/\rho_0(0) + F_s(S_0 - S_I)/\rho_0(S_I) \quad \text{(A2d)}$$

where S_0, ρ_0, and C_{p0} are the salinity, density, and specific heat at constant pressure of the surface seawater, respectively. The density of surface water of salinities 0 and S_I are $\rho_0(0)$ and $\rho_0(S_I)$, respectively. The buoyancy profile $B(d)$ and the surface buoyancy flux $\overline{wb}_0$ and forcing B_f are diagnostic quantities computed as

$$B(d) = g(\alpha T - \beta S) \quad \text{(A3a)}$$

$$\overline{wb}_0 = g(\alpha \overline{wt}_0 - \beta \overline{ws}_0) \quad \text{(A3b)}$$

$$B_R = g[(\alpha I/\rho C_p)_0 - (\alpha I/\rho C_p)_{h_b}] \quad \text{(A3c)}$$

$$B_f = -\overline{wb}_0 + B_R \quad \text{(A3d)}$$

where g is gravitational acceleration, α and β are the thermodynamic expansion coefficients evaluated at local values of T and S, and the subscripts 0 and h_B specify evaluation at the surface and at $d = h_B$, respectively. It is not clear what the radiative contri-

bution B_R to the surface buoyancy forcing B_f and hence the stability, by L (equation (2)), should be. This term is not considered by *Troen and Mahrt* [1986] because of the negligible solar absorption in the ABL. Setting $h_B = 0.0$ in (A3) assumes no contribution. At most, only radiation absorbed in the OBL has the potential to affect the turbulence, so h_B can be at most equal to h. The buoyancy effects of frazil ice formation could be treated in a similar fashion.

Similarly, the radiative contribution to the surface heat flux that is used to parameterize the nonlocal heat flux, γ_θ (20), is unknown. Again it can be expressed as

$$-\overline{w\theta}_R = [(I/\rho C_p)_0 - (I/\rho C_p)_{h_\gamma}] \qquad \text{(A4)}$$

where the depth of evaluation, h_γ, is between the surface and $d = h$.

The distribution of solar irradiance in the water column is modeled by the general form

$$I(d) = I_0 \sum_{i=1}^{NI} r_i \exp\left(-\frac{d}{\mu_i}\right) \qquad \text{(A5)}$$

in which the solar spectrum is divided into a number NI of wavelength bands, each containing a fraction r_i of the total radiation. The reciprocals of the band absorption coefficients are the μ_i. A one-band formulation does not do well throughout the column because long infrared and red wavelengths are absorbed much closer to the surface than are some shorter wavelengths. *Paulson and Simpson* [1977] find that a two-band model, $NI = 2$, should be adequate for most physical models. They give empirical values of r_1, r_2, μ_1, and μ_2 for each of the different *Jerlov* [1976] water types.

The model is usually configured over a depth D that is less than the full ocean depth, and fluxes across the bottom at $z = -D$ are then governed by (26), because of the depth restriction, $h < D$. Whenever a property gradient is nonzero, there is a downgradient property flux because there is always a positive diffusivity, $\nu_x(-D) \geq \nu_x^w$ (equation (25)). Integration of such fluxes over time gives the net gain from or loss to the deep ocean. Conceptually, the velocity bottom boundary conditions are the geostrophic reference velocities at $d = D$. In three-dimensional applications the profile of geostrophic velocity would be computed from the horizontal pressure gradient derived from the T and S distributions. It would then be added to the surface-forced velocities to give the total velocity used, for example, in (21) and (27). The horizontal divergence of this velocity together with continuity gives the profile of vertical velocity.

LOTUS Heat Fluxes

Evaluation of the relative performance of the models (section 6) is complicated by the differences in the surface heat fluxes used and by the different ways of dealing with heat and salt imbalances.

At the LOTUS site, near-surface wind velocity, air temperature, and solar insolation were measured from a surface buoy. There are no reliable cloud and humidity observations. Therefore, following *Stramma et al.* [1986] a constant value of 75% relative humidity is assumed in computing the evaporative and latent heat fluxes, and the cloud fraction is estimated by comparing the observed insolation with calculated clear sky solar radiation. The latter operation is not too critical, because clear sky conditions prevailed over much of the period of interest here. Precipitation therefore is assumed to be always zero. *Stramma et al.* [1986] found that there model simulation was quite sensitive to the length scale μ_1 used for vertical absorption of long wavelength solar radiation (equation A5)). To be consistent, we use the same values as *Stramma et al.* [1986], namely $NI = 2$, $r_1 = 0.58$, $r_2 = 0.42$, $\mu_1 = 0.35$ m, and $\mu_2 = 23$ m for Jerlov water type I [*Paulson and Simpson*, 1977].

Gaspar et al. [1990] argue that over the 2-week LOTUS period of 1982 (days 193–207) the *Stramma et al.* [1986] surface heat flux are on average 86 W m^{-2} larger than the observed rate of change in ocean heat content. Furthermore, they estimate oceanic heat advection to account for only about 15 W m^{-2}, but this advection is ignored in their simulation. They ascribe the remainder of the imbalance to error in the nonsolar heat flux, from which they remove (flux correct) a bias of 71 W m^{-2}. However, the heat budget imbalance through day 199 is clearly much less; at most 40 W m^{-2} [*Gaspar et al.*, 1990, Figure 7]. Therefore over the comparison period of Tables 4 and 5, the heat flux into the GGL model is too small by at least 31 W m^{-2} and by 46 W m^{-2} if the advection was really present. *Stramma et al.* [1986] note that their heat budget is often in balance between days 195 and 199 and that the observed 50-m temperature shows no evidence of advection. Therefore they neither flux correct nor include any advection.

OWS Papa Heat Fluxes

Our OWS Papa surface forcing is derived from standard 3-hourly meteorological observations except for precipitation, for which a mean annual cycle fit to the 1956–1961 observations of *Tabata* [1965] is used every year:

$$P(t_d) = \left\{23.2 + 9.1 \cdot \cos\left[2\pi\left(\frac{t_d}{365.25} - 0.88\right)\right]\right\} \text{ mg m}^{-2}\text{ s}^{-1}$$

where t_d is the year day. The meteorological data, including cloud fraction, were interpolated to each 1-hour model time step; then surface fluxes were com-

puted as was described above. This procedure gives a 20-year average (1961–1980) net heat input of 24 W m^{-2} and net freshwater gain of 9.3 mg m^{-2} s^{-1}. These compare with the 1956–1961 mean values of 38 W m^{-2} and 7.6 mg m^{-2} s^{-1} computed by *Tabata* [1965] and the 32 W m^{-2} average heat flux from 1959 to 1975 determined by *Smith and Dobson* [1984].

Over many years the net surface heating and freshening appear to be balanced by advective processes. *Tabata* [1965] finds that an average upward vertical velocity due to surface Ekman divergence and deep geostrophic convergence could balance the salt budget, but that this would cool the upper ocean only by about 2 W m^{-2}. *Gill and Niiler* [1973] argue that there is negligible horizontal advection due to mean currents and mean temperature gradients, due to mean currents and seasonal gradients, and due to seasonal currents and mean gradients. Vertical diffusion of heat through the pycnocline cools the upper ocean by less than 1 W m^{-2} because the temperature gradients are so small, with salinity gradients primarily responsible for the deep density gradient. If the excess heating over observed changes in ocean heat content occurred uniformly throughout the year, then perhaps it could be ascribed to errors in the surface flux estimates. However, *Tabata* [1965] shows that the imbalance is concentrated in the fall and winter, when it becomes more than 80 W m^{-2}, and hence much more than should be due to flux errors. Consistent with these results is the suggestion of *Large et al.* [1986] that the heat imbalance is balanced chiefly by seasonal flows acting on seasonal thermocline temperature gradients in the fall and winter.

The year 1961 was chosen for the standard KPP simulation at OWS Papa (section 5) in order to overlap with the period examined by *Martin* [1985]. Martin computes an annual mean surface heat flux, $Q_A(1961)$, of 8 W m^{-2}, and his fluxes are used by *Kantha and Clayson* [1994]. Using the same meteorological data, we get 29 W m^{-2} for the calendar year. The difference is equally partitioned between the longwave radiation and the combined latent and sensible heat fluxes. The former must be due to different cloud factors for the downwelling component because the SST, cloud fraction, and clear-sky formula appear to be identical. The latter is due mainly to very different bulk transfer coefficients. *Martin* [1985] uses 0.00149 at OWS Papa and 0.00122 at OWS November for both C_θ and C_E in (A1). These values were chosen as a compromise between balancing the annual heat budget and matching observed seasonal changes in heat content. The KPP model is run without such tuning, and the coefficients (A1) are about 0.0012. The heat flux difference of about 20 W m^{-2} is sufficient to heat a 10-m water column by about 1.3°C per month.

Gaspar [1988] and *Gaspar et al.* [1990] always use the OWS Papa surface forcing produced by *Tricot* [1985]. The net heat flux over the 4 years 1969–1972 is only 4 W m^{-2}, so heat imbalances are ignored. Our average over these years is 21 W m^{-2}. The solar radiation differs by only 3 W m^{-2}, so the difference is due mostly to the nonsolar flux components. The largest Q_A from Tricot is 12 W m^{-2} in 1969. This value is still significantly less than our $Q_A(1969)$ estimate of 29 W m^{-2}, which is only coincidently the same as our $Q_A(1961)$. *Gaspar* [1988] claims that the Tricot values are corroborated by observed changes in heat content. We disagree because his Figure 1 clearly shows the heat content rising by more than the Tricot heat flux would predict during all four heating seasons and falling by more during all four cooling seasons. These features are consistent with there being a greater heat flux throughout the year and advective cooling during the fall and winter. The *Archer et al.* [1993] forcing has no net annual heat flux.

To integrate any model over a year or more, it is necessary to balance any excess surface heat or fresh water with ocean transports. The latter is accomplished in KPP simulations at OWS Papa in accord with the observational evidence presented above. There is a steady vertical advection of salt through the model bottom corresponding to a removal of 10 mg m^{-2} s^{-1} of fresh water. This process is modeled by a continual salinity increase in all model layers in the halocline below about 120 m where there are salinity gradients for a vertical velocity to act on to give an advective flux of salt. There is a companion advection of cold water, but the associated cooling is only 2 W m^{-2}. Small diffusive heat and salt fluxes across the bottom are computed by the model. The remainder of the excess surface heat flux is balanced in some KPP integrations by horizontal advection that starts in September of each year, peaks in December, and ends in February of the following year. Only model layers above the halocline and below the mixed layer are cooled. This cooling could be prescribed each year to make the following March temperature profile nearly match observations, with its interannual variability accounting for year-to-year changes in ocean advection. Given March initial conditions, the KPP model has been shown to simulate the next heating season very well. However, for present purposes we choose to keep the fall and winter advective cooling the same each year at an annual equivalent of 21.5 W m^{-2} to balance the 20-year climatological heat budget. However, these advections are applied only to the OWS Papa simulations from 1969 through 1973 in section 6.

APPENDIX B: THE DIMENSIONLESS FLUX PROFILES

Calculation of the turbulent velocity scales (equation (16)) requires expressions for the dimensionless flux profiles. Over the whole range of ζ, acceptable fits to the available data are plotted in Figure B1. The analytic expressions of these fits are:

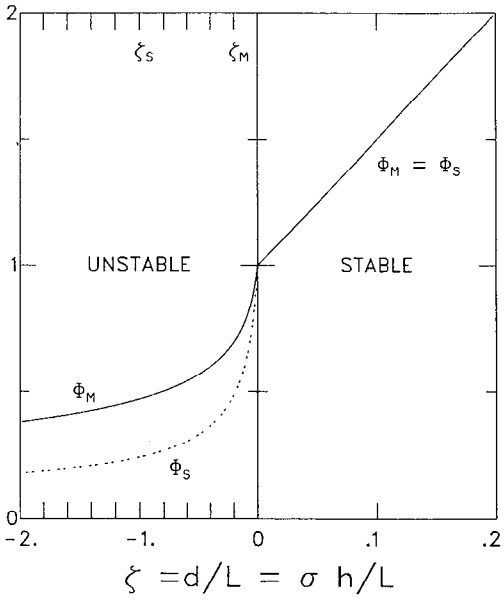

Figure B1. Plots of the nondimensional flux profiles for momentum, ϕ_m, and for scalars, ϕ_s, as functions of the stability parameter ζ. These functions become $-1/3$ power laws for values of ζ more negative than ζ_m and ζ_s, respectively.

$$\phi_m = \phi_s = 1 + 5\zeta \qquad 0 \le \zeta \qquad \text{(B1a)}$$

$$\phi_m = (1 - 16\zeta)^{-1/4} \qquad \zeta_m \le \zeta < 0 \qquad \text{(B1b)}$$

$$\phi_m = (a_m - c_m\zeta)^{-1/3} \qquad \zeta < \zeta_m \qquad \text{(B1c)}$$

$$\phi_s = (1 - 16\zeta)^{-1/2} \qquad \zeta_s \le \zeta < 0 \qquad \text{(B1d)}$$

$$\phi_s = (a_s - c_s\zeta)^{-1/3} \qquad \zeta < \zeta_s \qquad \text{(B1e)}$$

where the subscript s refers to all scalars. The constants in (B1) are prescribed as follows:

$$\begin{array}{lll} \zeta_s = -1.0 & c_s = 98.96 & a_s = -28.86 \\ \zeta_m = -0.20 & c_m = 8.38 & a_m = 1.26 \end{array} \qquad \text{(B2)}$$

where the a_x and c_x are chosen so that both ϕ_x and its first derivative are continuous across $\zeta = \zeta_m$ and ζ_s (Figure B1). This matching also ensures continuity of w_x and its first derivative. In stabilizing forcing nearly all measurements have been for $0 < \zeta < 1$, and there is general agreement on the linear form of (B1), though the proportionality constant varies and sometimes differs for ϕ_s and ϕ_m. The value of 5, used in (B1) and by *Troen and Mahrt* [1986] for both, is common practice [*Panofsky and Dutton*, 1984]. The restriction $h \le L$ precludes ζ ever exceeding 1 in the boundary layer. In unstable conditions near neutral, ϕ_m and ϕ_s are the most common Businger-Dyer forms [*Panofsky and Dutton*, 1984]. These forms match the stable functions at $\zeta = 0$ and are good fits to the available data [*Högström*, 1988] for $\zeta_m \le \zeta < 0$ and $\zeta_s \le \zeta < 0$, respectively.

In more unstable conditions there are no observations of ϕ_x, but the data of *Carl et al.* [1973] suggest the $-1/3$ dependency in (B1) and (14) for ϕ_m. This dependency and a similar $-1/3$ dependency for ϕ_s is also required in order to satisfy the theoretical result of w_x proportional to w^* (equation (6)) in the convective limit, as given in (15). The near-neutral Businger-Dyer forms in (B1) do not lead to this result. In the *Troen and Mahrt* [1986] formulation, only ϕ_m has a $-1/3$ power law dependency at large negative ζ.

The ratio of momentum to scalar diffusivity defines the turbulent Prandtl number, Pr, which from (10) and (13) becomes,

$$Pr = K_m/K_s = w_m/w_s = \phi_s/\phi_m \qquad \text{(B3)}$$

Since there is no physical reason to expect the neutral boundary layer to diffuse momentum differently than scalars, the near-neutral functions (B1) are equal at $\zeta = 0$ (Figure B1), such that $Pr = 1$. The functions used by *Troen and Mahrt* [1986] give $Pr(\zeta = 0) = 0.75$ in accord with some observations [*Businger et al.*, 1971]. Beyond the surface layer, w_x is constant in the convective limit, and (15) gives $w_m = 0.28w^*$ and $w_s = 0.63w^*$ and hence a finite $Pr \to (c_m/c_s)^{1/3} = 0.44$. This value is just the limit of the ratio of the two curves in Figure B1 as ζ becomes increasingly negative. Since this figure shows $\phi_m > \phi_s$ for all $\zeta < 0$, convection always mixes scalars, including buoyancy, more efficiently than momentum.

APPENDIX C: KPP SENSITIVITY EXPERIMENTS

This appendix explores some sensitivities of the KPP simulations in addition to those presented in section 5. First, finite resolution is shown to produce biases and oscillations in the model's boundary layer depth, which are ameliorated numerically (Appendix D). With these numerics the overall effect of entrainment is shown to be well reproduced in a low-resolution convective simulation. Next, the sensitivity of the stably forced LOTUS simulation is investigated. These results are used to establish that the treatment of solar radiation, through our values of h_B and h_γ, is reasonable. Finally, the sensitivity of the annual cycle at OWS Papa is shown to be relatively insensitive to an order of magnitude change in vertical resolution.

Finite Resolution

Any practical resolution of the upper ocean will not always resolve the sharp gradients that occur near the bottom of the boundary layer. The computational problems that result are illustrated by a strongly wind-forced case. Consider the idealized seasonal thermocline shown in Figure C1. The continuous buoyancy and velocity profiles (solid lines) are constant down to a depth $h_m = 17$ m, below which the former has a

constant gradient equivalent to a buoyancy frequency of $N = 0.01\ s^{-1}$ and the latter decreases to zero at $d = 50$ m. The continuous bulk Richardson number profile defined by (21), with $u^* = 0.01\ m\ s^{-1}$ and $\zeta = 0$, is critical at a depth $h_c > h_m$. The discrete buoyancy and velocity profiles (triangles) are formed by averaging over 5-m-thick layers, and these differ from the continuous profiles only in the $n = 4$ layer, where there is nonlinearity. Although these differences appear to be small, they create large differences in the Ri_b computed at the fourth layer. Linear interpolation of the discrete Richardson number profile gives a boundary layer depth h_d that is systematically less than h_c. One problem immediately evident from Figure C1 is that the mixing from the continuous profiles would be vigorous in the region between h_c and h_m, where there is nonzero diffusivity and property gradients. In contrast, the discrete profile results in no mixing anywhere because at layer interfaces above h_d, where there is diffusivity, there are no property gradients, and at deeper interfaces, where there are gradients, there is no boundary layer diffusivity.

As h_m of the idealized profiles varies from 8 to 22 m, the difference between h_d and h_c is always much less than the layer thickness of 5 m. Relative to the grid resolution, therefore, h_d is a good estimate of h_c, but it oscillates and has a systematic bias. In a situation of steady deepening, h_c is proportional to time, and the solid curve of Figure C2 approximates the deepening of h_d. Increasing resolution dampens the oscillations and reduces the bias, so that the solid curve approaches the dashed line of perfect agreement between h_d and h_c. In practice, low-resolution simulations of deepening do exhibit similar behavior. In Appendix D the numerics of the interior to boundary layer matching are used to dampen the oscillations and remove the bias.

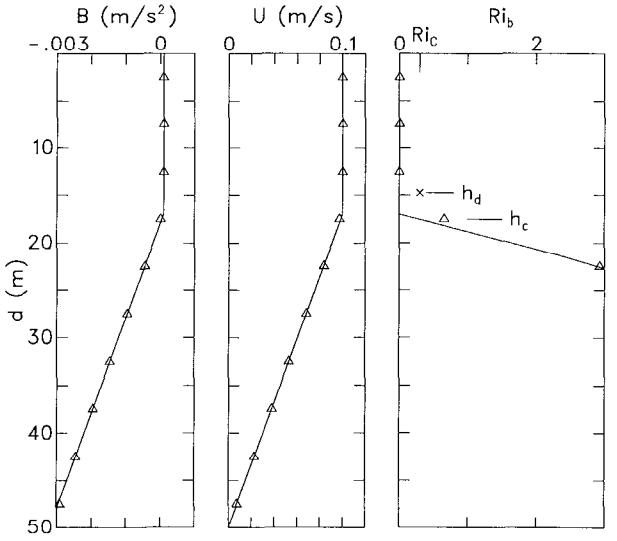

Figure C1. Continuous (solid traces) and discretized (triangles) profiles of buoyancy, horizontal speed (U, with $V = 0$), and bulk Richardson number (equation (21)) from idealized conditions of a 17-m mixed layer above a seasonal thermocline with linear stratification and constant shear. Also shown are the diagnosed boundary layer depths from the continuous (h_c) and discrete (h_d) Richardson number profiles.

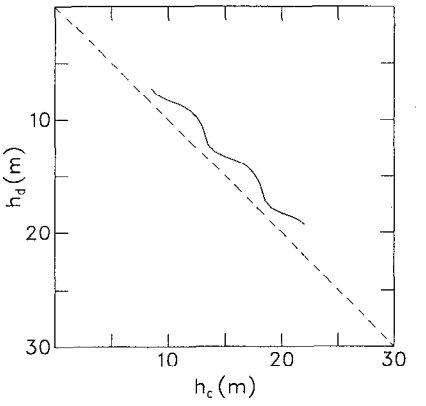

Figure C2. Plot of boundary layer depths h_d, diagnosed from low-resolution discrete profiles, versus h_c from continuous profiles. Note the systematic bias relative to the dashed line of perfect agreement.

In purely convective forcing, Figure 1 shows that the vertical extent of the region of negative buoyancy flux can be small. Therefore this region will not be well resolved, and the model cannot be expected to reproduce the details of convective deepening. However, with the Appendix D numerics, the overall effect of this process is well simulated. Using the results of the pure convective simulation at day 3.0 (Figure 1) as initial conditions, three experiments were run with $\Delta z = 0.2$, 2.0, and 3.33 m. After 2 days the boundary layer deepens by more than the coarsest resolution, from 13.5 to 17.5 m. This time is purposefully chosen for display in Figure C3 because it is most unfavorable to the moderate-resolution grid (crosses). Figure C3 also shows the evolved fine-resolution (solid trace) and coarse-resolution (circles) and the initial (dashed trace) temperature profiles. The unstable gradient in the surface layer is resolved only with the highest resolution, so there are differences in the temperatures at the shallowest grid points, but average temperatures over the surface layer used in (21) differ by less than 0.01°C. In the entrainment region the temperature comparison depends on where the mixed layer is in relation to the discrete model layers. After the two days, $h_m = 17$ m is near a layer interface of the coarse grid, and the temperatures of the neighboring layers are within 0.02°C of the high-resolution temperatures (solid line). In the medium-resolution case at this time, however, h_m is near a grid level, and the temperature is nearly 0.1°C less than the high-resolution case. This temperature difference decreases rapidly as the mixed layer moves away from the grid point level, and it becomes negligible when the mixed layer deepens to

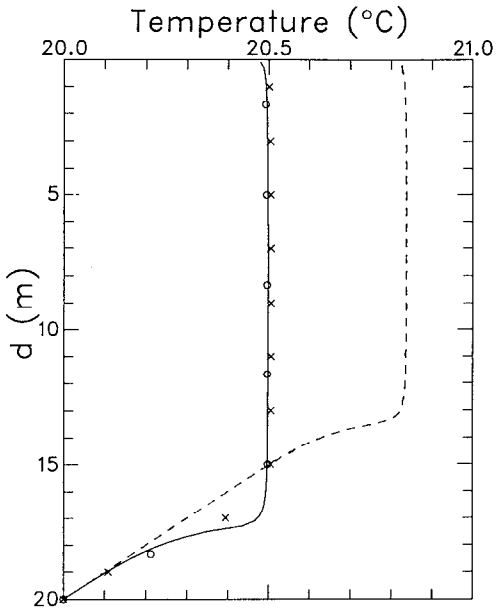

Figure C3. The potential temperature profile (dashed line) at day 3.0 of a pure convective simulation corresponding to Figure 1, and the evolved profiles after 2.0 more days of $Q_t = -100$ W m^{-2} cooling at resolutions of $\Delta z = 0.2$ m (solid trace), 2.0 m (crosses), and 3.33 m (open circles).

near the next interface. At this later time it is the coarse grid temperature at 18.33 m that differs significantly from its neighboring fine-grid temperatures.

LOTUS Sensitivities and Determination of h_B and h_γ

The KPP LOTUS simulation is sensitive to the treatment of solar radiation in (A3) and (A4), and the SST time series from possible combinations of h_B and h_γ are shown in Figure C4, along with the observations (solid trace). With $h_B = h_\gamma = h$, the nonlocal transport becomes zero during the daylight hours of stable forcing. Any effect of a nonzero $\overline{w\theta}_R$ is therefore limited to short periods near sunrise and sunset when there is unstable forcing and daylight. Thus this case is indistinguishable from $h_B = h$, $h_\gamma = 0$ (Figure C4, dashed trace). If solar radiation is included in neither B_f nor γ_θ ($h_B = h_\gamma = 0$), the forcing is always unstable, and the amplitude of the diurnal cycle is reduced by about 0.4°C on days 196, 197, and 198 (Figure C4, dot-dashed trace). Unfortunately, this difference is too small to allow the observations to determine which is the better treatment, because of uncertainties in the forcing and unknown advective effects. On the other days there are no significant differences in the two simulations. If it is assumed that the peculiar diurnal cycle observed on day 198 is due to advection, since the forcing appears to have been similar to the preceding 4 days, then including solar radiation in B_R, $h_B = h$ does give somewhat better agreement with observations. As a note, the effect of including the solar flux into B_f is felt primarily through the influence on the diffusivities K_x through the dependency of the turbulent velocity scale w_x on ϕ_x and hence stability. Including a solar component in B_f also alters h via the turbulent velocity shear V_t in the bulk Richardson number Ri_b (23), but this appears to be a secondary effect.

Figure C4 (dotted trace) also shows the simulation with $h_B = 0$, $h_\gamma = h$. The poor agreement with observations is satisfying because this situation is not physical and the model should not behave well in such a configuration. The forcing is always unstable ($\overline{w\theta}_0 > 0$), so the nonlocal transport is not set to zero during the day. Instead, the absorbed solar radiation makes $\overline{w\theta}_R$ (equation (A4)) sufficiently negative that γ_θ (equation (20)) becomes negative. Thus the nonlocal transport becomes a downgradient contribution to the heat flux, which is contrary to the physics behind this term.

The critical Richardson number Ri_c in the standard LOTUS simulation equals 0.3, and a value of 1.5 is

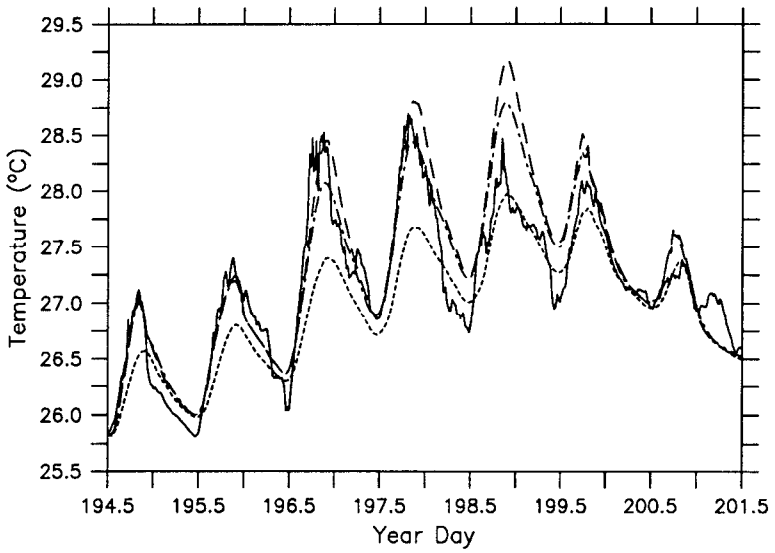

Figure C4. Seven-day time series of observed (solid trace) LOTUS temperature at 0.6-m depth and the corresponding simulated temperature from KPP run in three different modes, namely, $h_B = h_\theta = 0$ (dash-dot trace), $h_B = 0$, $h_\gamma = h$ (dotted trace), and $h_B = h$, $h_\gamma = 0$ (dashed trace). The latter is indistinguishable from the case of $h_B = h_\gamma = h$, which is therefore not shown.

used for the constant C_v. Increasing either value acts to deepen the computed PBL depth h and thus to increase entrainment rates, decrease the model SST, and degrade the simulation. Higher values for Ri_c and C_v also result in surface mixed-layer penetration down to the 5-m thermistor during the night convection period, a feature absent in the LOTUS data (Figure 8). The sensitivity of the near-surface temperature to these parameters is modest, however. Also, changing Ri_c and/or C_v does not appreciably change the amplitude of the diurnal SST variations. Based on the LOTUS data, reasonable values for Ri_c and C_v are in the ranges 0.25–0.5 and 1.25–1.50, respectively. Removing the constraint that h be less than the Monin-Obukhov depth L does not significantly alter the model solution in this particular case. However, without this restriction and with $h_B = h$, idealized diurnal cycles with no wind give an unphysical abrupt surface cooling following the onset of the solar heating.

Interior mixing does play an important role in the LOTUS simulation. The background internal wave mixing below h influences the model solution by transporting heat away from the surface layer and into the 5- to 15-m depth range. Background scalar diffusivities ν_s^w (equation (29)) greater than 0.3×10^{-4} m^2 s^{-1} result in too much entrainment and subsurface heating at the 5- and 10-m model depths. Shear instability mixing (28) acts in the standard case primarily to reduce the magnitude of the diurnal SST cycle for some days. The shear instability and internal wave mixing in the model

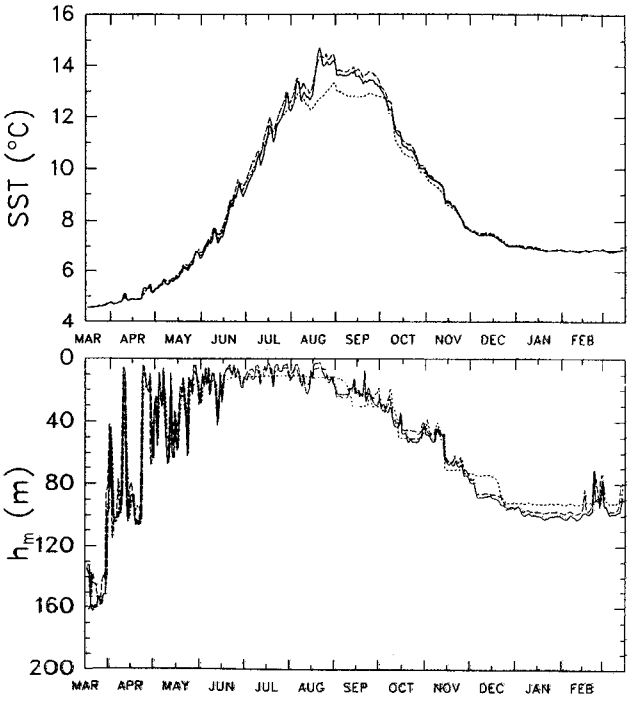

Figure C5. Annual cycle, starting March 15, 1961, of SST and h_m for the standard OWS Papa simulation (solid trace) and for two lower-resolution runs with Δz = 10 m (dashed trace) and Δz = 20 m (dotted trace).

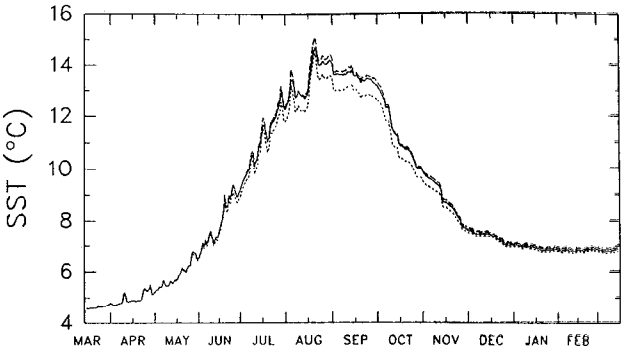

Figure C6. Annual cycle, starting March 15, 1961, of SST from the standard OWS Papa simulation (solid trace) and from a higher-resolution (Δz = 2 m) run with Ri_0 = 0.7 (dotted trace) and Ri_0 = 0.5 (dashed trace).

are interconnected in that if the latter is set to zero, more momentum is trapped in the boundary layer, leading to enhanced shear instability mixing. Thus the model LOTUS solution is insensitive to the exact form of the interior mixing, needing only for it to be active in the model to limit the maximum daily SST values.

Resolution Dependence of the Annual Cycle

The annual cycles from KPP simulations of OWS Papa at three resolutions are shown in Figure C5. There are no significant differences in either SST evolution or mixed-layer depth between the Δz = 5 m and 10 m cases. Both the high- and low-frequency variability are well correlated. With 20-m resolution, however, the boundary layer itself is not resolved in summertime, and as can be expected, the SSTs are too cold because heat is distributed evenly in the upper 20 m. Nonetheless, the distribution of heat in the upper ocean appears to be unaffected because in all three cases the interpolated mixed layer depths agree to within the resolution differences. Whenever there are grid points in the mixed layer, the 20-m resolution compares favorably with the higher-resolution simulations of both temperature and mixed-layer depth. All three cases give nearly identical SSTs in spring, fall, and winter, and comparable mixed-layer depths throughout the year.

If the vertical resolution gets too fine and the time step remains too long (3 hours), however, significant differences from the standard run emerge, as in the case shown in Figure C6, with Δz = 2 m. Most noticeable are the colder SSTs (dotted trace) relative to the standard simulation (solid trace) that are produced by a tendency for more interior mixing when the mixed layer is shallow. The interior temperatures then become correspondingly warmer. The first encounter with this problem occurs in late June. At this time, just below the influence of the boundary layer, the gradient Richardson number becomes less than 0.30, which leads to thermal diffusivities greater than 30×10^{-4} m^2

s^{-1} (Figure 3) and heat fluxes of about -800 W m^{-2}. The corresponding values in the standard run are $Ri_g = 0.50$, $K_\theta = 10 \times 10^{-4}$ m^2 s^{-1}, and a heat flux of about -200 W m^{-2}. The net result is that the $\Delta z = 2$ m case begins to have lower SSTs. Although such flux differences are short-lived, they are systematic and occur often enough to cause the persistent SST differences shown in Figure C6 from June to November. The effect on mixed-layer depth is not noticeable until September, but then it lasts through the winter. A high-resolution case ($\Delta z = 2$ m) can be made very similar to the standard simulation by reducing the Ri_0 parameter of (28) from 0.7 to between 0.5 and 0.6, or by reducing the time step by about a half. The sensitivity to Ri_0 is illustrated in Figure C6, where a case with $Ri_0 = 0.5$ (dashed trace) shows SSTs systematically slightly warmer than the standard case from July onwards.

Removing the restrictions that h be less than both L and h_E in stable forcing conditions changed neither the SST or h_m evolution by any appreciable amount from the standard case.

APPENDIX D: NUMERICAL IMPLEMENTATION

This appendix details how the ocean model described in this paper is numerically implemented in finite difference form. These numerics are not unique solutions to the various problems encountered and alternatives are possible. However, to reproduce the results shown in this paper, similar numerics may be required.

Vertical Discretization

The discrete vertical grid d_n is formed from a transform variable ξ, which varies from 0 to 1 as the distance d from the boundary goes from 0 to the prescribed model depth D. This depth is partitioned into a number M of layers, each of constant thickness in ξ. Following *McWilliams et al.* [1990], a dimensionless parameter λ is used to control the resolution as a function of d:

$$\xi(d) = (1 - e^{\lambda d/D})/(1 - e^{\lambda})$$
$$d(\xi) = (D/\lambda) \ln [1 - \xi(1 - e^{\lambda})] \quad \text{(D1)}$$

For $\lambda < 0$, model layers are concentrated near the surface, and the resolution degrades with d faster as λ becomes more negative. For $\lambda > 0$, there is better resolution near $d = D$. In the limit $\lambda \to 0$, (D1) becomes $\xi(d) = d/D$, and the resolution is constant at $\Delta z = D/M$.

Layer interfaces are denoted by fractional indices and found at $\xi_{n+0.5} = nM^{-1}$; $n = 0, M$. Layer grid points are denoted by whole number indices and are at $\xi_n = (n - 0.5)M^{-1}$; $n = 1, M$. The layer thicknesses are $\Delta_n = d_{n+0.5} - d_{n-0.5}$, and the distances between grid levels are $\Delta_{n+0.5} = d_{n+1} - d_n$. To define the latter for $n = 0$ and $n = M$, d_0 is taken to be zero, and a fictitious layer, $M + 1$, of zero thickness is added at the bottom. An index k can always be found such that $d_{k-1} \le h < d_k$. A useful variable that varies from 0 to 1 over this grid interval is

$$\delta = (h - d_{k-1})/\Delta_{k-0.5} \quad \text{(D2)}$$

Property values are defined at the grid levels d_n for $1 \le n \le M + 1$, where the $M + 1$ values are prescribed bottom boundary conditions. In computing near-surface reference values X_r as the average value between the surface and εh, the following continuous profile is assumed:

$$X(d) = X_1 \qquad d < d_1$$
$$X(d) = X_{n-1} + \frac{(X_n - X_{n-1})}{(d_n - d_{n-1})}(d - d_{n-1}) \quad \text{(D3)}$$
$$d_1 \le d_{n-1} \le d < d_n \le D$$

Property gradients are required both at interfaces and grid levels, and in the ocean, where partial derivatives with respect to d equal $-\partial_z$, these are computed as

$$[\partial_z X]_{n+0.5} = \frac{X_n - X_{n+1}}{\Delta_{n+0.5}} \qquad 1 \le n \le M \quad \text{(D4a)}$$

$$[\partial_z X]_n = \frac{X_{n-1} - X_{n+1}}{\Delta_{n-0.5} + \Delta_{n+0.5}} \qquad 1 < n \le M$$

$$[\partial_z X]_n = \frac{X_1 - X_2}{2\Delta_{1.5}} \qquad n = 1 \quad \text{(D4b)}$$

Interior–Boundary Layer Matching

In Appendix C, both the convective and wind deepening cases were shown to be handled well, but not ideally by a low-resolution KPP model. Several techniques were explored in an attempt to dampen the oscillations and reduce the bias in h (Figure C2). One approach is to use nonlinear interpolation. Several schemes were tested and they could be made to work very well with idealized profiles, such as the those of Figure C1. However, in general, the property profiles, and especially the bulk Richardson number profile, are highly variable, and no one scheme could be found to work well over a wide variety of naturally occurring conditions.

The following practical scheme is used to remove the bias and dampen the oscillations. It involves overcoming the lack of mixing discussed above for Figure C1 by enhancing the diffusivity at the $k - 0.5$ interface. Figure D1 shows the diffusivities produced by the model's parameterizations in the vicinity of layer k for two situations: (1) $d_{k-1} < h < d_{k-0.5}$ (Figure D1a) and (2) $d_{k-0.5} < h < d_k$ (Figure D1b). The first step in

the matching process is to determine the interior diffusivities (triangles). These are interpolated (dotted line) to give $\nu_x(h)$ and the gradient, $\partial_z\nu_x(h)$, at h. The only important requirement here is that there be discontinuities in neither quantity as h progresses through the grid. This is true of the simple scheme used in the model:

$$\nu_x(h) = \nu_x(d_{n+0.5}) + \partial_z\nu_x(h)(d_{n+0.5} - h) \qquad \text{(D5a)}$$

$$d_{n-0.5} < h \leq d_{n+0.5}$$

$$\partial_z\nu_x(h) = (1 - R)\left[\frac{\nu_x(d_{n-0.5}) - \nu_x(d_{n+0.5})}{\Delta_n}\right] + R\left[\frac{\nu_x(d_{n+0.5}) - \nu_x(d_{n+1.5})}{\Delta_{n+1}}\right] \qquad \text{(D5b)}$$

with $n = k - 1$ in situation 1 and $n = k$ in situation 2. The interpolated gradient is just a weighted average of two discrete gradients, with the weight $R = (h - d_{n-0.5})\Delta_n^{-1}$. With these values, (18) can be solved and substituted into (17) to give the two variable coefficients, a_2 and a_3, of the shape function $G(\sigma)$ (equation (11)). The continuous boundary layer diffusivity profile (solid trace) is then completely specified by (10). The dotted trace of Figure D1 follows the $\nu_x(h)$ that would be computed from (D5) for different values of h between $d_{k-1.5}$ and $d_{k+0.5}$.

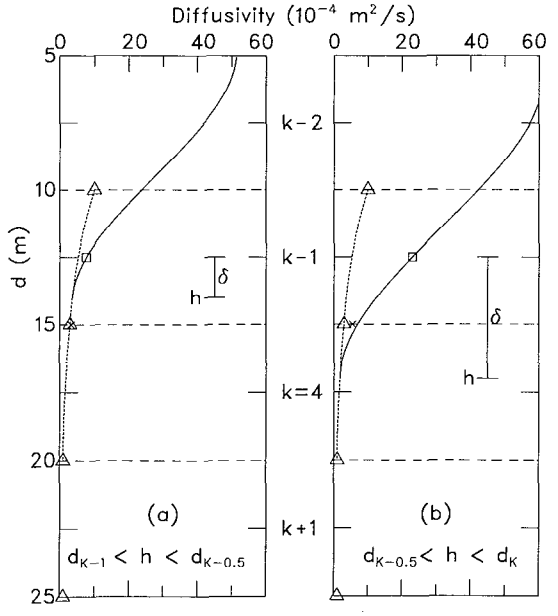

Figure D1. Schematic of the diffusivities required to match the interior and boundary layer mixing for two cases: (a) h between d_{k-1} and $d_{k-1/2}$, and (b) h between $d_{k-1/2}$ and d_k. Shown are the discrete interior diffusivities (triangles) and their interpolation (dashed curve) from (A5); the continuous boundary layer diffusively profile $K_x(d)$ (solid trace) from (13), including its value at d_{k-1} (square); and finally the modified diffusivity at $d_{k-1/2}$, Λ_x, which is used by the model (cross).

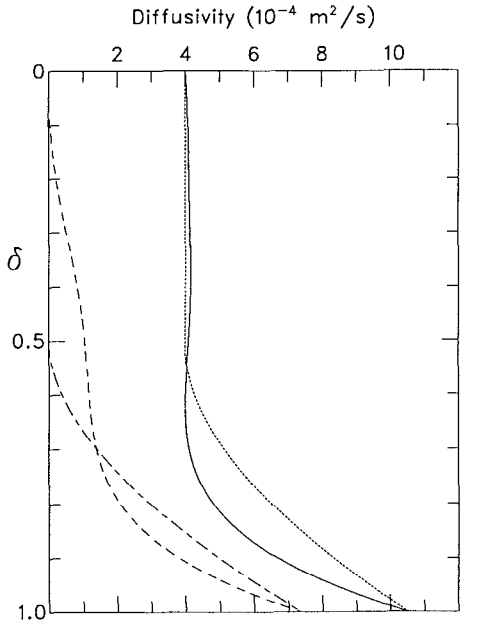

Figure D2. Comparison of Λ_x used by the model and $K_x(d_{k-0.5})$ as δ varies from 0 to 1. Shown are a case of no interior mixing (Λ_x, dashed trace; K_x, dot-dashed trace) and a case with substantial interior mixing (Λ_x, solid trace; K_x, dotted trace).

The next step is to compute a modified diffusivity, Λ_x (cross in Figure D1), which is to be applied at the $k - 0.5$ interface. It is a weighted average of $\nu_x(d_{k-0.5})$ (triangle) and an enhanced boundary layer diffusivity, K_x^*, such that for case 2 situations

$$\Lambda_x = (1 - \delta)\nu_x(d_{k-0.5}) + \delta K_x^*$$
$$K_x^* = (1 - \delta)^2 K(d_{k-1}) + \delta^2 K(d_{k-0.5}) \qquad \text{(D6)}$$

where δ, as defined as (D2), varies from 0 to 1. For case 1, $\nu_x(d_{k-0.5})$ replaces $K(d_{k-0.5})$ in (D6) because the latter is not defined by (10) for $d > h$. The important feature is that the dependency on $K(d_{k-1})$ (square) leads to an enhanced diffusivity at the $k - 0.5$ interface as soon as h becomes greater than d_{k-1}. The increased deepening that results greatly reduces the boundary layer depth bias (Figure C2) of low-resolution, relative to high-resolution, simulations.

Figure D2 compares the diffusivity Λ_x used by the model with the boundary layer diffusivity at $d_{k-0.5} = 15$ m, as δ varies from 0 to 1. The latter are kept small by using a small $u^* = 0.006$ m s^{-1} and by using the grid of Figure D1 with $k = 4$, so that h does not get very large. Two extreme cases are shown: no interior mixing (dashed versus dot-dashed lines) and substantial interior mixing (solid versus dotted lines). In the latter case the interior diffusivities are 1, 2, 4, and 8 $\times$ 10^{-4} m^2 s^{-1} at 25-, 20-, 15-, and 10-m depth, respectively. The boundary layer diffusivities at the $k - 0.5$ interface in the range $0 \leq \delta \leq 0.5$ are constant at the interior value. The importance of using Λ_x is to en-

hance these diffusivities in this range of δ when the interior diffusivity is small. When there is substantial interior mixing, as in the cases shown in Figures D1 and D2, the enhancement is not necessary and is much reduced. As δ approaches 1, the form of (D6) makes Λ_x less than $K_x(d_{k-0.5})$ in an attempt to reduce biases.

Semi-Implicit Time Integration

The prognostic equations of the one-dimensional model, given by (35), are solved with a semi-implicit integration scheme whose general matrix form is

$$\mathbf{A}_x^i \mathbf{X}_{t+1}^{i+1} = \mathbf{X}_t + \mathbf{H}_x^i \tag{D7}$$

where $\mathbf{A}$ is an $M \times M$ tridiagonal matrix and $\mathbf{X}$ and $\mathbf{H}$ are vectors of length M. Integration over a time step Δt is accomplished by inversion of $\mathbf{A}$, which allows the properties at the new time $t + 1$ to be computed from past values at t. The integration can be only semi-implicit because $\mathbf{A}$ and $\mathbf{H}$ depend on quantities like the diffusivity that depend on h, which in turn depends on the profiles $\mathbf{X}_{t+1}$ that are themselves computed from $\mathbf{A}$ and $\mathbf{H}$. The superscripts in (D7) denote various choices of when and how $\mathbf{A}$ and $\mathbf{H}$ are calculated. The simplest method, denoted by $i = 0$, would be to compute all the required quantities, including the forcing, at time t using $\mathbf{X}_t$ values. In some numerical schemes the prognostic variables are updated by advection prior to vertical diffusion, so that these updated $\mathbf{X}_{t+1}^0$ values could also be used.

In our applications, (D7) has been iterated until the new boundary layer depth from the ith iteration, h^{i+1}, differs from the previous h^i by less than a specified tolerance, η_h:

$$|h^i - h^{i+1}|/\Delta_k < \eta_h \tag{D8}$$

where again $d_{k-1} \le h^{i+1} \le d_k$ defines the vertical index k, and Δ_k is the local vertical resolution. Iteration allows the $\mathbf{X}_{t+1}^i$ values used to determine $\mathbf{A}_x^i$ and $\mathbf{H}_x^i$ to be close to the final $\mathbf{X}_{t+1}^{i+1}$ values. Either $\mathbf{X}_t$ or $\mathbf{X}_{t+1}^0$ could be used for the first iteration, $i = 1$. Alternatively, we use linear extrapolations of $\mathbf{X}_{t-1}$ and $\mathbf{X}_t$ to give the first iteration $\mathbf{X}_{t+1}^1$ values. Since it is undesirable to use the extrapolated values in the final iteration, at least two iterations are always performed. Over an annual cycle at OWS Papa, fewer than 1% of all time integrations required more than two iterations. At most, 12 iterations were needed, but 0.3 percent of all iterations (when the stratification was weak) failed to converge, and the results of the twentieth iteration were used.

The elements of $\mathbf{A}$ have the same form for all properties, so the subscript x can be dropped for convenience. The elements of $\mathbf{A}$ then become $A_{n,m}$, where n is the row index and m is the column. The nonzero elements are

$$A_{1,1} = (1 + \Omega_1^+) \tag{D9a}$$

$$A_{n,n-1} = -\Omega_n^- \qquad 2 \le n \le M \tag{D9b}$$

$$A_{n,n} = (1 + \Omega_n^- + \Omega_n^+) \qquad 2 \le n \le M \tag{D9c}$$

$$A_{n,n+1} = -\Omega_n^+ \qquad 1 \le n \le M - 1 \tag{D9d}$$

where

$$\Omega_n^- = \frac{\Delta t}{\Delta_n} \frac{K_x(d_{n-0.5})}{\Delta_{n-0.5}} \qquad \Omega_n^+ = \frac{\Delta t}{\Delta_n} \frac{K_x(d_{n+0.5})}{\Delta_{n+0.5}}$$

The vector $\mathbf{H}$ is very different for scalars than for velocity. In general, the scalar $\mathbf{H}$ includes the boundary conditions, countergradient terms, and nonturbulent forcing. Let J be the nonturbulent forcing at the interfaces, $Q_n(d)$ for temperatures and $-F_n(d)$ for salinity, with J_0 the surface value. For a surface turbulent flux of $\overline{ws}_0$, the elements of $\mathbf{H}_s$ are

$$H_1 = \frac{\Delta t}{\Delta_1} ((K_s\gamma_s)_{1.5} - \overline{ws}_0 + J_{1.5} - J_0) \tag{D10a}$$

$$H_n = \frac{\Delta t}{\Delta_n} ((K_s\gamma_s)_{n+0.5} - (K_s\gamma_s)_{n-0.5} + J_{n+0.5} - J_{n-0.5}) \qquad 2 \le n \le M - 1 \tag{D10b}$$

$$H_M = \frac{\Delta t}{\Delta_M} \left((K_s\gamma_s)_{M+0.5} - (K_s\gamma_s)_{M-0.5} + J_{M+0.5} - J_{M-0.5} + S_{M+1} \frac{K_s(d_{M+0.5})}{\Delta_{M+0.5}} \right) \tag{D10c}$$

where S_{M+1} is the prescribed bottom boundary value of the scalar and subscripts in $n + 0.5$ and $n - 0.5$ denote evaluation at $d_{n-0.5}$ and $d_{n+0.5}$, respectively.

For velocity components, $\mathbf{H}$ includes only boundary conditions and Coriolis terms. For the zonal component the elements of $\mathbf{H}_u$ are

$$H_1 = \Delta t f V_1^{t+0.5} - \frac{\Delta t}{\Delta_1} \overline{wu}_0 \tag{D11a}$$

$$H_n = \Delta t f V_n^{t+0.5} \qquad 2 \le n \le M - 1 \tag{D11b}$$

$$H_M = \Delta t f V_M^{t+0.5} + \frac{\Delta t}{\Delta_M} \frac{U_{M+1} K_m(d_{M+0.5})}{\Delta_{M+0.5}}. \tag{D11c}$$

For the meridional component the elements of $\mathbf{H}_v$ are

$$H_1 = -\Delta t f U_1^{t+0.5} - \frac{\Delta t}{\Delta_1} \overline{wv}_0 \tag{D12a}$$

$$H_n = -\Delta t f U_n^{t+0.5} \qquad 2 \le n \le M - 1 \tag{D12b}$$

$$H_M = -\Delta t f U_M^{t+0.5} + \frac{\Delta t}{\Delta_M} \frac{V_{M+1} K_m(d_{M+0.5})}{\Delta_{M+0.5}} \tag{D12c}$$

In (D11) and (D12) the fixed bottom boundary conditions are U_{M+1} and V_{M+1}. The Coriolis terms are estimates of their average value over the time step:

$$U_n^{t+0.5} = 0.5(U_n^t + U_n^i)$$
$$V_n^{t+0.5} = 0.5(V_n^t + V_n^i) \quad \text{(D13)}$$

where the layer n velocity components at time t and U_n^t and V_n^t.

NOTATION

$\mathbf{A}$ M by M tridiagonal matrix, with nonzero elements $A_{n,m}$.
A_S vertical plus horizontal advection of salt.
A_T vertical plus horizontal advection of potential temperature.
A_m amplitude of an idealized inertially rotating wind stress.
a_0, a_1, a_2, a_3 polynomial coefficients of shape function $G(\sigma)$.
a_m, c_m, a_s, c_s coefficients of ϕ_m and ϕ_s in their 1/3 power law regimes.
B, b mean and turbulent buoyancy components.
B_f surface buoyancy forcing.
B_R radiative contribution to the surface buoyancy forcing B_f.
B_r near-surface reference buoyancy.
C_D neutral 10-m bulk momentum transfer (drag) coefficient.
C_E neutral 10-m bulk moisture transfer coefficient (Dalton number).
C_θ neutral 10-m bulk heat transfer coefficient (Stanton number).
C_v ratio of interior N to N at h_e.
C_b empirical constant parameterizing the buoyancy of convective elements.
C_s, C^* proportionality coefficients parameterizing γ_s.
D vertical depth of the model.
d distance coordinate from the boundary.
$\bar{e}$ turbulent kinetic energy.
F_T temperature flux across a diffusive interface.
$F_n(d)$ nonturbulent freshwater flux.
F_t surface turbulent freshwater flux.
f local Coriolis parameter.
$G(\sigma)$ nondimensional vertical shape function for diffusivities.
g gravitational acceleration.
$\mathbf{H}$ vector of length M and elements H_n.
h boundary layer depth.
h_c, h_d continuous and discrete boundary layer depths.
h_E Ekman depth.
h_e entrainment depth.
h_m mixed-layer depth.
h_B depth to which absorbed solar radiation contributes to B_f.
h_γ depth to which absorbed solar radiation contributes to γ_s.
$I_0, I(d)$ net solar irradiance at the surface and at depth d.
IKE_m inertial mean kinetic energy in a mixed layer.
$J_{n+0.5}$ generalized nonturbulent forcing at the interface between layers n and $n + 1$.
K_x generalized diffusivity in the boundary layer.
K_x^* enhanced boundary layer diffusivity at the $k - 0.5$ interface.
L Monin-Obukhov length scale.
L_e turbulent kinetic energy length scale.
L_m significant eddy size or mixing length.
L_0 asymptotic value of L_m.
M number of discrete model layers.
m subscript denoting applicability to momentum variables.
N local buoyancy frequency.
NI number of solar wavelength bands.
P precipitation.
Pr turbulent Prandtl number.
PE potential energy of the water column.
p_1, p_2 exponents of parameterization functions.
Q_A surface heat flux averaged over 1 year.
$Q_t(d)$ turbulent heat flux profile.
$Q_n(d)$ nonturbulent heat flux profile.
Q_t net surface turbulent heat flux.
R_ρ double-diffusive density ratio $(\alpha\partial_z T)/(\beta\partial_z S)$.
R_ρ^0 value of R_ρ where ν_x^d goes to zero in salt fingering.
Ri_b bulk Richardson number across the boundary layer.
Ri_c critical bulk Richardson number.
Ri_g local gradient Richardson number.
Ri_0 value of Ri_g where ν_x^s goes to zero.
r_i fraction of solar radiation in wavelength band i.
S, s mean and turbulent components of salinity, or generalized scalar.
S_I salinity of sea ice.
S^* turbulent flux scale for salinity, or generalized scalar.
s subscript denoting applicability to scalar variables.
T mean potential temperature component.
T^* turbulent potential temperature scale.
T_i inertial period.
T_r near-surface reference potential temperature.
t time coordinate.
U, u mean and turbulent eastward velocity components.
U_{10} wind speed at $z = 10$ m.

u^* turbulent friction velocity.
V, v mean and turbulent northward velocity components.
$\mathbf{V}(d)$ boundary layer horizontal velocity profile.
$\mathbf{V}_r$ near-surface reference horizontal velocity vector.
V_t velocity scale of turbulent velocity shear.
W, w mean and turbulent upward vertical velocity components.
w^* convective velocity scale, $(-B_f h)^{1/3}$.
w_x generalized turbulent velocity scale.
w_m, w_s turbulent velocity scale for momentum and scalars.
$\overline{wx}_0$ generalized turbulent kinematic flux at the surface.
$\overline{w\theta}_R$ radiative contribution to the parameterization γ_θ.
X generalized mean component (U, V, T, S, B).
X_m generalized mean value in a mixed layer.
X_0 generalized mean surface value of U, V, T, S or B.
x generalized turbulent component (u, v, θ, s, b).
z upward vertical coordinate.
z_x generalized roughness length for momentum or scalars.
α thermal expansion coefficient.
β expansion coefficient for salt.
β_r fractional loss of flux at $\sigma = \varepsilon$.
β_T ratio of entrainment flux to surface buoyancy flux.
γ_θ, γ_s boundary layer nonlocal transport.
Δ_n thickness of model layer n.
$\Delta_{n+0.5}$ distance between grid levels n and $(n + 1)$.
ΔX jump across an interference in T, B, U, V or S.
∂ partial derivative.
δ $(h - d_{k-1})/\Delta_{k-0.5}$.
ε nondimensional extent of the surface layer, 0.10.
ζ stability parameter, equal to d/L.
ζ_m, ζ_s maximum ζ values of the $-1/3$ power law regimes of ϕ_m and ϕ_s.
θ turbulent potential temperature component.
η_h implicit integration iteration tolerance on h.
κ von Kármán's constant, 0.40.
Λ_x modified diffusivity at the $k - \frac{1}{2}$ interface.
λ dimensionless grid stretching parameter.
μ_i reciprocal of the absorption coefficient for solar wavelength band i.
ν molecular viscosity, 1.5×10^{-6} m^2 s^{-1}.
ν_x generalized interior diffusivity.
ν_x^s generalized interior diffusivity for shear instability mixing.
ν_x^w generalized interior diffusivity for internal wave mixing.
ν_x^d generalized interior diffusivity for double diffusive mixing.
ν^0 scaling factor for ν_x^s, 50×10^{-4} m^2 s^{-1}.
ν_f scaling factor for ν_x^d in salt fingering, 10×10^{-4} m^2 s^{-1}.
ξ vertical grid stretching transform variable.
ρ_0 density of surface seawater.
$\rho_0(0)$ density of surface fresh water.
$\rho_0(S_I)$ density of surface water of salinity S_I.
$\sigma = d/h$ nondimensional vertical coordinate in the boundary layer.
τ_0 surface wind stress vector.
τ_u, τ_v zonal and meridional components of τ_0.
ψ_m, ψ_s integrals of the ϕ functions.
ϕ_m, ϕ_s dimensionless flux profiles for momentum and scalars.
Ω_n^-, Ω_n^+ components of matrix elements $A_{n,n-1}$, $A_{n,n}$ and $A_{n,n+1}$.

ACKNOWLEDGMENTS. Financial support for this work was gratefully received from the National Oceanic and Atmospheric Administration (NOAA order NRAZ0-000200115) through its Atlantic Climate Change Program. S. Doney was supported by a postdoctoral fellowship from the Advanced Study Program of the National Center for Atmospheric Research (NCAR). NCAR is supported by the National Science Foundation. We gratefully acknowledge the programming support of Jan Morzel in all aspects of this work. Jim Price, Paul Martin, and Jim Moum generously supplied the LOTUS data, the 20 years of meteorological and oceanographic data from OWS Papa, and the Tropic Heat data, respectively. We thank Greg Crawford for sharing the early results of his thesis on the Ocean Storms experiment and Lakshmi Kantha for providing the results from KC simulations.

Douglas Luther was the editor responsible for this paper. He thanks E. Sarachik, M. Perfit, and two anonymous reviewers for their assistance in evaluating the paper.

REFERENCES

Anis, A., and J. N. Moum, The superadiabatic surface layer of the ocean during convection, *J. Phys. Oceanogr.*, *22*, 1221–1227, 1992.

Archer, D., S. Emerson, T. Powell, and C. S. Wong, Numerical hindcasting of sea surface pCO_2 at weathership station Papa, *Prog. Oceanogr.*, *32*, 319–351, 1993.

Ball, F. K., Control of inversion height by surface heating, *Q. J. R. Meteorol. Soc.*, *86*, 483–494, 1960.

Berliand, M. E., and T. G. Berliand, Measurement of the effective radiation of the Earth with varying cloud amounts, *Izv. Acad. Sci. USSR, Ser. Geophys.*, Engl. Transl., no. 1, 1952.

Blackadar, A. K., The vertical distribution of wind and turbulent exchange in a neutral atmosphere, *J. Geophys. Res.*, *67*, 3095–3102, 1962.

Bougeault, P., and J. C. Andre, On the stability of the third order turbulence closure for the modeling of the stratoc-

umulus-topped boundary layer, *J. Atmos. Sci.*, *43*, 1574–1581, 1986.

Briscoe, M. G., and R. A. Weller, Preliminary results from the Long-Term Upper-Ocean Study (LOTUS), *Dyn. Atmos. Oceans*, *8*, 243–265, 1984.

Bunker, A. F., Computations of surface energy and annual air-sea interaction cycles of the North Atlantic Ocean, *Mon. Weather Rev.*, *104*, 1122–1140, 1976.

Businger, J. A., J. C. Wyngaard, Y. Izumi, and E. F. Bradley, Flux-profile relationships in the atmospheric surface layer, *J. Atmos. Sci.*, *28*, 181–189, 1971.

Carl, D. M., T. C. Tarbell, and H. A. Panofsky, Profiles of wind and temperature from towers and homogeneous terrain, *J. Atmos. Sci.*, *30*, 788–794, 1973.

Craik, A. D. D., and S. Leibovich, A rational model for Langmuir circulations, *J. Fluid Mech.*, *73*, 401–426, 1976.

D'Asaro, E. A., Ocean storms—A three-dimensional, severe storm, air/sea interaction experiment: Overview and core program, 39 pp., Appl. Phys. Lab., Univ. of Wash., Seattle, 1985a.

D'Asaro, E. A., Upper ocean temperature structure, inertial currents, and Richardson numbers observed during strong meteorological forcing, *J. Phys. Oceanogr.*, *15*, 943–962, 1985b.

Davis, R. E., R. deSzoeke, D. Halpern, and P. Niiler, Variability in the upper ocean during MILE, I, The heat and momentum balances, *Deep Sea Res., Part A*, *28*, 1427–1451, 1981a.

Davis, R. E., R. deSzoeke, and P. P. Niiler, Variability in the upper ocean during MILE, II, Modeling the mixed layer response, *Deep Sea Res., Part A*, *28*, 1453–1475, 1981b.

Deardorff, J. W., The counter gradient heat flux in the lower atmosphere and in the laboratory, *J. Atmos. Sci.*, *23*, 503–506, 1966.

Deardorff, J. W., A numerical study of three-dimensional channel flow at large Reynolds numbers, *J. Fluid Mech.*, *41*, 453–480, 1970.

Deardorff, J. W., Numerical investigation of neutral and unstable planetary boundary layers, *J. Atmos. Sci.*, *29*, 91–115, 1972a.

Deardorff, J. W., Theoretical expression for the countergradient vertical heat flux, *J. Geophys. Res.*, *77*, 5900–5904, 1972b.

Deardorff, J. W., G. E. Willis, and D. K. Lilly, Laboratory investigation of non-steady penetrative convection, *J. Fluid Mech.*, *35*, 7–31, 1969.

Dobson, F. W., and S. D. Smith, Bulk models of solar radiation at sea, *Q. J. R. Meteorol. Soc.*, *114*, 165–182, 1988.

Donaldson, C., Construction of a dynamic model of the production of atmospheric turbulence and the dispersal of atmospheric pollutants, in *Workshop on Micrometeorology*, edited by D. A. Haugen, pp. 313–392, American Meteorological Society, Boston, Mass., 1973.

Ekman, V. W., On the influence of the Earth's rotation on ocean currents, *Ark. Mat. Astron. Fys.*, *2* (11), 1–53, 1905.

Eriksen, C. C., Measurements and models of fine structure, internal gravity waves, and wave breaking in the deep ocean, *J. Geophys. Res.*, *83*, 2989–3009, 1978.

Fedorov, K. N., Layer thicknesses and effective diffusivities in the diffusive thermocline convection in the ocean, in *Small-Scale Turbulence and Mixing in the Ocean*, edited by J. C. J. Nihoul and B. M. Jamart, pp. 471–479, Elsevier, New York, 1988.

Fung, I. Y., D. E. Harrison, and A. A. Lacis, On the variability of the net longwave radiation at the ocean surface, *Rev. Geophys.*, *22*, 177–193, 1984.

Galperin, B., L. H. Kantha, S. Hassid, and A. Rosati, A quasi-equilibrium turbulent energy model for geophysical flows, *J. Atmos. Sci.*, *45*, 55–62, 1988.

Gargett, A. E., and G. Holloway, Dissipation and diffusion by internal wave breaking, *J. Mar. Res.*, *42*, 15–27, 1984.

Garwood, R. W., An oceanic mixed layer model capable of simulating cyclic states, *J. Phys. Oceanogr.*, *7*, 455–471, 1977.

Gaspar, P., Modeling the seasonal cycle of the upper ocean, *J. Phys. Oceanogr.*, *18*, 161–180, 1988.

Gaspar, P., Y. Gregoris, and J.-M. Lefevre, A simple eddy kinetic energy model for simulations of the oceanic vertical mixing: Tests at station Papa and Long-Term Upper Ocean Study site, *J. Geophys. Res.*, *95*, 16,179–16,193, 1990.

Gill, A. E., and P. P. Niiler, The theory of the seasonal variability in the ocean, *Deep Sea Res.*, *20*, 141–177, 1973.

Gregg, M. C., Diapycnal mixing in the thermocline: A review, *J. Geophys. Res.*, *92*, 5249–5286, 1987.

Gregg, M. C., Scaling turbulent dissipation in the thermocline, *J. Geophys. Res.*, *94*, 9686–9698, 1989.

Haugen, D. A. (Ed.), *Workshop on Micrometeorology*, 392 pp., American Meteorological Society, Boston, Mass., 1973.

Heisenburg, W., On the theory of statistical and isotropic turbulence, *Proc. R. Soc. London A*, *195*, 402–406, 1948.

Högström, U., Non-dimensional wind and temperature profiles in the atmospheric surface layer: A re-evaluation, *Boundary Layer Meteorol.*, *42*, 55–78, 1988.

Holtslag, A. A. M., and B. A. Boville, Local versus nonlocal boundary-layer diffusion in a global climate model, *J. Clim.*, *6*, 1825–1842, 1993.

Holtslag, A. A. M., and C.-H. Moeng, Eddy diffusivity and countergradient transport in the convective atmospheric boundary layer, *J. Atmos. Sci.*, *48*, 1690–1698, 1991.

Holtslag, A. A. M., E. I. F. de Bruijn, and H.-L. Pan, A high resolution air mass transformation model for short-range weather forecasting, *Mon. Weather Rev.*, *118*, 1561–1565, 1990.

Jerlov, N. G., *Marine Optics*, 231 pp., Elsevier, New York, 1976.

Kaimal, J. C., J. C. Wyngaard, D. A. Haugen, O. R. Cote, Y. Izumi, S. J. Caughey, and C. J. Readings, Turbulence structure in the convective boundary layer, *J. Atmos. Sci.*, *33*, 2152–2169, 1976.

Kantha, L. H., and C. A. Clayson, An improved mixed layer model for geophysical applications, *J. Geophys. Res.*, in press, 1994.

Kelley, D. E., Explaining effective diffusivities within diffusive oceanic staircases, in *Small-Scale Turbulence and Mixing in the Ocean*, edited by J. C. J. Nihoul and B. M. Jamart, pp. 481–502, Elsevier, New York, 1988.

Kelley, D. E., Fluxes through diffusive staircases: A new formulation, *J. Geophys. Res.*, *95*, 3365–3371, 1990.

Kim, J., and L. Mahrt, Simple formulation of turbulent mixing in the stable free atmosphere and nocturnal boundary layer, *Tellus, Ser. A*, *44*, 381–394, 1992.

Koop, C. G., and F. K. Browand, Instability and turbulence in a stratified fluid with shear, *J. Fluid Mech.*, *93*, 135–159, 1979.

Koracin, D., and R. Berkowicz, Nocturnal boundary-layer height: Observations by acoustic sounders and predictions in terms of surface layer height parameters, *Boundary Layer Meteorol.*, *43*, 65–83, 1988.

Kraus, E. B., and J. S. Turner, A one-dimensional model of the seasonal thermocline, II, The general theory and its consequences, *Tellus*, *19*, 98–105, 1967.

Kundu, P. K., and R. C. Beardsley, Evidence of a critical

Richardson number in moored measurements during the upwelling season off northern California, *J. Geophys. Res.*, *96*, 4855–4868, 1991.

Kunze, E., A. J. Williams III, and M. G. Briscoe, Observations of shear and vertical stability from a neutrally buoyant float, *J. Geophys. Res.*, *95*, 18,127–18,142, 1990.

Kurzeja, R. J., S. Berman, and A. H. Weber, A climatological study of the nocturnal planetary boundary layer, *Boundary Layer Meteorol.*, *54*, 105–128, 1991.

Large, W. G., and G. C. Crawford, Observations and simulations of upper ocean response to wind events during the Ocean Storms experiment, *J. Phys. Oceanogr.*, in press, 1994.

Large, W. G., and S. Pond, Sensible and latent heat flux measurements over the ocean, *J. Phys. Oceanogr.*, *12*, 464–482, 1982.

Large, W. G., J. C. McWilliams, and P. P. Niiler, Upper ocean thermal response to strong autumnal forcing of the northeast Pacific, *J. Phys. Oceanogr.*, *16*, 1524–1550, 1986.

Ledwell, J. R., A. J. Wilson, and C. S. Low, Evidence for slow mixing across the pycnocline from an open-ocean tracer-release experiment, *Nature*, *364*, 701–703, 1993.

Lenschow, D. H., J. C. Wyngaard, and W. T. Pennell, Mean-field and second-moment budgets in a baroclinic convective boundary layer, *J. Atmos. Sci.*, *37*, 1313–1326, 1980.

Lewis, M. R., N. Kuring, and C. Yentsch, Global patterns of ocean transparency: Implications for the new production of the open ocean, *J. Geophys. Res.*, *93*, 6847–6855, 1988.

Lilly, D. K., The representation of small-scale turbulence in numerical simulation experiments, *Proc. IBM Sci. Comput. Symp. Environ. Sci.*, 195–210, 1967.

Liu, W. T., K. B. Katsaros, and J. A. Businger, Bulk parameterization of air-sea exchanges of heat and water vapor including the molecular constraints at the interface, *J. Atmos. Sci.*, *36*, 1722–1735, 1979.

Louis, J. F., A parametric model of vertical eddy fluxes in the atmosphere, *Boundary Layer Meteorol.*, *17*, 187–202, 1979.

Lukas, R., and E. Lindstrom, The mixed layer of the western equatorial Pacific Ocean, *J. Geophys. Res.*, *96*, 3343–3357, 1991.

Lumley, J. A., and H. A. Panofsky, *The Structure of Atmospheric Turbulence*, 239 pp., John Wiley, New York, 1964.

Mahrt, L., Mixed layer moisture structure, *Mon. Weather Rev.*, *104*, 1403–1418, 1976.

Mahrt, L., and W. Gibson, Flux decomposition into coherent structures, *Boundary Layer Meteorol.*, *60*, 143–168, 1992.

Mailhôt, J., and R. Benoit, A finite-element model of the atmospheric boundary layer suitable for use with numerical weather prediction models, *J. Atmos. Sci.*, *39*, 2249–2266, 1982.

Marmorino, G. O., and D. R. Caldwell, Heat and salt transport through a diffusive thermohaline interface, *Deep Sea Res.*, *23*, 59–67, 1976.

Martin, P. J., Simulation of the ocean mixed layer at OWS November and Papa with several models, *J. Geophys. Res.*, *90*, 903–916, 1985.

McPhee, M. G., A time dependent model for turbulent transfer in a stratified oceanic boundary layer, *J. Geophys. Res.*, *92*, 6977–6986, 1987.

McPhee, M. G., and D. G. Martinson, Turbulent mixing under drifting pack ice in the Weddell Sea, *Science*, *263*, 218–221, 1994.

McWilliams, J. C., N. J. Norton, P. R. Gent, and D. B. Haidvogel, A linear balance model of wind-driven, midlatitude ocean circulation, *J. Phys. Oceanogr.*, *20*, 1349–1378, 1990.

McWilliams, J. C., P. C. Gallacher, C.-H. Moeng, and J. C. Wyngaard, Modeling the oceanic planetary boundary layer, in *Large-Eddy Simulations of Complex Engineering and Geophysical Flows*, edited by B. Galperin and S. A. Orszag, pp. 441–454, Cambridge University Press, New York, 1993.

Mellor, G. L., Retrospect on oceanic boundary layer modeling and second moment closure, in *Parameterization of Small-Scale Processes, Proceedings of the 'Aha Huliko'a Hawaiian Winter Workshop*, edited by P. Muller and D. Henderson, University of Hawaii at Manoa, Honolulu, 1989.

Mellor, G. L., and T. Yamada, A hierarchy of turbulent closure models for planetary boundary layers, *J. Atmos. Sci.*, *31*, 1791–1806, 1974.

Mellor, G. L., and T. Yamada, Development of a turbulence closure model for geophysical fluid problems, *Rev. Geophys.*, *20*, 851–875, 1982.

Moeng, C.-H., and J. C. Wyngaard, Statistics of conservative scalars in the convective boundary layer, *J. Atmos. Sci.*, *41*, 3161–3169, 1984.

Moeng, C.-H., and J. C. Wyngaard, Evaluation of turbulent transport and dissipation closures in second-order modeling, *J. Atmos. Sci.*, *46*, 2311–2330, 1989.

Monin, A. S., and A. M. Yaglom, *Statistical Fluid Mechanics*, vol. 1, 769 pp., MIT Press, Cambridge, Mass., 1971.

Moum, J. N., D. R. Caldwell, and C. A. Paulson, Mixing in the equatorial surface layer and thermocline, *J. Geophys. Res.*, *94*, 2005–2021, 1989.

Nieuwstadt, F. T. M., and H. van Dop (eds.), *Atmospheric Turbulence and Air Pollution Modelling*, 358 pp., D. Reidel, Norwell, Mass., 1982.

Niiler, P. P., Deepening of the wind mixed layer, *J. Mar. Res.*, *33*, 405–422, 1975.

Niiler, P. P., and E. B. Kraus, One-dimensional models of the upper ocean, in *Modelling and Prediction of the Upper Layers of the Ocean*, edited by E. B. Kraus, pp. 143–172, Pergamon, New York, 1977.

O'Brien, J. J., A note on the vertical structure of the eddy exchange coefficient in the planetary boundary layer, *J. Atmos. Sci.*, *27*, 1213–1215, 1970.

Osborn, T. R., Estimates of the local rate of vertical diffusion from dissipation measurements, *J. Phys. Oceanogr.*, *10*, 83–89, 1980.

Pacanowski, R. C., and S. G. H. Philander, Parameterization of vertical mixing in numerical models of the tropical oceans, *J. Phys. Oceanogr.*, *11*, 1443–1451, 1981.

Padman, L., and T. M. Dillon, Vertical fluxes through the Beaufort Sea thermohaline staircases, *J. Geophys. Res.*, *92*, 10,799–10,806, 1987.

Paduan, J. D., and R. A. deSzoeke, Heat and energy balances in the upper ocean at 50°N, 150°W during November 1980 (STREX), *J. Phys. Oceanogr.*, *16*, 25–38, 1986.

Panofsky, H. A., The boundary layer above 30 m, *Boundary Layer Meteorol.*, *4*, 251–264, 1973.

Panofsky, H. A., and J. H. Dutton, *Atmospheric Turbulence: Models and Methods for Engineering Applications*, 397 pp., John Wiley, New York, 1984.

Paulson, C. A., Representation of wind speed and temperature profiles in the unstable atmospheric surface layer, *J. Appl. Meteorol.*, *9*, 857–861, 1970.

Paulson, C. A., and J. J. Simpson, Irradiance measurements in the upper ocean, *J. Phys. Oceanogr.*, *7*, 952–956, 1977.

Peters, H., M. C. Gregg, and J. M. Toole, On the parameterization of equatorial turbulence, *J. Geophys. Res.*, *93*, 1199–1218, 1988.

Pollard, R. T., P. B. Rhines, and R. O. R. Y. Thompson, The deepening of the wind mixed layer, *Geophys. Fluid Dyn.*, *4*, 381–404, 1973.

Prandtl, L., Bericht über Untersuchungen sur augogebildeten Turbulenz, *Z. Angev. Math. Mech.*, *5*, 136–139, 1925.

Preisendorfer, R. W., Secchi disk science: Visual optics of natural waters, *Limnol. Oceanogr.*, *31*, 909–926, 1986.

Price, J. F., Upper ocean response to a hurricane, *J. Phys. Oceanogr.*, *11*, 153–175, 1981.

Price, J. F., R. A. Weller, and R. Pinkel, Diurnal cycling: Observations and models of the upper ocean response to diurnal heating, cooling and wind mixing, *J. Geophys. Res.*, *91*, 8411–8427, 1986.

Price, J. F., R. A. Weller, C. M. Bowers, and M. G. Briscoe, Diurnal response of sea surface temperature observed at the Long-Term Upper Ocean Study (34°N, 70°W) in the Sargasso Sea, *J. Geophys. Res.*, *92*, 14,480–14,490, 1987.

Resnyanskiy, Y. D., Parameterization of the integral turbulent energy dissipation in the upper quasihomogeneous layer of the ocean, *Izv. Acad. Sci. USSR Atmos. Oceanic Phys.*, Engl. Transl., *11*, 453–457, 1975.

Sausen, R., K. Barthel, and K. Hasselmann, Coupled ocean-atmosphere models with flux corrections, *Clim. Dyn.*, *2*, 154–163, 1988.

Schmitt, R. W., Form of the temperature-salinity relationship in the Central Water: Evidence for double-diffusive mixing, *J. Phys. Oceanogr.*, *11*, 1015–1026, 1981.

Schmitt, R. W., Mixing in a thermohaline staircase, in *Small-Scale Turbulence and Mixing in the Ocean*, edited by J. C. J. Nihoul and B. M. Jamart, pp. 435–452, Elsevier, New York, 1988.

Schmitt, R. W., On the density ratio balance in the central water, *J. Phys. Oceanogr.*, *20*, 900–906, 1990.

Simpson, J. J., and C. A. Paulson, Mid-ocean observations of atmospheric radiation, *Q. J. R. Meteorol. Soc.*, *105*, 487–502, 1979.

Smagorinsky, J., General circulation experiments with the primitive equations, 1, The basic experiment, *Mon. Weather Rev.*, *91*, 99–164, 1963.

Smith, S. D., and F. W. Dobson, The heat budget at ocean weather station Bravo, *Atmos. Ocean*, *22*, 1–22, 1984.

Stevenson, J. W., and P. P. Niiler, Upper ocean heat budget during the Hawaii to Tahiti Shuttle Experiment, *J. Phys. Oceanogr.*, *13*, 1894–1907, 1983.

Stramma, L., P. Cornillon, R. A. Weller, J. F. Price, and M. G. Briscoe, Large diurnal sea surface temperature variability: Satellite and in situ measurements, *J. Phys. Oceanogr.*, *16*, 827–837, 1986.

Stull, R. B., Transilient turbulence theory, I, The concept of eddy-mixing across finite differences, *J. Atmos. Sci.*, *41*, 3351–3367, 1984.

Stull, R. B., *An Introduction To Boundary Layer Meteorology*, 666 pp., Kluwer, Norwell, Mass., 1988.

Tabata, S., Variability of oceanographic conditions at ocean station P in the northeast Pacific Ocean, *Trans. R. Soc. Canada*, Vol III, Series IV, 367–418, 1965.

Tennekes, H., The logarithmic wind profile, *J. Atmos. Sci.*, *30*, 234–238, 1973a.

Tennekes, H., A model for the dynamics of the inversion above a convective boundary layer, *J. Atmos. Sci.*, *30*, 558–567, 1973b.

Tricot, C., Estimation des flux chaleur en surface à la station météo-océanographique Papa, *Sci. Rep. 1985/9*, Inst. d'Astron. et de Geophys. G. Lemaître, Univ. Cath. de Louvain, Louvain-La-Neuve, Belgium, 1985.

Troen, I. B., and L. Mahrt, A simple model of the atmospheric boundary layer; Sensitivity to surface evaporation, *Boundary Layer Meteorol.*, *37*, 129–148, 1986.

Turner, J. S., The coupled turbulent transports of salt and heat across a sharp density interface, *Int. J. Heat Mass Transfer*, *8*, 759–767, 1965.

Turner, J. S., *Buoyancy Effects in Fluids*, 368 pp., Cambridge University Press, New York, 1973.

Weller, R. A., and J. F. Price, Langmuir circulation within the oceanic mixed layer, *Deep Sea Res.*, *35*, 711–747, 1988.

Weller, R. A., J. P. Dean, J. Marra, J. F. Price, E. A. Francis, and D. C. Boardman, Three-dimensional flow in the upper ocean, *Science*, *227*, 1552–1556, 1984.

Wells, N. C., A coupled ocean-atmosphere experiment: The ocean response, *Q. J. R. Meteorol. Soc.*, *112*, 355–370, 1979.

Wyngaard, J. C., Lectures on the planetary boundary layer, in *Mesoscale Meteorology—Theories, Observations and Models, NATO ASI, Ser., Ser. C*, edited by D. K. Lilly and T. Gal-Chen, 781 pp., D. Reidel, Norwell, Mass., 1982.

Wyngaard, J. C., and R. A. Brost, Top-down and bottom-up diffusion in the convective boundary layer, *J. Atmos. Sci.*, *41*, 102–112, 1984.

Zeman, O., and J. L. Lumley, Modeling buoyancy driven mixed layers, *J. Atmos. Sci.*, *33*, 1974–1988, 1976.

S. C. Doney, W. G. Large, and J. C. McWilliams, National Center for Atmospheric Research, P.O. Box 3000, Boulder, CO 80307.